Strong correlations in ultracold atomic gases

Andreas Nunnenkamp

A thesis submitted in partial fulfillment
of the requirements for the degree of
Doctor of Philosophy at the University of Oxford

St. John's College
University of Oxford
Trinity Term, 2008

Strong correlations in ultracold atomic gases

Andreas Nunnenkamp, St. John's College, Oxford

Thesis submitted in partial fulfillment of the requirements for the degree of Doctor of Philosophy at the University of Oxford. Trinity Term, 2008

Abstract

In this thesis we investigate strongly-correlated states of ultracold bosonic atoms in rotating ring lattices and arrays of double-well potentials.

In the first part of the thesis, we study the tunneling dynamics of ultracold bosons in double-well potentials. In the non-interacting limit single-particle transitions dominate, while in the interaction-dominated regime correlated tunneling of all particles prevails. At intermediate times of the many-particle flopping process correlated states occur, but the timescales of these processes increase dramatically with the number of particles. Using an array of double-well potentials, a large number of such few-particle superposition states can be produced in parallel.

In the second part of the thesis, we study the effects of rotation on ultracold bosons confined to one-dimensional ring lattices. We find that at commensurate filling there exists a critical rotation frequency, at which the ground state of the weakly-interacting gas is fragmented into a macroscopic superposition of different quasi-momentum states. We demonstrate that the generation of such superposition states using slightly non-uniform ring lattices has several practical advantages. Moreover, we show that different quasi-momentum states can be distinguished in time-of-flight absorption imaging and propose to probe correlations via the many-body oscillations induced by a sudden change in the rotation frequency. Finally, we compare these macroscopic superposition states to those occurring in superconducting quantum interference devices.

In the third part of the thesis, we demonstrate the creation of entangled states with ultracold bosonic atoms by dynamical manipulation of the shape of the lattice potential. To this end, we consider an optical superlattice that allows both the splitting of each site into a double-well potential and the variation of the height of the potential barrier between the sites. We show how to use this array of double-well potentials to perform entangling operations between neighboring qubits encoded on the Zeeman levels of the atoms. As one possible application, we present a method of realizing a resource state for measurement-based quantum computation via Bell-pair measurements.

In the final part of the thesis, we study ultracold bosons on a two-dimensional square lattice in the presence of an effective magnetic field and point out a couple of features this system has in common with ultracold bosons in one-dimensional rotating ring lattices.

Contents

Chapter 1

From weakly-interacting superfluids to strongly-correlated systems

Advances in cooling techniques for magnetically or optically trapped atoms over the last few decades have paved the way for the observation of Bose-Einstein condensation [1, 2, 3] and Fermi degeneracy [4, 5, 6] in ultracold dilute gases. These developments have opened up a new and exciting field of atomic, molecular and optical physics, where interacting many-particle systems can be probed and manipulated in space and time within an exceptionally clean environment.

The first generation of experiments with ultracold atomic gases focused on the coherence properties of these weakly-interacting superfluids. Some of the most important examples are the observation of interference between two overlapping condensates [7], of long-range phase coherence [8], and of quantized vortices and vortex lattices [9, 10]. All of these phenomena can be explained by introducing a so-called macroscopic wave function or order parameter, which reduces the full many-body problem to a non-linear single-particle problem governed by the Gross-Pitaevskii equation for bosons or the Ginzburg-Landau theory for fermions. Beyond these mean-field approaches weak interactions can be included in Bogoliubov theory describing the interacting many-body system in terms of weakly-interacting quasi-particles. This regime has been the topic of a number of review articles and textbooks such as [11, 12, 13, 14].

More recently, two developments have given the relatively young field of ultracold atomic gases a new direction and have attracted much attention also among physicists with a background in condensed matter physics, nuclear physics and quantum information science. These are the ability to tune the interaction strength between the particles by means of so-called *Feshbach resonances* [15, 16] and the possibility to load ultracold quantum gases into *optical lattices* [17].

These two techniques, together or by themselves, have made it possible to realize quantum liquids in the strongly-interacting regime, where the interaction energy of the particles dominates over their kinetic energies. The two most-popular phenomena in this context are the *superfluid to Mott insulator transition* of bosonic atoms in an optical lattice [18, 17] and the crossover between Bardeen-Cooper-Schrieffer superfluidity of atom pairs and Bose-Einstein condensation of diatomic molecules (*BEC-BCS crossover*), studied in fermionic atoms close to a Feshbach resonance [19, 20, 21, 22]. A review [23] of these experiments and the relevant theory has just appeared in the literature.

These experiments have successfully demonstrated long coherence times as well as a high degree of control over the experimental parameters, showing that the engineering of model Hamiltonians for various purposes should be possible. There are at least three different goals for the research on strong correlations in ultracold atomic gases:

- *Generation of macroscopic superposition states*: Macroscopic superposition states or Schrödinger cat states are one class of strongly-correlated states crucial in examining the foundations of quantum mechanics. The overriding issue is, of course, whether there is a mesoscopic scale at which the laws of quantum mechanics break down, in other words the nature of the quantum-to-classical transition [24].

- *Quantum simulation of many-body systems*: The experiments on the Mott transition and the BEC-BCS crossover have established ultracold quantum gases as model systems for condensed matter problems. It is believed that some open questions about the properties of the phase diagram or the non-equilibrium dynamics of quantum many-body systems can be addressed using ultracold gases as “quantum simulators”, programmable quantum systems which simulate other less accessible or less controllable quantum systems [25].

- *Quantum information processing*: Ultracold atoms seem to be ideal candidates for future quantum technologies which directly exploit the laws of quantum mechanics for applications such as quantum computation, quantum communication and Heisenberg-limited precision measurements. The strong correlations between the particles are in this case a useful resource which enables an exponential speed up of some computational problems [26] and allows for interferometry with phase estimation beyond the standard quantum limit [27].

In this thesis we study strongly-correlated states of ultracold bosonic atoms in optical lattices. We consider lattice geometries such as rotating ring lattices and arrays of double-well potentials which are within the reach of current experiments. The unifying notion is that strong correlations occur when the interaction energy of the particles dominates over their kinetic energies. The theoretical description of these systems is challenging, because, on the one hand, they cannot be reduced to systems of weakly-interacting quasi-particles, and, on the other hand, the Hilbert space of the full many-body problem increases exponentially with increasing number of particles. For this reason we will make frequent use of exact diagonalization for small system sizes and derive effective Hamiltonians in order to gain more insight into the occurring quantum correlations.

In Chapter 2 we show that ultracold bosonic atoms in deep optical lattices can be described using the Bose-Hubbard model and discuss some of the most important properties of the superfluid and Mott insulating phases. In a typical experiment the latter regime is reached by increasing the lattice depth at commensurate filling, so that the kinetic energy becomes comparable to the on-site interaction energy. The nearly degenerate many-body configurations are then strongly mixed by the on-site interaction matrix elements and result in the strongly-correlated Mott insulating ground state.

In Chapter 3 we study the tunneling dynamics of ultracold bosons in double-well potentials. The strong correlations in the Mott insulating regime dramatically affect the non-equilibrium dynamics of the particles. In the non-interacting limit single-particle transitions dominate, while in the interaction-dominated regime correlated tunneling prevails. At intermediate times of the many-particle flopping process correlated states are formed. This is related to the occurrence of macroscopic superposition states in rotating ring lattices and of superexchange interactions in optical superlattices to be discussed in Chapter 4 and Chapter 6, respectively.

In Chapter 4 we study the effect of rotation on ultracold bosons in one-dimensional ring lattices. We show that there exists a critical rotation frequency, at which the single-particle spectrum is degenerate and the weakly-interacting ground state becomes a macroscopic superposition of different quasi-momentum states. We extend our discussion to the case of a ring superlattice which has several practical advantages. Finally, we show that different quasi-momentum states can be distinguished in time-of-flight absorption imaging and propose to probe correlations via the many-body oscillations induced by a sudden change in the rotation frequency.

In Chapter 5 we study macroscopic superposition states produced in flux qubit devices. We start by deriving the effective action of these “artificial” quantum devices in the limit of low temperatures and small frequencies. We find that the magnetic flux threading the superconducting ring is the only essential variable, since fluctuations in all other macroscopic variables are strongly suppressed due to the energy gap in the charged superconductor. We show that macroscopic superposition states can be achieved in the macroscopic quantum coherence regime, where the tunneling barrier of the adiabatic potential is small even for a large number of Cooper pairs. Finally, we compare the two different mechanisms leading to macroscopic superposition states: correlated tunneling and tunneling in adiabatic potentials.

In Chapter 6 we consider ultracold bosons with two hyperfine states loaded into an array of double-well potentials. Their tunneling dynamics in the interaction-dominated regime is governed by so-called superexchange processes. We present how to use them in order to perform entangling operations between neighboring qubits encoded on the Zeeman levels of the atoms and prepare robust entangled states which remain unaffected by collective decoherence. As one possible application, we present a method of realizing a resource state for measurement-based quantum computing via Bell-pair measurements.

In Chapter 7 we study ultracold bosons on a two-dimensional square lattice in the presence of an effective magnetic field and point out a couple of features this system has in common with ultracold bosons in rotating ring lattices we discussed in Chapter 4. Starting from the degenerate single-particle spectrum known as the Hofstadter butterfly, we find that interactions lift the huge degeneracy of the non-interacting system apart from topological degeneracies. Parallel to our previous work, we derive an effective many-body Hamiltonian and show that a weak random potential can lead to ground-state splittings which decrease exponentially with increasing number of particles.

In Chapter 8 we conclude the thesis with a brief summary of the research it contains and give a view of possible directions for future work.

Publications. Parts of this thesis have been published in peer-reviewed journals. Chapter 4 is based on Refs. [28, 29] and Chapter 6 is published as Ref. [30]. During my time at Oxford, I also worked on Ref. [31] which is not included in this thesis.

Chapter 2

Ultracold bosons in optical lattices

In this chapter, we show when ultracold bosonic atoms in optical lattices can be described using the Bose-Hubbard model [32]. We first discuss the basic physics of optical potentials and of a single particle in a periodic potential. We then derive the Bose-Hubbard model as the microscopic description of ultracold bosons in optical lattices [18] and discuss some of the most important properties of the superfluid and Mott insulating phases. Finally, we describe how they can be probed in experiments with ultracold atomic gases.

2.1 Optical potentials

To understand the physical origin of the confinement of cold atoms with laser light, we consider a two-level atom interacting with an off-resonant light field. The Hamiltonian for a *two-level atom* in the absence of radiation may be written in the form $\hat{H}_0 = \hbar\omega_0 |e\rangle\langle e|$, where we have set the energy of the ground state $|g\rangle$ to zero and ω_0 denotes the transition frequency between the ground state $|g\rangle$ to the excited state $|e\rangle$.

In the *dipole approximation*, the effect of a classical light field $\mathbf{E}(\mathbf{x}, t) = \mathbf{E}_0(\mathbf{x}) \cos\omega_L t$ with frequency ω_L and field amplitude $\mathbf{E}_0(\mathbf{x})$ on a two-level atom is described by the Hamiltonian $\hat{H}_I = -\mathbf{d}\cdot\mathbf{E} = \hbar\Omega_R(\mathbf{x})\,(|e\rangle\langle g|\cos\omega_L t + h.c.)$ where $\Omega_R(\mathbf{x}) = \langle e|\mathbf{d}\cdot\mathbf{E}_0(\mathbf{x})|g\rangle/\hbar$ is the Rabi frequency and $\mathbf{d} = e\mathbf{x}$ the atomic dipole moment. This approximation is valid as long as the wavelength of the light is large compared to the size of the atom.

Going into a frame rotating at the laser frequency ω_L and neglecting rapidly oscillating terms at frequency $\omega_L + \omega_0$ (*rotating wave approximation*), we obtain the Hamiltonian

$$\hat{H} = \hat{H}_0 + \hat{H}_I = \hbar(\omega_0 - \omega_L)\,|e\rangle\langle e| + \hbar\Omega_R/2\,(|e\rangle\langle g| + h.c.) = \hbar\begin{pmatrix} \Delta & \Omega_R/2 \\ \Omega_R/2 & 0 \end{pmatrix}, \quad (2.1)$$

where we introduced the detuning parameter $\Delta = \omega_0 - \omega_L$.

In the limit of large detuning $\Delta \gg \Omega_R$, we can eliminate the excited state $|e\rangle$ using second-order perturbation theory. It predicts that the energy of the ground state $|g\rangle$ is simply shifted by $E_g(\mathbf{x}) = \frac{|\Omega_R(\mathbf{x})|^2}{4\Delta}$. This is the so-called *ac-Stark shift* which is proportional to the intensity of the laser light $I(\mathbf{x}) = |\mathbf{E}_0(\mathbf{x})|^2$ and the polarizability of the atom $\alpha(\omega) = \frac{|\langle e|d|g\rangle|^2}{\omega_0-\omega}$, taken at the laser frequency $\omega = \omega_L$. For red-detuned light, i.e. $\Delta < 0$ or $\omega_L < \omega_0$, the atoms are attracted to the anti-nodes of the light field where the electric field intensity $I(\mathbf{x})$ is maximal. For blue-detuned light, i.e. $\Delta > 0$ or $\omega_L > \omega_0$, the atoms are attracted to the nodes of the light field where the electric field intensity $I(\mathbf{x})$ is minimal.

To generate a one-dimensional optical lattice one interferes two counter-propagating laser beams of equal beam parameters and polarization, e.g. by reflecting one beam back into itself. They will form a *standing wave pattern* $V(x) = V_0 \sin^2 k_L x$ with lattice depth $V_0 = 4E_0$, wave vector $k_L = 2\pi/\lambda_L = \omega_L/c$, and lattice constant $a = \lambda_L/2$. One way to construct optical lattices in higher dimensions is by combining one-dimensional lattices. With different polarizations or slightly detuned frequencies along the different axis, interference terms average out and a three-dimensional square lattice is obtained

$$V(x,y,z) = V_0 \left(\sin^2 k_L x + \sin^2 k_L y + \sin^2 k_L z\right). \tag{2.2}$$

So far, we have neglected the possibility of spontaneous emission from the excited state $|e\rangle$ which introduces dissipative scattering processes, e.g. the absorption of an off-resonant photon followed by spontaneous emission into the vacuum. The effective decay rate Γ_{eff} can be estimated by the product of the decay rate Γ for the excited state $|e\rangle$ and the probability of an atom occupying the excited state $|e\rangle$. Assuming that the atom is in the motional ground state of a single potential well (see harmonic approximation below), one obtains for red-detuned lattices $\Gamma_{\text{eff}} = V_0\Gamma/\hbar|\Delta|$ [33]. Let us take the example of an optical lattice produced by a red-detuned laser with $\lambda_L = 852$nm driving the $\mathrm{S}_{1/2} \rightarrow$

$P_{3/2}$ transition in ^{87}Rb at $\lambda_0 = 795$nm with the linewidth $\Gamma = 2\pi \times 6$MHz. The recoil energy is in this case $E_R = 2\pi \times 3.1$kHz which gives a detuning of $\hbar\Delta = -8.0 \times 10^9 E_R$. For a lattice depth $V_0 = 25E_R$ the effective spontaneous emission rate is $\Gamma_{\text{eff}} = 0.2 \times 10^{-2} s^{-1}$ which corresponds to a timescale on the order of minutes [33]. As the experiments with ultracold atoms in optical lattices usually take place on timescales of up to a few seconds, spontaneous emission can be neglected for an appropriate choice for the detuning parameter Δ. In the following, we will assume that all optical potentials are conservative.

2.2 Band structure

Let us now consider the states of atoms in an optical lattice potential. Neglecting at first the interaction between the particles we have to solve the textbook problem of a single particle subject to a periodic potential $V(x)$. The single-particle Hamiltonian has the form $\hat{H} = \hat{p}^2 + V(x)$, with $V(x) = V(x + a)$, and a is the lattice constant.

Bloch's theorem tells us we can write the wave function in the form $\psi(x) = e^{iqx} u_q(x)$, with $u_q(x) = u_q(x + a)$, and where q is the so-called quasi-momentum. Using the Fourier decomposition of $u_q(x)$, i.e. $u_q(x) = \frac{1}{\sqrt{2\pi}} \sum_l u_q^l e^{iG_l x}$ of the periodic function $u_q(x)$ with $G_l = 2\pi l/a$ and l integer, we obtain the so-called central equation

$$\frac{\hbar^2}{2M}(q + G_l)^2 u_q^l + \sum_m V_{l-m} u_q^m = E u_q^l, \tag{2.3}$$

where $V_l = \frac{1}{\sqrt{2\pi}} \int dx\, V(x)\, e^{-iG_l x}$ are the Fourier components of the potential $V(x)$ and M is the mass of the atoms.

Using the identity $\sin^2 kx = \frac{1}{2} + \frac{\mathrm{e}^{\mathrm{i}2kx}}{4} + \frac{\mathrm{e}^{-\mathrm{i}2kx}}{4}$, we obtain the band structure from the following tridiagonal matrices: $\left(H_q\right)_{ll} = E_R \left(\frac{qa}{\pi} + 2l\right)^2 + \frac{V_0}{2}$ and $\left(H_q\right)_{lm} = \frac{V_0}{4}$ for $|l - m| = 1$, with the recoil energy $E_R = \hbar^2 k_L^2/2M = \hbar^2\pi^2/2Ma^2$. For a lattice with L sites, we solve Eq. (2.3) for each of the quasi-momenta $qa/\pi \in \{-1 + 2/L, -1 + 2(2/L), \ldots, 1\}$ separately.

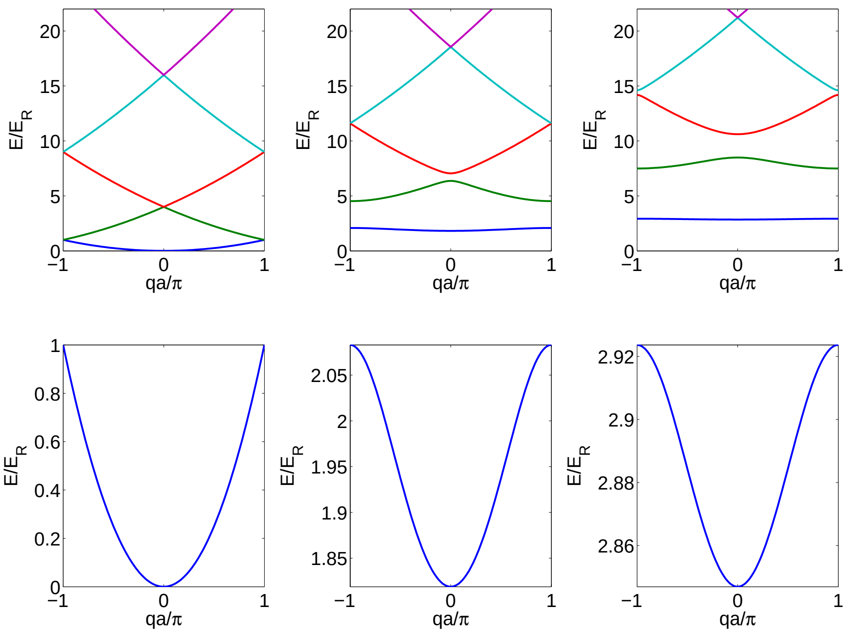

Fig. 2.1: Band structure for $V_0/E_R = \{0, 5, 10\}$ (from left to right). The top row shows the five lowest bands, the lower one a zoomed in plot of the lowest band.

In Fig. 2.1 we plot the five lowest energy bands for lattice depths $V_0/E_R = \{0, 5, 10\}$. For $V_0 = 0$ we recover the dispersion of a free particle $E_q/E_R = (qa/\pi)^2$, while for a finite lattice depth V_0 a band gap opens at the zone boundary $qa = \pm\pi$. With increasing lattice depth V_0 the band width decreases. In Fig. 2.1 we also show a zoomed in plot for the lowest energy band which evolves from a parabolic form in the absence of a lattice to a cosine form in the deep lattice limit.

In treating the effects of local interactions it will be convenient to choose single-particle wave functions which are localized in position space. For each Bloch band with band index n we, therefore, construct the set of Wannier functions $w_n(x - x_j)$ which are centered at the positions of the lattice sites x_j

$$w_n(x - x_j) = \frac{a}{2\pi} \int_{\mathrm{BZ}} dq\, e^{-iqx_j} \psi_q^{(n)}(x). \tag{2.4}$$

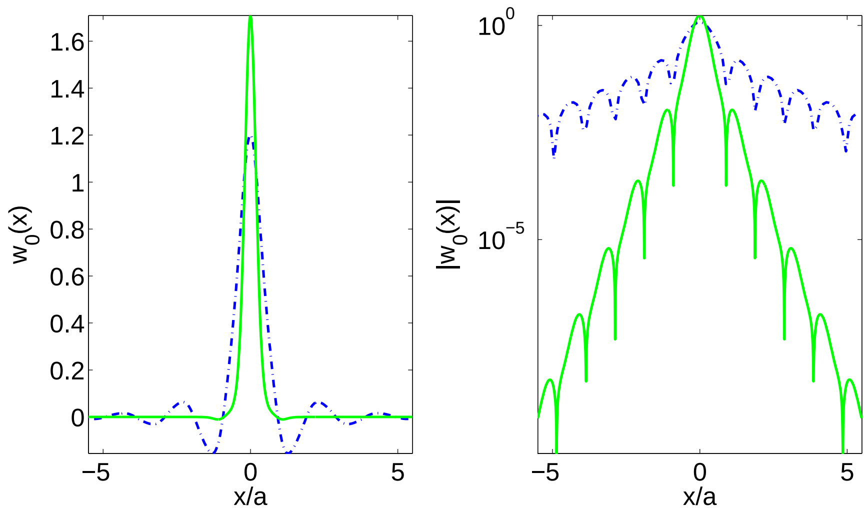

Fig. 2.2: Maximally-localized Wannier functions [34, 35] of the lowest band $w_0(x)$ for $V_0/E_R = 1$ (dash-dotted) and $V_0/E_R = 10$ (solid), both on a linear (left) and a logarithmic (right) scale. [Help by Dr Stephen R. Clark is acknowledged.]

In this expression, the integral is taken over the first Brillouin zone $-1 < qa/\pi < 1$ and $\psi_q^{(n)}(x) = e^{iqx}u_q^{(n)}(x) = e^{iqx}\frac{1}{\sqrt{2\pi}}\sum_l u_{qn}^l e^{iG_l x}$ is the Bloch wave function. In Fig. 2.2 we show the maximally-localized Wannier functions [34, 35] of the lowest band $w_0(x)$ for $V_0/E_R = 1$ and $V_0/E_R = 10$, both on a linear and a logarithmic scale.

2.3 The Bose-Hubbard model

At ultracold temperatures the two-body interaction between the particles can be approximated by the pseudopotential $V_{\text{2body}}(\mathbf{x},\mathbf{x}') \propto a_s\delta(\mathbf{x}-\mathbf{x}')$ where a_s is the s-wave scattering length. The many-body Hamiltonian for bosonic atoms with the optical potential $V(\mathbf{x})$ and the two-body interaction potential $V_{\text{2body}}(\mathbf{x},\mathbf{x}')$ can be written in the form

$$\hat{H} = \int d\mathbf{x}\hat{\Phi}^\dagger(\mathbf{x})\left[-\frac{\hbar^2}{2M}\nabla^2 + V(\mathbf{x})\right]\hat{\Phi}(\mathbf{x}) + \frac{1}{2}\cdot\frac{4\pi a_s\hbar^2}{M}\int d\mathbf{x}\hat{\Phi}^\dagger(\mathbf{x})\hat{\Phi}^\dagger(\mathbf{x})\hat{\Phi}(\mathbf{x})\hat{\Phi}(\mathbf{x}), \quad (2.5)$$

where $\hat{\Phi}(\mathbf{x})^\dagger$ and $\hat{\Phi}(\mathbf{x})$ are bosonic creation and annihilation field operators satisfying the canonical commutation relations: $\left[\hat{\Phi}(\mathbf{x}),\hat{\Phi}^\dagger(\mathbf{x}')\right] = \delta(\mathbf{x}-\mathbf{x}')$ and $\left[\hat{\Phi}(\mathbf{x}),\hat{\Phi}(\mathbf{x}')\right] = \left[\hat{\Phi}^\dagger(\mathbf{x}),\hat{\Phi}^\dagger(\mathbf{x}')\right] = 0$.

If the optical lattice is sufficiently deep, i.e. the band gap between the different Bloch bands is large compared to the interaction energy, we can make the *single-band approximation* and neglect the coupling between different bands. Expanding the field operators in the set of Wannier functions of the first band $\hat{\Phi}(\mathbf{x}) = \sum_j w_0(\mathbf{x} - \mathbf{x}_j)\,\hat{a}_j$ and substituting this expression into the many-body Hamiltonian we obtain

$$\hat{H} = \sum_{i,j} J_{ij}\hat{a}_i^\dagger \hat{a}_j + \frac{U}{2}\sum_{ijkl} \hat{a}_i^\dagger \hat{a}_j^\dagger \hat{a}_k \hat{a}_l. \tag{2.6}$$

In this expression, we defined the tunneling matrix elements

$$J_{ij} = \int d\mathbf{x}\, w_0^*(\mathbf{x} - \mathbf{x}_i)\left[-\frac{\hbar^2}{2M}\nabla^2 + V(\mathbf{x})\right] w_0(\mathbf{x} - \mathbf{x}_j) = \frac{a}{2\pi}\int_{\mathrm{BZ}} d\mathbf{q}\, e^{i\mathbf{q}\cdot(\mathbf{x}_i - \mathbf{x}_j)} E_{\mathbf{q}} \tag{2.7}$$

and the interaction matrix elements

$$U_{ijkl} = \frac{4\pi a_s \hbar^2}{M}\int d\mathbf{x}\, w_0(\mathbf{x} - \mathbf{x}_i)^* w_0(\mathbf{x} - \mathbf{x}_j)^* w_0(\mathbf{x} - \mathbf{x}_k) w_0(\mathbf{x} - \mathbf{x}_l). \tag{2.8}$$

In Fig. 2.3 we plot the tunneling matrix elements J_{01}, J_{02} and J_{03}, as well as the interaction matrix elements U_{0000}, U_{0001} and U_{0101}, as a function of the lattice depth V_0. For deep lattices $V_0 \geq 5E_R$ the tunneling matrix elements between nearest neighbors J_{01} and the on-site interaction energy U_{0000} are the dominant terms.

In the *tight-binding approximation*, we keep only these terms, i.e. the nearest-neighbor tunneling $J \equiv -J_{01} > 0$ and the on-site interaction $U \equiv U_{0000}$, and hence obtain the Hamiltonian of the Bose-Hubbard model

$$\hat{H} = -J\sum_{\langle i,j\rangle}\left(\hat{a}_i^\dagger \hat{a}_j + H.c.\right) + \frac{U}{2}\sum_j \hat{n}_j(\hat{n}_j - 1). \tag{2.9}$$

For sufficiently deep lattices the Wannier function $w_0(x)$ has a spatial extent smaller than the lattice constant a and can be approximated by the ground-state wavefunction of a single potential well. Expanding the lattice potential $V(x)$ around this minimum to second order, we obtain the so-called harmonic approximation, $V_{\mathrm{ho}}(x) = M\omega_{\mathrm{ho}}^2 x^2/2$ with

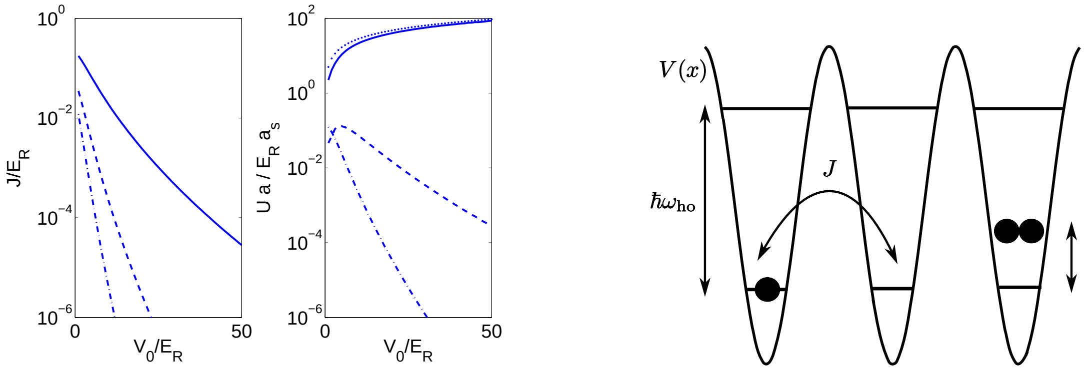

Fig. 2.3: (Left) Tunneling matrix elements $|J_{01}|$ (solid), $|J_{02}|$ (dashed) and $|J_{03}|$ (dash-dotted) as well as interaction matrix elements U_{0000} (solid) with its harmonic approximation $U_{0000}^{(ho)}$(dotted), U_{0001} (dashed) and U_{0101} (dashed-dotted) as a function of the lattice depth V_0. (Right) Parameters of Bose-Hubbard model. [Help by Dr Stephen R. Clark is acknowledged.]

$\hbar\omega_{ho} = 2\sqrt{V_0 E_R}$. The ground-state wave function is thus $\psi_{ho}(x) = \left(\sqrt{\pi}a_{ho}\right)^{-1/2} e^{-x^2/2a_{ho}^2}$ with the harmonic oscillator length $a_{ho} = \sqrt{\hbar/m\omega_{ho}}$. In this approximation we obtain

$$U_{0000}^{(ho)} = \sqrt{8\pi}\frac{a_s}{a}\left(\frac{V_0}{E_R}\right)^{3/4} E_R \tag{2.10}$$

for the on-site interaction energy U.

From the exact width of the lowest band (via the 1D Mathieu equation) we obtain

$$J = \frac{4}{\sqrt{\pi}}\left(\frac{V_0}{E_R}\right)^{3/4} \exp\left[-2\sqrt{\frac{V_0}{E_R}}\right] E_R \tag{2.11}$$

for the nearest-neighbor tunneling matrix element J (see e.g. [36]).

One of the most important features of the realization of the Bose-Hubbard model in a ultracold atomic system is that the ratio between the tunneling matrix element J and the on-site interaction energy U can be tuned over a wide range by varying the lattice depth

$$\frac{U}{J} \approx \frac{a_s}{a}\exp\left[2\sqrt{\frac{V_0}{E_R}}\right]. \tag{2.12}$$

From this expression, we see that the optical lattice effectively enhances the effects of the interactions between the particles and thus opens the possibility to study the physics of strongly-correlated systems with weakly-interacting dilute gases.

2.4 Quantum phase transition from a superfluid to a Mott insulator

At integer filling, i.e. if the number of atoms N is commensurate with the number of lattice sites L, the Bose-Hubbard model predicts a quantum phase transition [37]. When the ratio between the on-site interaction energy U to the tunneling matrix element J is increased beyond a certain critical value $(U/J)_c$, the ground-state wave function changes from a superfluid to a Mott insulating phase [32].

In the limit of small on-site interactions $J \gg U$, the system is in the *superfluid phase*. The superfluid wave function, for which the kinetic energy is minimized by delocalizing the atoms over the entire lattice, has the form

$$|\Psi_{\mathrm{SF}}\rangle \propto \left(\sum_{j=1}^{L} \hat{a}_j^\dagger\right)^N |\mathrm{vac}\rangle. \tag{2.13}$$

In the thermodynamic limit, where $N, L \to \infty$ with N/L fixed, the atoms on each site are in a coherent state $|\Psi\rangle_j = e^{-|\varphi_j|^2/2} \sum_{n=0}^{\infty} \frac{\varphi_j^n}{\sqrt{n!}} |n\rangle_j$ where $|n\rangle_j$ is the Fock state with n atoms on site j and $\varphi_j = \langle \hat{a}_j \rangle$ is the superfluid order parameter. It has a poissonian atom number distribution $P(n) = \bar{n}^n e^{-\bar{n}}/n!$ with the mean particle number $\bar{n} = N/L$. The superfluid momentum distribution can be detected using the peaks in the diffraction pattern after time-of-flight expansion [17, 38], whereas the atom number distribution can be probed via spin changing collisions [39].

Weak interactions between the atoms lead to quantum depletion of the condensate, i.e. a finite fraction of the particles are pushed into $p \neq 0$ momentum modes even at zero temperature. This effect can easily be included in *Bogoliubov theory* [40, 41, 42]. First, one has to solve the set of coupled non-linear Schrödinger (i.e. Gross-Pitaevskii) equations

$$i\hbar\partial_t z_j = -J(z_{j-1} + z_{j+1}) + U|z_j|^2 z_j.$$

In the case of a homogeneous lattice the uniform ansatz $z_j = \sqrt{\bar{n}}e^{-i\mu t/\hbar}$ with the number density $\bar{n} = N/L$ leads to a chemical potential $\mu = \bar{n}U - 2J$. Next, one linearizes the equation of motion

$$i\hbar\partial_t\hat{a}_j = -J(\hat{a}_{j-1} + \hat{a}_{j+1}) + U\hat{n}_j\hat{a}_j$$

by substituting $\hat{a}_j \to (z_j + \hat{\delta}_j)e^{-i\mu t/\hbar}$ and keeping operators up to second order. We obtain

$$i\hbar\partial_t\hat{\delta}_j = (2nU - \mu)\hat{\delta}_j - J(\hat{\delta}_{j-1} + \hat{\delta}_{j+1}) + nU\hat{\delta}_j^\dagger.$$

Decomposing the quasi-particle operators into Fourier modes

$$\hat{\delta}_j = \frac{1}{\sqrt{L}}\sum_q \left(u_q e^{i(qaj-\omega_q t)}\hat{\alpha}_q - v_q^* e^{-i(qaj-\omega_q t)}\hat{\alpha}_q^\dagger\right),$$

the equations for the quasi-particle amplitudes and frequencies are

$$\begin{aligned}\left[nU + 4J\sin^2\left(\frac{qa}{2}\right) - \hbar\omega_q\right]u_q + nUv_{-q} &= 0\\ nUu_q + \left[nU + 4J\sin^2\left(\frac{qa}{2}\right) + \hbar\omega_q\right]v_{-q} &= 0.\end{aligned} \tag{2.14}$$

Their solution is given by

$$\begin{aligned}|u_q|^2 &= |v_q|^2 + 1 = \frac{\epsilon_q + nU + \hbar\omega_q}{2\hbar\omega_q}\\ \hbar\omega_q &= \sqrt{\epsilon_q(\epsilon_q + 2nU)}\end{aligned} \tag{2.15}$$

where $\epsilon_q = 4J\sin^2(qa/2)$ is the single-particle energy spectrum. We recognize the well-known linear phonon-like dispersion $\omega_q \propto q$ at small wave vectors $\epsilon_q \ll 2nU$ and the free-particle-like dispersion $\omega_q \approx \epsilon_q$ at large wave vectors $\epsilon_q \gg 2nU$. Using the decomposition $\hat{b}_k^\dagger = \frac{1}{\sqrt{L}}\sum_j e^{2\pi ikj/L}\hat{a}_j^\dagger$, the many-body wave function reads

$$|\Psi_{\mathrm{Bogo}}\rangle = \prod_{k\neq 0}\left(u_k + v_k\hat{b}_k^\dagger\hat{b}_{-k}^\dagger\hat{b}_0\hat{b}_0\right)|\Psi_{\mathrm{SF}}\rangle. \tag{2.16}$$

We see that pairs of particles with opposite momentum are excited out of the condensate, so that the number of particles in the condensate is reduced to $n - \sum_{q\neq 0} n_q = n - \sum_{q\neq 0}|v_q|^2$.

As the ratio U/J is increased, the quantum depletion increases. The Bogoliubov approximation eventually breaks down when the fluctuations in the number of particles in the condensate cannot be neglected.

In the limit of strong on-site interactions $J \ll U$, the system is in the *Mott insulating phase*. In this regime the atoms minimize the on-site interaction by localizing in lattice sites. It produces Fock states with zero number fluctuations

$$|\Psi_{\mathrm{MI}}\rangle \propto \prod_{j=1}^{L} \left(\hat{a}_j^\dagger\right)^{N/L} |\mathrm{vac}\rangle. \tag{2.17}$$

In contrast to the gapless superfluid state, the Mott insulator has an excitation gap U which can be probed by Bragg spectroscopy [43]. This also leads to the "wedding cake" density profile in the presence of the harmonic trapping potential [44, 45].

Weak tunneling can be included by perturbation theory, i.e. the so-called *strong coupling expansion* [46, 47, 48]. In first order the ground-state wave function is given by

$$|\Psi^{(1)}\rangle = |\Psi_{\mathrm{MI}}\rangle + \frac{J}{U} \sum_{\langle i,j\rangle} \hat{a}_i^\dagger \hat{a}_j |\Psi_{\mathrm{MI}}\rangle. \tag{2.18}$$

It has an admixture of adjacent particle-hole excitations. As the ratio J/U is increased, higher orders of the tunneling term become important, so that the particle-hole pairs can separate further across the lattice.

The ground-state phase diagram can be obtained most easily using the *Gutzwiller or mean-field decoupling ansatz* [40]. By substituting $\hat{a}_i^\dagger \hat{a}_j \rightarrow \langle \hat{a}_i^\dagger \rangle \hat{a}_j + \hat{a}_i^\dagger \langle \hat{a}_j \rangle - \langle \hat{a}_i^\dagger \rangle \langle \hat{a}_j \rangle$ or equivalently using the following mean-field ansatz

$$|\Psi_{\mathrm{GW}}\rangle = \prod_j |\Phi\rangle_j \;\text{ with }\; |\Phi\rangle_j = \sum_{n=0}^{\infty} f_n |n\rangle_j, \tag{2.19}$$

the Bose-Hubbard Hamiltonian factorizes into a sum of single-site Hamiltonians

$$\hat{H}^{\mathrm{GW}} = \sum_j \hat{H}_j^{\mathrm{GW}} \;\text{ with }\; \hat{H}_j^{\mathrm{GW}} = \frac{U}{2} \hat{n}_j (\hat{n}_j - 1) - \mu \hat{n}_j - zJ(\hat{a}_i^\dagger + \hat{a}_j)\phi + J\phi^2, \tag{2.20}$$

where $\phi = \langle \hat{a}_j \rangle$ is the superfluid order parameter, $z = 2d$ the number of nearest neighbors in a d-dimensional square lattice, and μ the chemical potential of the system in the grand-canonical ensemble. The single-site problem is easily solved numerically or approximately by second-order perturbation theory in the off-diagonal tunneling term $-zJ(\hat{a}_i^\dagger + \hat{a}_j)$. The unperturbed problem has the ground-state energy $E_n^{(0)} = 0$ for $\bar{\mu} < 0$ and $\bar{U}n(n-1) - \bar{\mu}n$ if $\bar{U}(n-1) < \bar{\mu} < \bar{U}n$, where $n = N/L$ is the number of atoms per site, $\bar{\mu} = \mu/J$ and $\bar{U} = U/J$ the normalized chemical potential and interaction energy. The tunneling term only couples the unperturbed state with n particles per site to states with $n-1$ and $n+1$ atoms, so we find the energy shift in second-order perturbation theory

$$E_n^{(2)} = \frac{|\langle n+1|\hat{a}^\dagger|n\rangle|^2}{E_n - E_{n+1}} + \frac{|\langle n-1|\hat{a}|n\rangle|^2}{E_n - E_{n-1}} = \frac{n+1}{\bar{\mu} - \bar{U}n} + \frac{n}{\bar{U}(n-1) - \bar{\mu}}. \tag{2.21}$$

Following Landau's theory for second-order phase transitions, we write the ground-state energy as an expansion in the order parameter ϕ, i.e. $E_n(\phi) = a_0(n, \bar{U}, \bar{\mu}) + a_2(n, \bar{U}, \bar{\mu})\phi^2 + O(\phi^4)$ with $a_0(n, \bar{U}, \bar{\mu}) = E_n^{(0)}$ and $a_2(n, \bar{U}, \bar{\mu}) = E_n^{(2)} + 1$. We then determine the boundary between the superfluid and Mott insulating phase by requiring $a_2(n, \bar{U}, \bar{\mu}) = 0$, i.e.

$$(\mu/U)_\pm = \frac{1}{2}\left[2n - 1 - (zJ/U) \pm \sqrt{1 - 2(2n+1)(zJ/U) + (zJ/U)^2}\right]. \tag{2.22}$$

We have given a plot of the phase diagram in Fig. 2.4. The tip of the Mott lobes, where $(\mu/U)_+ = (\mu/U)_-$, is given by $(U/J)_c = z(2n + 1 + \sqrt{(2n+1)^2 - 1})$ which gives $(U/J)_c \approx z \times 5.83$ for the $n = 1$ insulator.

We note that the appearance of the strongly-correlated Mott insulating state fits well into the main theme of the thesis. By increasing the lattice depth, the band width is reduced, so that the kinetic energy in the lowest band becomes comparable to the interaction energy. That means, all single-particle states in the lowest energy band become almost degenerate and are therefore strongly mixed by the on-site interaction matrix elements. The Mott insulating state is then a superposition of the quasi-degenerate many-body states.

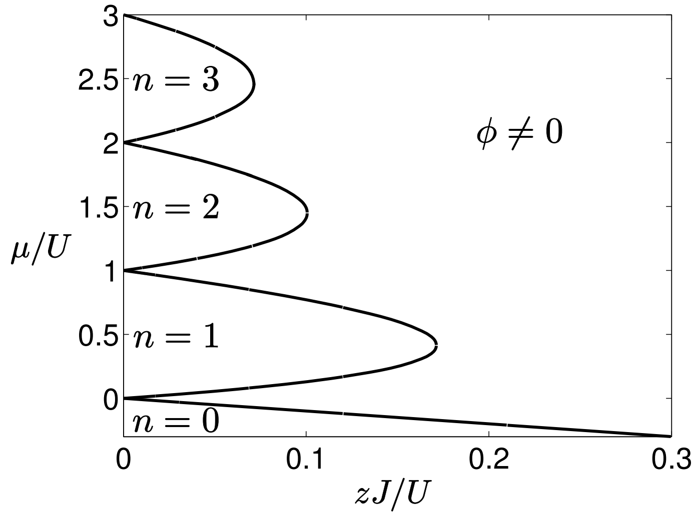

Fig. 2.4: Mean-field phase diagram of the Bose-Hubbard model (2.9) given by Eq. (2.22).

2.5 Probing the Bose-Hubbard model with ultracold atoms in optical lattices

Let us now turn to the question how the properties of the Bose-Hubbard model and its mean-field phases can be probed in experiments with ultracold atoms in optical lattices.

The most popular detection method in ultracold atom experiments is *absorption imaging after time-of-flight expansion* [49]. In this technique, all optical and magnetic potentials are suddenly switched off and the atom cloud is allowed to expand freely. After a certain time-of-flight t an ordinary absorption image of the enlarged cloud is taken. To calculate its density distribution we expand the amplitude operator $\hat{A}(x,t)$ in terms of the initial wavepackets as $\hat{A}(x,t) = \sum_j \hat{a}_j\, \varphi_j(x,t)$ where $\hat{a}_j$ are the destruction operators for a particle at lattice site j and $\varphi_j(x,t) = \hat{U}(t)\, \varphi_j(x, t=0) = \hat{U}(t)\, w_0(x - x_j)$ with the Wannier function $w_0(x - x_j)$ centered at lattice site j and the time evolution operator $\hat{U}(t)$. Neglecting the effects of interactions during the expansion, i.e. $\hat{U}(t) = \exp\left[-\frac{i}{\hbar}\frac{\hat{p}^2}{2m}t\right]$, we can calculate the wave function in the far-field and long-time limit within the stationary-phase approximation to be $\varphi_j(x,t) \approx \sqrt{\frac{m}{\hbar t}}\, \tilde{w}_0(\overline{k})\, e^{i\overline{k}(x-x_j)}$ with $\overline{k} = mx/\hbar t$ and $\tilde{w}_0(\mathbf{k})$ the Fourier transform of the Wannier function $w_0(\mathbf{r})$. The density distribution observed after some time-of-flight t is then given by [50, 51]

$$n(\mathbf{x}) = \langle \hat{A}^\dagger(\mathbf{x})\hat{A}(\mathbf{x})\rangle = \left(\frac{m}{\hbar t}\right)^3 \left|\tilde{w}\left(\mathbf{k} = \frac{m\mathbf{r}}{\hbar t}\right)\right|^2 S\left(\mathbf{k} = \frac{m\mathbf{r}}{\hbar t}\right) \tag{2.23}$$

where $S(\mathbf{k})$ is the static structure factor and identical to the quasi-momentum distribution

$$S(\mathbf{k}) = \sum_{i,j} e^{i\mathbf{k}\cdot(\mathbf{r}_i - \mathbf{r}_j)}\langle \hat{a}_i^\dagger \hat{a}_j\rangle = \langle \hat{b}_\mathbf{k}^\dagger \hat{b}_\mathbf{k}\rangle = \langle \hat{n}_\mathbf{k}\rangle. \tag{2.24}$$

In the non-interacting limit $U = 0$, where all particles have condensed into the $\mathbf{k} = 0$ quasi-momentum state, we have $\langle \hat{a}_i^\dagger \hat{a}_j\rangle = N_0$, so that the wave packets from the different lattice sites interfere coherently and lead to diffraction peaks in the time-of-flight diffraction pattern. In the Mott insulating $J = 0$ state, we have $\langle \hat{a}_i^\dagger \hat{a}_j\rangle = \delta_{ij}$, so that we expect to see only the Fourier transform of the single-site wave function $w_0(\mathbf{r})$. In Fig. 2.5 we show the interference pattern observed after time-of-flight expansion in the seminal experiment performed in Munich [17]. One clearly recognizes the transition from the superfluid regime with its interference peaks to the Mott insulating regime where the interference pattern is washed out.

One novel detection technique is the analysis of the *noise correlations* in the absorption images after time-of-flight expansion. Proposed in Ref. [52], it was used to detect the density-density correlations after molecule dissociation [53] and of a Mott insulating state of bosons [54] as well as the anti-bunching of free fermions in a lattice [55]. It has great promise in distinguishing many different phases of proposed phase diagrams.

Another new technique used to characterize the quantum state of ultracold atoms in optical lattices are spin-changing collisions [56]. With their help it has been possible to measure the squeezing in the *atom number distribution* [39] and then by additionally applying a spatially varying bias field the "wedding cake" *density profile* of a Mott insulator in a trapping potential [44].

Fig. 2.5: Absorption images of multiple matter-wave interference patterns. These were obtained after suddenly releasing the atoms from an optical lattice potential with different potential depths V_0 after a time-of-flight of 15 ms. Values of V_0 were: a) 0 E_R, b) 3 E_R, c) 7 E_R, d) 10 E_R, e) 13 E_R, f) 14 E_R, g) 16 E_R and h) 20 E_R. [Reprinted from Ref. [17].]

Apart from exploring the equilibrium ground-state phase diagram of the standard Bose-Hubbard model ultracold atomic gases in optical lattices offer the possibility to observe *non-equilibrium dynamics* due to their long coherence times. Quantum quenches, i.e. sudden changes of the parameter J/U, lead to collapse and revival of the coherent matter-wave field [57]. Following the proposal [58], state-dependent optical lattice potentials [59] have been used to observe entanglement oscillations of 1D spin chains [60]. This involved the preparation of 1D cluster states [61] whose two-dimensional relatives are a general resource state for quantum one-way computing [62].

Since single-site addressability is crucial to many of the promising applications such as quantum simulation and quantum computing proposals, there have recently been major efforts to extend the possibility to manipulate atoms in optical lattices more selectively via *optical superlattices* [63, 64]. In first experiments it has allowed the observation of two-atom correlated tunneling [65], the realization of so-called $\sqrt{\text{SWAP}}$-gates [66], and the control over spin-exchange interactions [67].

Chapter 3

Correlated tunneling of ultracold bosons in double-well potentials

In this chapter, we study the tunneling dynamics of ultracold bosons in double-well potentials. In the non-interacting limit single-particle transitions dominate, while in the interaction-dominated regime correlated tunneling prevails. At intermediate times of the many-particle flopping process correlated states are formed, but the tunneling times increase dramatically with the number of particles. Using an array of double-well potentials, a large number of few-particle superposition states can be produced in parallel.

3.1 Introduction

In the absence of interactions many-body systems reduce to a set of single-particle ones, where the atoms move independently of each other. The situation changes drastically once interactions become important: the particles affect each other and become correlated.

Double-well potentials are one of the simplest non-trivial "lattice" configurations. Recently, arrays of double-well potentials have been realized experimentally [63, 64]. This opens up novel possibilities for manipulating atoms in optical lattices. For instance, this setup allows to explore the physics of double-well potentials in the few-atom limit. Due to the large number of identical double-well potentials in the array, a good signal-to-noise ratio can be achieved despite the small number in each of them.

In this chapter, we study the tunneling dynamics of ultracold bosons loaded into an array of double-well potentials. Using the two-site Bose-Hubbard model, we find two qualitatively different dynamical regimes. In the non-interacting limit the particles tunnel independently and single-particle Rabi oscillations dominate the dynamics. In the opposite limit single-particle transitions are suppressed by the interaction energy and slow many-particle transitions occur. We obtain an analytic expression for the many-particle tunneling times using perturbation theory. The fact that the tunneling time increases dramatically with the number of particles puts severe limitations on the number of particles that can be involved in these many-particle transitions on experimentally accessible time scales. Using arrays of double-well potentials, it is possible to study these few-particle superposition states with good statistics.

After the completion of these notes, several theoretical papers have considered correlated tunneling in symmetric or tilted double-well potentials [68, 69, 70]. In the meantime, correlated tunneling has entered the stage of cold atom experiments in the form of repulsively bound pairs in an optical lattice [71]. More recently, second-order tunneling of atom pairs has been observed in an array of double-well potentials [65] and has now been used to measure the atom number distribution in the superfluid to Mott insulator transition [72].

3.2 Model

Assuming that tunneling between the double-well potentials in the array can be neglected, we concentrate on a single symmetric double-well potential filled with N bosons. This system can be described by the well-known two-mode Bose-Hubbard model

$$\hat{H} = -J\left(\hat{a}_L^\dagger \hat{a}_R + h.c.\right) + \frac{U}{2}\left(\hat{n}_L(\hat{n}_L - 1) + \hat{n}_R(\hat{n}_R - 1)\right), \tag{3.1}$$

where $\hat{a}_i$ is the annihilation and $\hat{n}_i = \hat{a}_i^\dagger \hat{a}_i$ the number operator for atoms on the left- ($i = L$) and right-hand ($i = R$) side of the double-well potential. The first term in Eq. (3.1) describes tunneling between the two wells with tunneling matrix element J and the second the on-site interaction energy U.

In the Fock state basis an arbitrary state can be described by $|\psi\rangle = \sum_n c_n|n, N-n\rangle$, where n is the number of particles in state $|L\rangle$ and $N-n$ in state $|R\rangle$. The Hamiltonian (3.1) reduces to an $(N+1)\times(N+1)$ tridiagonal matrix which is easily diagonalized numerically. The initial state is taken to be $|\psi(t=0)\rangle = |0, N\rangle$. Defining a dimensionless time $\tau = Jt/(2\pi\hbar)$, we obtain the quantum state at time t through $|\psi(t)\rangle = \exp(-i\hat{H}t/\hbar)\,|\psi(t=0)\rangle$. We compute the atom number distribution $P_n(\tau) = |\langle n, N-n|\psi(\tau)\rangle|^2 = |c_n(\tau)|^2$, the mean number difference $\Delta n(\tau) = \sum_n n|c_n(\tau)|^2 - N/2$ and its variance $\sigma^2 = \langle\Delta n^2\rangle - \langle\Delta n\rangle^2$.

3.3 Single-particle transitions

Let us first discuss the non-interacting case $U = 0$. In Fig. 3.1 we show the atom number distribution $P_n(\tau)$ as well as the expectation values of the mean number difference Δn and its variance σ^2 as a function of the dimensionless time τ for $N = 2$ particles. The dynamics are, of course, determined by single-particle transitions, i.e. the system evolves from the initial Fock state $|0, N\rangle = \frac{1}{\sqrt{N!}}\left(\hat{a}_R^\dagger\right)^N|\mathrm{vac}\rangle$ via the coherent state $\frac{1}{\sqrt{N!}}\left(\frac{\hat{a}_L^\dagger+\hat{a}_R^\dagger}{\sqrt{2}}\right)^N|\mathrm{vac}\rangle$ to the Fock state $|N, 0\rangle = \frac{1}{\sqrt{N!}}\left(\hat{a}_L^\dagger\right)^N|\mathrm{vac}\rangle$. The time scale for that process is the single-particle tunneling time $\tau = 1$.

We note that matrix elements of the Hamiltonian that determine that coupling, i.e.

$$\langle n_L+1, n_R-1|\hat{a}_L^\dagger\hat{a}_R|n_L, n_R\rangle = \sqrt{n_L+1}\,\sqrt{n_R} \tag{3.2}$$

represent a “Bose-enhanced” coupling. In the non-interacting limit the N single-particle processes happen completely independently, so that the tunneling time for N particles is equal to the tunneling time of a single one τ. In the second quantized formulation the transition matrix elements are multiplied by a factor of the order of the number of particles N, but at the same time N particles have to be transferred, so that the time for an N-particle Rabi oscillation is the same as for a single-particle oscillation.

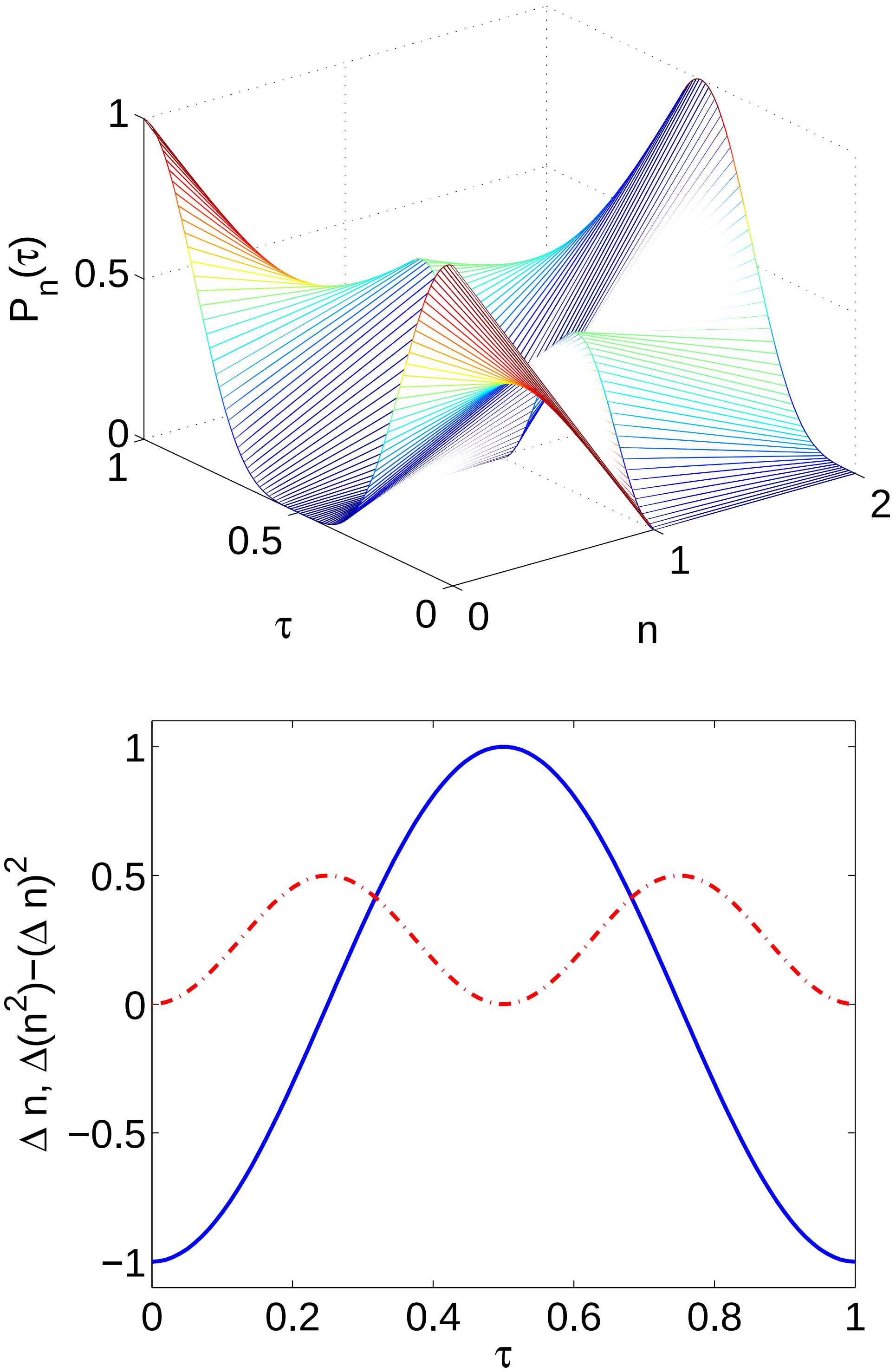

Fig. 3.1: *Single-particle transitions.* **(a)** Atom number distribution $P_n(\tau)$ and **(b)** mean number difference Δn (solid line) as well as its variance σ^2 (dashed-dotted line) in the non-interacting case ($U = 0$ and $N = 2$).

3.4 Many-particle transitions

In Fig. 3.2 we show the time dependence of the same observables as before, but now for $U/J = 10$ and $N = 2$ particles. Instead of single-particle Rabi flopping, we observe correlated tunneling of all N particles in the double-well potential. At intermediate times a cat-like state $\frac{|N,0\rangle+|0,N\rangle}{\sqrt{2}} = \frac{1}{\sqrt{2N!}}\left[\left(\hat{a}_L^\dagger\right)^N + \left(\hat{a}_R^\dagger\right)^N\right]|\mathrm{vac}\rangle$ is formed, and the tunneling times are much longer.

To explain these observations, we consider the zero-tunneling limit $J = 0$ where the Fock states $|n, N-n\rangle$ are the eigenstates with energy $E_n = \frac{U}{2}[N^2 - N - 2n(N-n)]$. From the level diagram shown in Fig. 3.3 we see that the initial state $|0, N\rangle$ is degenerate with the state $|N, 0\rangle$, but detuned from all other intermediate states by the interaction energy. In the interaction-dominated regime $U/J \gg 1$ we can include tunneling perturbatively, and the two states $|0, N\rangle$ and $|N, 0\rangle$ are coupled by a N-th order tunneling process. They hybridize to form the eigenstates $\frac{|0,N\rangle\pm|N,0\rangle}{\sqrt{2}}$ with energy splitting ΔE. This leads to the observed many-particle transitions with many-body tunneling time $T = 2\pi\hbar/\Delta E$.

To calculate the energy splitting ΔE in first non-vanishing order, we project the Hamiltonian (3.1) onto the subspace spanned by $\{|0, N\rangle, |N, 0\rangle\}$

$$\hat{H}_{2\times2} = \begin{pmatrix} 0 & \Delta_N \\ \Delta_N & 0 \end{pmatrix}. \tag{3.3}$$

The coupling between the two degenerate many-particle states $|0, N\rangle$ and $|N, 0\rangle$ is

$$\Delta_N = \frac{H_{0,1}H_{1,2}\ldots H_{N-1,N}}{(E_0 - E_1)(E_0 - E_2)\ldots(E_0 - E_{N-1})} \tag{3.4}$$

with $H_{i,i+1} = \langle i, N-i|\hat{H}|i+1, N-i-1\rangle = -J\sqrt{(i+1)(N-i)}$, and we thus obtain for the energy splitting ΔE

$$\Delta E = 2\Delta_N = 4U\left(\frac{J}{2U}\right)^N \frac{N}{(N-1)!}. \tag{3.5}$$

We see that with increasing number of particles N the energy splitting ΔE decreases and thus the many-particle tunneling time T increases dramatically.

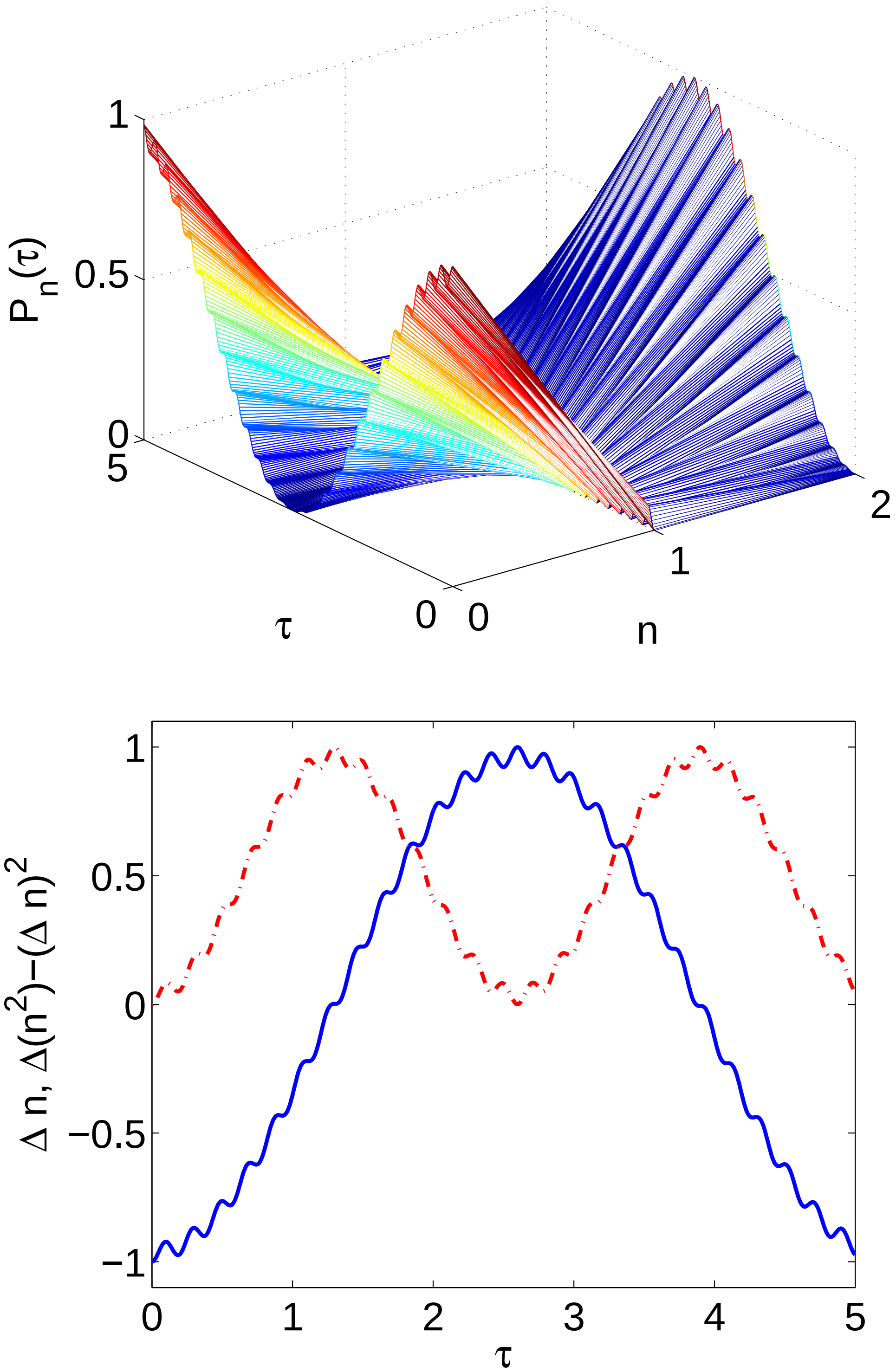

Fig. 3.2: *Many-particle transitions.* **(a)** Atom number distribution $P_n(\tau)$ and **(b)** mean number difference Δn (solid line) as well as its variance σ^2 (dashed-dotted line) for $U/J = 10$ and $N = 2$.

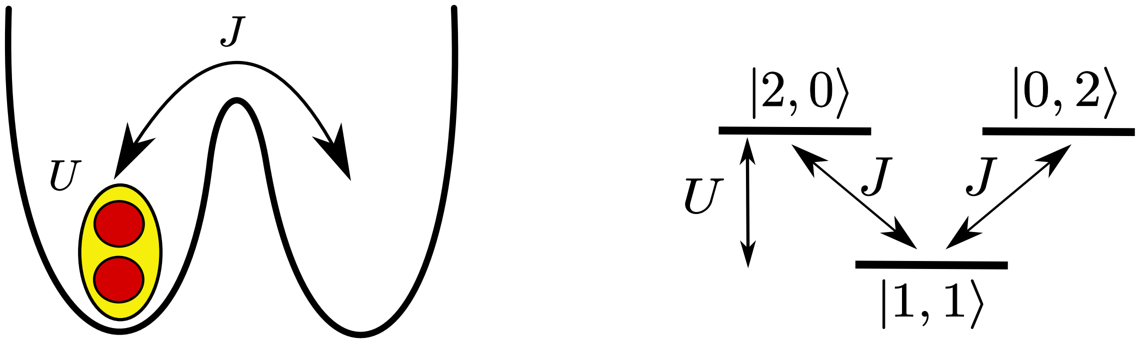

Fig. 3.3: (Left) Correlated tunneling in a double-well potential and (right) the energy level diagram for $N = 2$ particles (right)

3.5 Conclusion

We have studied the tunneling dynamics of ultracold bosons in double-well potentials and identified two different regimes: single-particle Rabi oscillations in the non-interacting and correlated tunneling in the strongly-interacting limit. We found that the many-particle tunneling time increases dramatically with the number of particles. For this reason this scheme will be limited to few-particle superpositions for typical experimental time scales. Using an array of double-well potentials, a large number of such few-particle superposition states can be produced in parallel.

Chapter 4

Macroscopic superposition states in rotating ring lattices

In this chapter, we investigate the effects of rotation on ultracold bosons confined to one-dimensional ring lattices. We find that at commensurate filling there exists a critical rotation frequency, at which the ground state of the weakly-interacting gas is fragmented into a macroscopic superposition of different quasi-momentum states. We demonstrate that the generation of such superposition states using slightly non-uniform ring lattices has several practical advantages. Finally, we show that different quasi-momentum states can be distinguished in time-of-flight absorption imaging and propose to probe correlations via the many-body oscillations induced by a sudden change in the rotation frequency.

4.1 Introduction

Macroscopic superposition states, to which we will refer in this thesis as (Schrödinger) cat states, are one class of strongly-correlated states which has attracted much interest since the early days of quantum theory [73]. Apart from foundational questions [24] they have been shown to enable precision measurements at the Heisenberg limit [74] and serve as resources for various quantum information tasks [75]. Efficient cat state production is therefore an issue of theoretical and practical importance.[1]

Among theoretical proposals for creating cat states with Bose-Einstein condensates [76, 77, 78, 79] one is to load ultracold bosons into rotating ring lattices [80, 81, 82]. In the first part of this chapter, we study the effects of rotation on the ground state properties of bosonic atoms confined to a one-dimensional ring [29]. For commensurate fill-

[1] Parts of this chapter were published as Refs. [28, 29]. In the joint publication [28] I have written the entire text apart from Sec. 4.6 which was contributed by Dr Ana Maria Rey.

ing and weak interactions there is a critical rotation frequency, at which the ground and first excited states are the symmetric and anti-symmetric superposition states of opposite circulation. Their energy difference turns out to decrease exponentially with increasing number of particles [82]. This makes it hard to observe this effect even in systems with small numbers of particles. In the second part of this chapter, we point out several advantages for a slightly non-uniform lattice setup [28]: the energy gap scales less severely with the number of particles, the superposition states are less sensitive to detunings away from the critical rotation frequency compared to the uniform case, and cat state production is not limited to commensurate filling. In the third and final part of this chapter, we discuss how to probe cat-like correlations via many-body oscillations induced by a sudden change in the rotation frequency and show that different quasi-momentum states can be distinguished in time-of-flight absorption images [28].

After this work was published in Refs. [28, 29], we became aware of a related article [83]. The authors study the quantum dynamics of a vortex in a Bose gas with repulsive interactions in an anisotropic, harmonic trap. They show that the circulation of the vortex can undergo periodic reversals by quantum tunneling. With increasing particle number vortices become more stable and the period for reversals increases.

4.2 Ultracold bosons in rotating ring lattices

Optical ring lattices can be created with Laguerre-Gaussian (LG) laser beams, as proposed in Ref. [84] and realized in Ref. [85]. LG beams can be derived from ordinary Gaussian beams, e.g. by means of computer-generated phase holograms [86]. A LG_l mode with frequency ω, wave-vector k and amplitude E_0 propagating along the z-axis can be written in cylindrical coordinates (r, φ, z) as

$$E_l\,(r, \varphi, z, t) = E_0 A_l(r) e^{il\varphi} e^{i(\omega t - kz)} \tag{4.1}$$

with $A_l(r) = \sqrt{\frac{2}{\pi|l|!}}\xi^{|l|}L_{|l|}\left(\xi^2\right)e^{-\xi^2}$ and $\xi = \sqrt{2}r/r_0$, where r_0 is the waist of the beam and $L_{|l|}$ are the Laguerre polynomials.

There are several possible experimental setups to realize rotating ring (super)lattices: The lattice modulation in the $x-y$ plane can be obtained by interfering either a LG_l beam with a co-propagating plane wave $E_0e^{i(\omega t-kz)}$ or a LG_{l_1} and a LG_{l_2} beam with different l-values. Examples of (dark and bright) ring lattice potentials are shown in Fig. 4.1. The interferograms are periodic in φ with l and $\delta l = |l_1 - l_2|$ wells, respectively. Confinement along the z-direction can be achieved either by reflecting the combined beam back on itself, which creates a series of disk shaped traps, or an independent 1D optical lattice potential. By controlling the tunneling between the disks and making it much smaller than the corresponding tunneling within each ring, one can implement an array of effective 1D ring lattices. If a frequency shift $\delta\omega$ is introduced between the two beams comprising the ring lattice, it will start rotating at frequency $\delta\omega$. In case of retroflected beams it will also start translating along the z-axis at a speed $\Delta\omega\lambda/(4\pi)$ [85]. Alternatively, the phase twist along the ring can come about due to an external cylindrical-symmetric magnetic field [84]. Superlattices can be realized by superimposing two independent rotating ring lattices with different number of lattice sites $L_1 = 2L_2$. A conceptionally different approach to arbitrary 2D potentials are spatial light modulators which have recently been used for dynamical manipulation of BECs [87].

We consider a system of N ultracold bosons with mass M confined in a 1D ring lattice of L sites with lattice constant d. The ring is rotated in its plane (about the z-axis) with angular velocity Ω. By subtracting the rotation energy $\hat{H}_{\mathrm{rot}} = \int d\mathbf{x}\,\hat{\Phi}^\dagger\Omega\hat{L}_z\hat{\Phi}$ we go into the rotating frame where the potential $V(\mathbf{x})$ is time-independent and the many-body Hamiltonian is given by [88, 82]

$$\hat{H} = \int d\mathbf{x}\hat{\Phi}^\dagger\left[-\frac{\hbar^2}{2M}\nabla^2 + V(\mathbf{x}) + \frac{4\pi\hbar^2 a_s}{2M}\hat{\Phi}^\dagger\hat{\Phi} - \Omega\hat{L}_z\right]\hat{\Phi}. \tag{4.2}$$

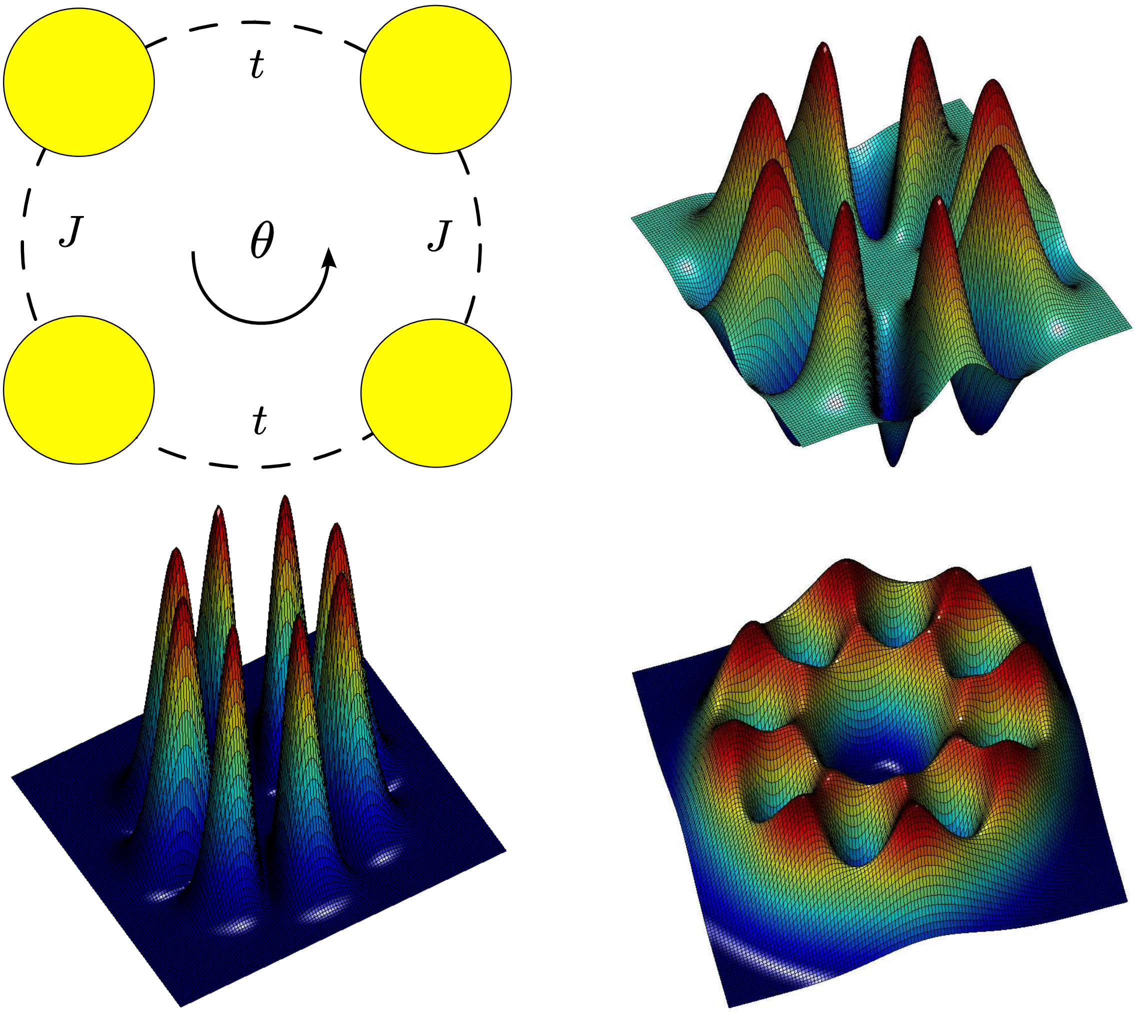

Fig. 4.1: (Upper left) One-dimensional ring lattice with $L = 4$ sites and alternating tunneling matrix elements J and t. In the rotating frame an effective phase twist θ is induced. The remaining figures show various ring lattice potentials $V(r, \varphi)$: (a) from interfering one LG $_{l=8}$ beam with a plane wave $E_0 e^{i(\omega t - kz)}$ (upper right), (b) bright ring lattice from interfering $\mathrm{LG}_{l_1=4}$ and $\mathrm{LG}_{l_1=-4}$ (lower left) and (c) dark ring lattice from interfering $\mathrm{LG}_{l_1=3}$ and $\mathrm{LG}_{l_1=11}$ with adjusted relative intensities [85] (lower right).

In this expression, a_s is the s-wave scattering length, $V(\mathbf{x})$ the lattice potential, $\hat{L}_z$ the angular momentum and $\mathbf{x}$ the 3D spatial coordinate vector. $\hat{\Phi}(\mathbf{x})^\dagger$ and $\hat{\Phi}(\mathbf{x})$ are bosonic creation and annihilation field operators satisfying the canonical commutation relations: $\left[\hat{\Phi}(\mathbf{x}), \hat{\Phi}^\dagger(\mathbf{x}')\right] = \delta(\mathbf{x} - \mathbf{x}')$ and $\left[\hat{\Phi}(\mathbf{x}), \hat{\Phi}(\mathbf{x}')\right] = \left[\hat{\Phi}^\dagger(\mathbf{x}), \hat{\Phi}^\dagger(\mathbf{x}')\right] = 0$.

Assuming that the lattice potential $V(\mathbf{x})$ confines the motion along the z-axis and the radial direction in the $x - y$ plane so strongly that only the motion of the atoms along the ring has to be taken into account and that the lattice is deep enough to restrict tunneling between nearest-neighbor sites and that the band gap is larger than the rotational energy, the bosonic field operator $\hat{\Phi}$ can be expanded in Wannier orbitals confined to the first band $\hat{\Phi} = \sum_j \hat{a}_j W'_j(\mathbf{x})$, where $W'_j(\mathbf{x})$ are the Wannier orbitals in the presence of rotation and $\hat{a}_j$ the bosonic annihilation operator of a particle at site j. We recall that the Hamiltonian of a neutral particle in a frame rotating at frequency Ω around the z-axis, $\hat{H} = \hat{\mathbf{p}}^2/2M - \Omega L_z$, is equivalent to the Hamiltonian of a charged particle in a magnetic field along the z-axis, $\hat{H} = (\hat{\mathbf{p}} - \mathbf{A})^2/2M$ with the effective vector potential $\mathbf{A}(\mathbf{x}) = M\Omega(\hat{z} \times \mathbf{x})$. That means, we can first calculate the Wannier orbitals of the stationary lattice $W_j(\mathbf{x})$ and account for the effective vector potential $\mathbf{A}(\mathbf{x})$ via the gauge transformation $W'_j(\mathbf{x}) = \exp\left[\frac{-i}{\hbar}\int_{\mathbf{x}_j}^{\mathbf{x}} \mathbf{A}(\mathbf{x}') \cdot d\mathbf{x}'\right] W_j(\mathbf{x})$.

In terms of these quantities, the many-body Hamiltonian can be written, up to on-site diagonal terms which we neglect for simplicity, as [88, 82]

$$\hat{H} = -\sum_{j=1}^{L} \left(J_j e^{i\theta} \hat{a}^\dagger_{j+1} \hat{a}_j + H.c.\right) + \frac{U}{2} \sum_{j=1}^{L} \hat{n}_j(\hat{n}_j - 1). \tag{4.3}$$

In this expression, $\hat{n}_j = \hat{a}^\dagger_j \hat{a}_j$ is the number operator at site j, θ is the effective phase twist between adjacent sites [89], $\theta \equiv \int_{\mathbf{x}_i}^{\mathbf{x}_{i+1}} \mathbf{A}(\mathbf{x}') \cdot d\mathbf{x}' = \frac{M\Omega L d^2}{h}$, J_j is the hopping energy between nearest-neighbor sites j and $j+1$: $J_j \equiv \int d\mathbf{x} W^*_j \left[-\frac{\hbar^2}{2M}\nabla^2 + V(\mathbf{x})\right] W_{j+1}$, and U the on-site interaction energy: $U \equiv \frac{4\pi a \hbar^2}{M} \int d\mathbf{x}\, |W_j|^4$.

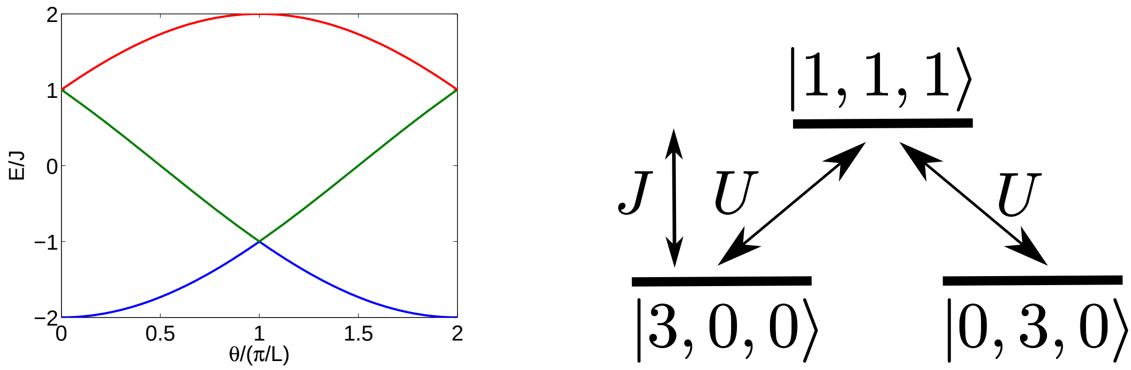

Fig. 4.2: (Left) Single-particle spectrum for $L = 3$ sites as a function of the phase twist θ. There is a single-particle level crossing at $\theta = \pi/L$ [80]. (Right) In the case $N = L = 3$ the interaction Hamiltonian $\hat{H}_{\text{int}}$ couples the degenerate states $|3,0,0\rangle = \frac{1}{\sqrt{3!}}(\hat{b}_0^\dagger)^3|\text{vac}\rangle$ and $|0,3,0\rangle = \frac{1}{\sqrt{3!}}(\hat{b}_1^\dagger)^3|\text{vac}\rangle$ via the intermediate state $|1,1,1\rangle = \hat{b}_0^\dagger\hat{b}_1^\dagger\hat{b}_2^\dagger|\text{vac}\rangle$ [80]. Compare also to Fig. 3.3.

4.3 The uniform ring lattice

We start our discussion with the case of a uniform ring lattice, i.e. $J_j = J$ for all j. To understand the effect of rotation on the atoms in the ring lattice, we write the many-body Hamiltonian (4.3) in terms of the quasi-momentum operators $\hat{b}_q = \frac{1}{\sqrt{L}}\sum_{j=1}^{L}\hat{a}_j e^{-2\pi i q j/L}$, where $2\pi q/dL$ is the quasi-momentum and $q = 0, \ldots, L-1$ an integer. In this basis the Hamiltonian (4.3) has the form [80, 82]

$$\hat{H} = \hat{H}_{\text{sp}} + \hat{H}_{\text{int}} = \sum_{q=0}^{L-1} E_q \hat{b}_q^\dagger \hat{b}_q + \frac{U}{2L}\sum_{q,s,l=0}^{L-1} \hat{b}_q^\dagger \hat{b}_s^\dagger \hat{b}_l \hat{b}_{[q+s-l]\,\text{mod}\,L} \tag{4.4}$$

where $E_q = -2J\cos(2\pi q/L - \theta)$ are the single-particle energies, and the modulus is taken because in collision processes the quasi-momentum is conserved up to an integer multiple of the reciprocal lattice vector $2\pi/d$, i.e. modulo Umklapp processes.

4.3.1 Macroscopic superposition states of different flow

Following Refs. [80] and [82], we show in Fig. 4.2 the single-particle spectrum as a function of the phase twist θ. In the absence of rotation, i.e. $\theta = 0$, the state with zero quasi-momentum $|q = 0\rangle$ is the single-particle ground state. In the rotating system the ground state depends on the phase twist θ. Writing $\theta = \frac{2\pi}{L}m + \frac{\Delta\theta}{L}$ with m an integer and $0 \leq \Delta\theta < 2\pi$, the ground state is the quasi-momentum state $|q = m\rangle$ for $0 \leq \Delta\theta < \pi$ and $|q = m + 1\rangle$ for $\pi < \Delta\theta < 2\pi$.

In the absence of interactions $U = 0$, the ground state of a bosonic many-body system is the state with all N bosons occupying the lowest-energy single-particle state. At rotation frequencies corresponding to phase twists with $\Delta\theta = \pi$, the ground state of the single-particle Hamiltonian $\hat{H}_{\text{sp}}$ is twice degenerate, i.e. $E_m = E_{m+1}$, so that there is a $N + 1$-dimensional degenerate subspace at the N-particle level. A convenient basis for this subspace are the Fock states $|n, N - n\rangle$ with $0 \leq n \leq N$, where n particles are in the quasi-momentum state $|q = m\rangle$ with energy E_m and $N - n$ particles in the quasi-momentum state $|q = m + 1\rangle$ state with energy E_{m+1}, respectively.

For weak interactions, i.e. $U \ll J$, we can use first-order perturbation theory to account for their effect. It predicts that the energies of the states $|n, N - n\rangle$ are

$$E_n^{(1)} = nE_m + (N - n)E_{m+1} + \frac{U}{2L}\left[N^2 - N + 2n(N - n)\right]. \tag{4.5}$$

We see that the degeneracy is lifted and the states of lowest energy are those with $n = 0$ and $n = N$, i.e. $|N, 0\rangle$ and $|0, N\rangle$. These two states remain degenerate in first-order perturbation theory.

At this point it is important whether the number of atoms N is commensurate or incommensurate with the number of lattice sites L. While there are many different paths that couple the states $|N, 0\rangle$ and $|0, N\rangle$ in the commensurate case, in the incommensurate case there is no coupling between these two states and they thus remain degenerate even in higher-order perturbation theory. To understand this fact, let us consider the total quasi-momentum $K = \frac{2\pi}{L}\left|\sum_{q=0}^{L-1} q\hat{b}_q^\dagger\hat{b}_q\right|_{\text{mod}\,L}$. Since the many-body Hamiltonian (4.4) commutes with the quasi-momentum operator $\hat{K}$, i.e. $\left[\hat{H}, \hat{K}\right] = 0$, the Hamiltonian has block diagonal form if the quasi-momentum Fock states are ordered according to the eigenvalues of $\hat{K}$. In the commensurate case, we have $N = nL$ with n an integer, so that the states $|N,0\rangle$ and $|0,N\rangle$ have total quasi-momentum $K = \frac{2\pi}{L}|mnL|_{\mathrm{mod}\,L} = 0$ and $K = \frac{2\pi}{L}|(m+1)nL|_{\mathrm{mod}\,L} = 0$, respectively. Thus both of them belong to the $K = 0$ block and are coupled by the interactions. On the other hand, in the incommensurate case, we have $N = nL + \Delta N$, and hence the two states $|N,0\rangle$ and $|0,N\rangle$ belong to different blocks as $K = |mnL + m\Delta N|_{\mathrm{mod}\,L} \neq |(m+1)nL + (m+1)\Delta N|_{\mathrm{mod}\,L}$, so that they remain degenerate.

In the commensurate case, we construct an effective 2×2 Hamiltonian by projecting the many-body Hamiltonian (4.4) onto the subspace spanned by the states $|N,0\rangle$ and $|0,N\rangle$

$$\hat{H}_{2\times 2} = \begin{pmatrix} E_0^{(1)} & \Delta \\ \Delta & E_N^{(1)} \end{pmatrix} \tag{4.6}$$

where the coupling Δ is given by

$$\Delta = \sum_{i,j,\ldots p} \frac{H_{0i}H_{ij}\ldots H_{pN}}{(E_0^{(1)}-\varepsilon_i)(E_0^{(1)}-\varepsilon_j)\ldots(E_0^{(1)}-\varepsilon_p)} \propto \left(\frac{U}{2L}\right)^{\bar{n}(L-1)}. \tag{4.7}$$

In this expression, $\bar{n} = N/L$ is the number density, the H_{ij} are transition matrix elements introduced by the interaction Hamiltonian $\hat{H}_{\mathrm{int}}$, and ε_i are either given by $E_n^{(1)}$ in Eq. (4.5) or non-interacting many-body eigenenergies depending upon whether the intermediate states are or are not in the $|n, N-n\rangle$ manifold. The factor $\bar{n}(L-1)$ corresponds to the minimum number of collision processes necessary to couple the states $|N,0\rangle$ and $|0,N\rangle$ and the sum is taken over all possible coupling paths. In Fig. 4.2 we show the energy level diagram for the case of $N = 3$ particles on $L = 3$ lattice sites at the phase twist $\theta = \pi/3$.

At the critical phase twist $\Delta\theta = \pi$, we have $E_0^{(1)} = E_N^{(1)}$ and due to the non-zero value of the coupling Δ the symmetric and anti-symmetric superpositions $|\pm\rangle$ become the ground and first excited state separated from each other by an energy gap 2Δ

$$|\pm\rangle = \frac{|0,N\rangle \pm |N,0\rangle}{\sqrt{2}}. \tag{4.8}$$

From Eq. (4.7) we find that the energy gap 2Δ decreases exponentially with increasing number of particles N, so that macroscopic superposition states only occur in the case of finite number of particles N and lattice sites L.

4.3.2 Effects of rotation on the Mott transition

Having explored the effects of rotation on the weakly-interacting regime, we examine in this subsection as to how rotation affects the Mott transition in a finite lattice. To this end, we calculate the momentum distribution $\langle\hat{n}_q\rangle$ as a function of the ratio J/U for various values of the phase twist θ. Our results for a lattice with $L = 6$ sites and $N = 6$ particles are shown in Fig. 4.3. Please note that several curves lie on top of each other. We find that the Mott transition is dramatically changed close to the critical phase twist $\theta_c = \frac{\pi}{L}$. In case of the non-rotating system $\theta = 0$, the occupation numbers of all non-zero momenta $\langle\hat{n}_{q\neq 0}\rangle$ decrease monotonically with decreasing J/U, while the zero-momentum occupation number $\langle\hat{n}_0\rangle$ increases. This means that, as the Mott insulator is melted, the bosons gradually condense into the zero-momentum mode $|q = 0\rangle$. This is not the case for a rotating lattice close to the critical phase twist, where the occupation numbers $\langle\hat{n}_0\rangle$ and $\langle\hat{n}_1\rangle$ both increase as the ratio J/U decreases and remain of similar size up to intermediate values of $J/U \approx 10$. This effect is easily understood from the band structure, which we show in the insets of Fig. 4.3. Close to the critical phase twist, there are two (almost) degenerate low-lying single-particle states, namely the quasi-momentum states $|q = 0\rangle$ and $|q = 1\rangle$. At intermediate interaction strengths these two modes are strongly coupled, so that the bosons cannot condense into the zero momentum mode $|q = 0\rangle$.

Let us now apply the approximations we discussed in Chapter 2 to the case of the rotating ring lattice. In the Bogoliubov approximation [82] the momentum distribution

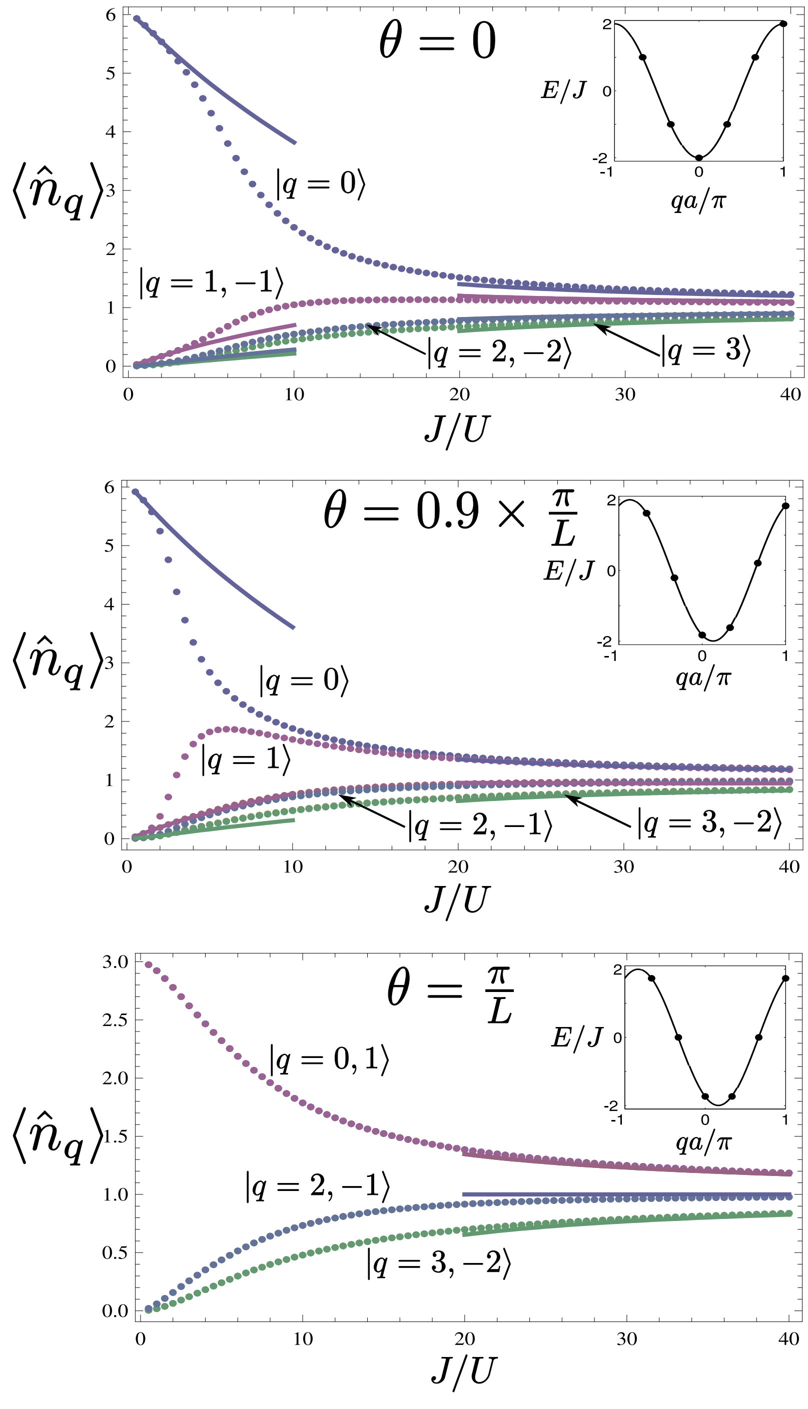

Fig. 4.3: Momentum distribution $\langle \hat{n}_q \rangle$ as a function of the ratio J/U for $\theta/\frac{\pi}{L} = \{0, 0.9, 1\}$ and $N = L = 6$. Please note that several curves lie on top of each other. Apart from the exact results (dotted line) we show the Bogoliubov approximation (4.9) and the strong coupling expansion (4.10) (solid lines at small and large J/U). At the critical phase twist $\theta = \frac{\pi}{L}$ the Bogoliubov approximation breaks down and is not shown. The insets show the single-particle dispersion relation E_q for a lattice with $L = 6$ sites (points) and an infinite lattice (solid line).

has the form

$$\langle \hat{n}_q \rangle = v_q^2 = \frac{\epsilon_q + U\bar{n}}{2\sqrt{\epsilon_q^2 + 2U\bar{n}\epsilon_q}} - \frac{1}{2} \tag{4.9}$$

where $\bar{n} = N/L$ is the number density, $\omega_q = \Lambda_q + \sqrt{\epsilon_q^2 + 2U\bar{n}\epsilon_q}$ denotes the quasi-particle energies with $\Lambda_q = 2J\sin[\frac{2\pi q}{L}]\sin[\frac{\Delta\theta}{L}]$, and the single-particle energies are given by $\epsilon_q = 4J\sin^2[\frac{\pi q}{L}]\cos[\frac{\Delta\theta}{L}]$. We show the Bogoliubov approximation alongside with the exact results in Fig. 4.3. It predicts a slightly increased depletion due to the modified single-particle energies ϵ_q, but the momentum distribution remains symmetric $v_q^2 = v_{-q}^2$ which is incorrect. At the critical phase twist $\theta = \frac{\pi}{L}$ the Bogoliubov approximation breaks down and is therefore not shown in Fig. 4.3. The strong-coupling expansion yields for the momentum distribution

$$\langle \hat{n}_q \rangle = \bar{n} + \frac{2J}{U} \cdot \sqrt{2\bar{n}(\bar{n}+1)} \cdot \cos\left(\frac{2\pi q}{L} - \theta\right). \tag{4.10}$$

This result is also shown in Fig. 4.3. We see that the strong coupling expansion predicts the correct behavior in the strongly-interacting regime $U \gg J$, where the effect of rotation is indeed only of perturbative nature. The bosons do not condense into the zero-momentum mode $|q = 0\rangle$, but the occupation number of the quasi-momentum modes $|q = 0\rangle$ and $|q = 1\rangle$ remain equal: $\langle \hat{n}_0 \rangle = \langle \hat{n}_1 \rangle$. The Gutzwiller ansatz [82] predicts a decrease of the critical value of the Mott insulator transition $(J/U)_c$ by a factor of $\cos(\Delta\theta/L)$. This result is a consequence of the reduced bandwidth $4J \to 4J\cos(\Delta\theta/L)$ in the rotating system, as can be seen from the single-particle spectrum in Fig. 4.4.

Although the effects of rotation we discussed here are absent in the thermodynamic limit, we see that rotation does have a dramatic effect on a small number of ultracold bosons in commensurate rotating ring lattices. Even away from the critical phase twist, strong correlations between the almost degenerate quasi-momentum modes $|q = 0\rangle$ and $|q = 1\rangle$ affect observables such as the quasi-momentum distribution $\langle \hat{n}_q \rangle$ and should be visible in future cold atom experiments.

4.4 Extension to a ring superlattice

Having seen how rotation induced modifications to the Mott transition, we now return to the production of macroscopic superpositions states. We found that for a uniform ring lattice the coupling Δ between the two macroscopic states scales exponentially with increasing number of particles N (see Eq. (4.7)), and that the cat state (4.8) only appears in the case of commensurate numbers. In this section, we explore whether the situation can be improved by introducing a lattice modulation, i.e. we generalize to ring superlattices where $J_j = J$ for j even and $J_j = t$ for j odd.

Due to the superlattice potential the quasi-momentum states $|q\rangle$ and $|q + L/2\rangle$ are coupled and the single-particle Hamiltonian is no longer diagonal in the quasi-momentum basis. Using the decompositions

$$\hat{a}_j = \frac{1}{\sqrt{L}} \sum_{q=0}^{L-1} \mathrm{e}^{\mathrm{i}2\pi qj/L} \hat{b}_q \tag{4.11}$$

along with

$$\frac{1}{L} \sum_{j=0}^{L-1} J_j \mathrm{e}^{-\mathrm{i}2\pi(q-q')j/L} = \begin{cases} -(J+t)/2 & \text{for } q = q' \\ +(J-t)/2 & \text{for } q = q' + L/2 \\ \quad 0 & \text{otherwise} \end{cases} \tag{4.12}$$

we obtain the single-particle Hamiltonian $\hat{H}_{\mathrm{sp}}$ in the quasi-momentum basis, i.e.

$$\hat{H}_{\mathrm{sp}} = \sum_{q=0}^{L/2-1} \begin{pmatrix} \hat{b}_q^\dagger & \hat{b}_{q+L/2}^\dagger \end{pmatrix} \mathbf{M}_q \begin{pmatrix} \hat{b}_q \\ \hat{b}_{q+L/2} \end{pmatrix}. \tag{4.13}$$

Here the two-by-two matrices are given by

$$\mathbf{M}_q = \begin{pmatrix} -(J+t)\cos\left(\theta - \frac{2\pi q}{L}\right) & -i(J-t)\sin\left(\theta - \frac{2\pi q}{L}\right) \\ +i(J-t)\sin\left(\theta - \frac{2\pi q}{L}\right) & +(J+t)\cos\left(\theta - \frac{2\pi q}{L}\right) \end{pmatrix} \tag{4.14}$$

and represent the coupling between the quasi-momentum states. We can diagonalize the single-particle Hamiltonian (4.13) via a unitary basis transformation

$$\begin{pmatrix} \hat{c}_q \\ \hat{c}_{q+L/2} \end{pmatrix} = \begin{pmatrix} \cos\alpha_q & i\sin\alpha_q \\ i\sin\alpha_q & \cos\alpha_q \end{pmatrix} \begin{pmatrix} \hat{b}_q \\ \hat{b}_{q+L/2} \end{pmatrix} \tag{4.15}$$

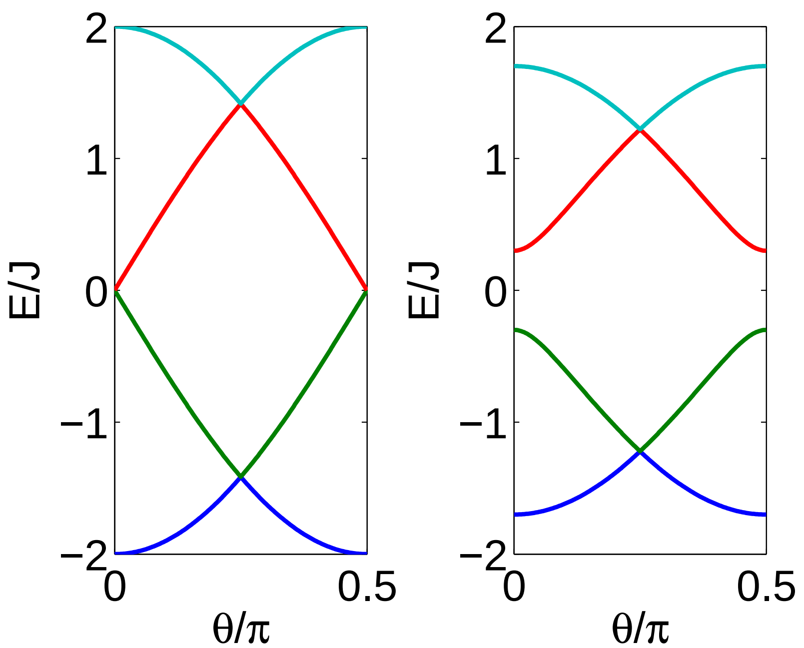

Fig. 4.4: Single-particle spectrum for $L = 4$ sites with $t/J = 1$ (left) and $t/J = 0.7$ (right) as a function of the phase twist θ. In both cases there are level crossings at $\theta = \pi/4$.

with

$$\tan 2\alpha_q = \frac{J-t}{J+t} \cdot \tan\left(\theta - \frac{2\pi q}{L}\right) \tag{4.16}$$

and obtain

$$\hat{H}_{\text{sp}} = \sum_{q=0}^{L/2-1} \begin{pmatrix} \hat{c}_q^\dagger & \hat{c}_{q+L/2}^\dagger \end{pmatrix} \begin{pmatrix} E_q^- & 0 \\ 0 & E_q^+ \end{pmatrix} \begin{pmatrix} \hat{c}_q \\ \hat{c}_{q+L/2} \end{pmatrix} \tag{4.17}$$

where the single-particle energies are given by

$$E_q^{\pm} = \pm\sqrt{J^2 + t^2 + 2Jt\cos\left(2\theta - \frac{4\pi q}{L}\right)}. \tag{4.18}$$

In the uniform ring, $t/J = 1$, the eigenstates of the single-particle Hamiltonian $\hat{H}_{\text{sp}}$ are quasi-momentum states. At certain phase twists θ they are twice degenerate. For example, for $L = 4$ sites the quasi-momentum states $|q = 1\rangle$ and $|q = -1\rangle$ are degenerate at $\theta = 0$, whereas at $\theta = \pi/4$ the states $|q = 0\rangle$ and $|q = 1\rangle$ as well as $|q = 2\rangle$ and $|q = -1\rangle$ are degenerate. Reducing the symmetry of the ring by choosing $t \neq J$ the quasi-momentum states which differ by $L/2$ quasi-momentum units are coupled by the single-particle Hamiltonian (4.13), so that the quasi-momentum states $|q = 1\rangle$ and $|q = -1\rangle$ hybridize and the degeneracy at $\theta = 0$ is lifted, i.e. $E_1^+ - E_1^- = 2(J - t)$.

At $\theta = \pi/4$ however the degenerate quasi-momentum states are not coupled by the single-particle Hamiltonian (4.13), so that the degeneracy is present also in the non-uniform case. This remains true for arbitrary L, i.e. $E_0^- = E_{L/4}^-$ at $\theta = \pi/4$, but for $L \neq 4$ these states are not the ground states of the system. In Fig. 4.4 we plot the single-particle spectrum for $L = 4$ sites as a function of the effective phase twist θ. It shows level crossings at $\theta = \pi/4$ both for $t = J$ as well as $t \neq J$. In the following we will refer to $\theta = \pi/4$ as the critical phase twist, since – as we will demonstrate below – weak on-site interactions lift the degeneracy at $\theta = \pi/4$ and lead to the formation of strongly-correlated states in the many-body system.

4.4.1 Effective many-body Hamiltonian

In this section we derive an effective many-body Hamiltonian to study the properties of the many-body system in the limit of weak on-site interactions. In the absence of interactions $U = 0$ the ground state of a bosonic many-body system is the state with all bosons occupying the lowest-energy single-particle state. At the critical phase twist $\theta = \pi/4$ the single-particle Hamiltonian (4.13) has, however, two degenerate single-particle states, so that there is a $N + 1$-dimensional degenerate subspace at N-particle level. A convenient basis for this subspace is given by the Fock states $|n, N - n\rangle$ with $0 \leq n \leq N$, where n particles are in the single-particle state of energy E_0^- and $N - n$ particles in the one of energy $E_{L/4}^-$, respectively. For weak interactions $NU/L \ll 2\sqrt{J^2 + t^2}$ this subspace is the low-energy sector of the many-body problem for all phase twists θ and tunneling strength ratios t/J.

Starting from the interaction Hamiltonian

$$\hat{H}_{\text{int}} = \frac{U}{2}\sum_{j=1}^{L} \hat{a}_j^\dagger \hat{a}_j^\dagger \hat{a}_j \hat{a}_j = \frac{U}{2L}\sum_{k_1,k_2,k_3=0}^{L-1} \hat{b}_{k_1}^\dagger \hat{b}_{k_2}^\dagger \hat{b}_{k_3} \hat{b}_{[k_1+k_2-k_3]\,\mathrm{mod}\,L} \tag{4.19}$$

we first restrict the sum in Eq. (4.19) to the relevant modes $k_i \in \{0, L/4, L/2, 3L/4\}$ with $i = \{1, 2, 3\}$ and second use the inverse of Eq. (4.15) to express the operators $\hat{b}_q$ in terms of the operators $\hat{c}_q$. Keeping only terms within the low-energy subspace we obtain the effective Hamiltonian up to first order in the on-site interaction strength U

$$\hat{H}_{\text{eff}} = \left(E_0^- \hat{n}_0 + E_{L/4}^- \hat{n}_{L/4}\right) + \frac{U}{2L}\left(N^2 - N + 2\hat{n}_0\hat{n}_{L/4}\right) + \left(\frac{i\eta U}{2L}\hat{c}_0^\dagger \hat{c}_0^\dagger \hat{c}_{L/4}\hat{c}_{L/4} + H.c.\right) \tag{4.20}$$

where $\hat{n}_q = \hat{c}_q^\dagger \hat{c}_q$ are the number operators and the parameter

$$\eta = 2\left(\cos\alpha_0 \sin\alpha_0 \cos 2\alpha_{L/4} + \cos\alpha_{L/4}(-\sin\alpha_{L/4})\cos 2\alpha_0\right) \tag{4.21}$$

satisfies $0 \le \eta \le 1$ and simplifies for $\theta = \pi/4$ to

$$\eta = \frac{J^2 - t^2}{J^2 + t^2}. \tag{4.22}$$

The first bracket of Eq. (4.20) contains the contributions from the single-particle Hamiltonian (4.17), whereas the terms in the second and third brackets arise from the on-site interaction (4.19). At the critical phase twist $\theta = \pi/4$ the former are an unimportant zero-energy offset, whereas the terms in the second bracket shift the energies of the states in the subspace differently, e.g. they lead to an energy difference of $U(N-1)/L$ between the states $|N, 0\rangle$ and $|N-1, 1\rangle$, while the states $|n, N-n\rangle$ and $|N-n, n\rangle$ remain pairwise degenerate. The terms in the third bracket are off-diagonal in the Fock basis of the subspace and describe two-particle scattering between the two single-particle modes. As we will see in the next section they lift the remaining pairwise degeneracies in the many-body spectrum. In Fig. 4.5 we plot the many-body spectrum for $L = N = 4$, $t/J = 0.7$ and $U/J = 0.5$ as a function of the phase twist θ obtained from exact diagonalization of (4.3) and the effective Hamiltonian (4.20). We see that for these parameters the effective Hamiltonian (4.20) is an excellent approximation for the low-energy sector of the many-body Hamiltonian (4.3).

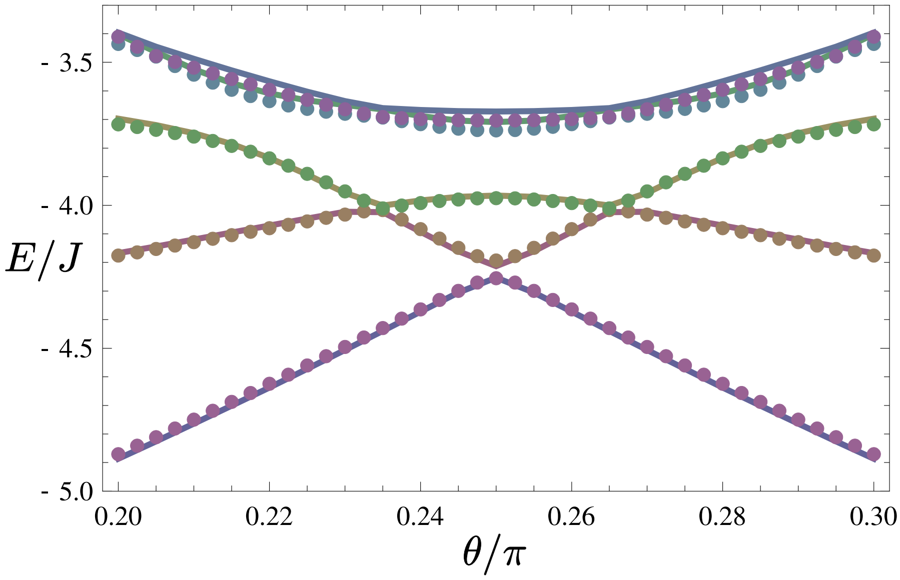

Fig. 4.5: Many-body spectrum for $L = N = 4$, $t/J = 0.7$ and $U/J = 0.5$ as a function of the phase twist θ obtained from exact diagonalization (dotted lines) of the many-body Hamiltonian (4.3) as well as from the effective Hamiltonian (4.20) (solid lines).

4.4.2 Cat-like superpositions for slightly non-uniform rings

Let us now determine the ground and first excited state for slightly non-uniform rings $t/J \approx 1$, close to the critical phase twist $\theta \approx \pi/4$. Since the terms in the second bracket of Eq. (4.20) increase the energy for all states in the subspace apart from $|N, 0\rangle$ and $|0, N\rangle$ and the coupling between the states is weak (as the coupling η is small in this limit), we project the effective Hamiltonian (4.20) onto the subspace spanned by these two nearly-degenerate lowest-energy states.

As there is no direct coupling between $|N, 0\rangle$ and $|0, N\rangle$ we calculate the total coupling through intermediate states using perturbation theory. After eliminating the intermediate states we obtain the following 2×2 Hamiltonian

$$\hat{H}_{2\times 2} = \begin{pmatrix} \Delta E/2 + \xi & \Delta \\ \Delta^* & -\Delta E/2 + \xi \end{pmatrix} \tag{4.23}$$

where ΔE is the energy difference between the states $|N, 0\rangle$ and $|0, N\rangle$ caused by the detuning of the phase twist from resonance $\Delta\theta = \theta - \pi/4$, i.e.

$$\Delta E = N(E^{-}_{L/4} - E^{-}_{0}) \approx \frac{4JtN\Delta\theta}{\sqrt{J^2 + t^2}}, \tag{4.24}$$

and Δ is the coupling between the states $|N, 0\rangle$ and $|0, N\rangle$ due to the off-diagonal terms of the effective Hamiltonian (4.20). As the latter only directly couples the states $|n, N - n\rangle$ and $|n \pm 2, N - n \mp 2\rangle$, the first non-vanishing order is given by

$$\Delta = \frac{\langle N, 0|\hat{H}_{\text{eff}}^{N/2}|0, N\rangle}{\prod_{j=1}^{N/2-1}(E^{(1)}_{0} - E^{(1)}_{2j})} = \frac{U}{L} \cdot \left(\frac{i\eta}{2}\right)^{N/2} \cdot \frac{N!}{\prod_{j=1}^{N/2-1}(2j)^2}. \tag{4.25}$$

Here, $E^{(1)}_{n} = \frac{U}{2L}[N^2 - N + 2n(N - n)]$ is the diagonal interaction energy shift. Finally, the term ξ in Eq. (4.23) is the energy shift induced by the non-diagonal terms in the effective Hamiltonian (4.20)

$$\begin{aligned}\xi = &- \frac{|\langle N, 0|\hat{H}_{\text{eff}}|N - 2, 2\rangle|^2}{(E^{(1)}_{0} - E^{(1)}_{2})} + \left(\frac{|\langle N, 0|\hat{H}_{\text{eff}}|N - 2, 2\rangle|^4}{(E^{(1)}_{0} - E^{(1)}_{2})^3}\right. \\ &\left.- \frac{|\langle N, 0|\hat{H}_{\text{eff}}|N - 2, 2\rangle|^2|\langle N - 2, 2|\hat{H}_{\text{eff}}|N - 4, 4\rangle|^2}{(E^{(1)}_{0} - E^{(1)}_{2})^2(E^{(1)}_{0} - E^{(1)}_{4})}\right) + \ldots\end{aligned} \tag{4.26}$$

As ξ is just a constant in the 2×2 subspace we do not need to evaluate it explicitly and neglect it hereafter.

The ground state of the two-by-two Hamiltonian (4.23) is given by

$$\frac{c_0|N, 0\rangle + i^{N/2}c_N|0, N\rangle}{\sqrt{2}} \tag{4.27}$$

where the ratio of its amplitudes is given by

$$\frac{c_0}{c_N} = \frac{\Delta E - \sqrt{(\Delta E)^2 + |2\Delta|^2}}{|2\Delta|} \tag{4.28}$$

and the energies of the ground and excited states are $E_{\pm} = \pm\sqrt{\Delta E^2 + |2\Delta|^2}/2$. We see that to obtain a cat-like superposition, i.e. $c_0/c_N \approx 1$, the energy difference must not dominate over the coupling $|\Delta E| \ll |2\Delta|$. In this limit the energy gap $E_+ - E_-$ is given by $E_+ - E_- \approx |2\Delta|$.

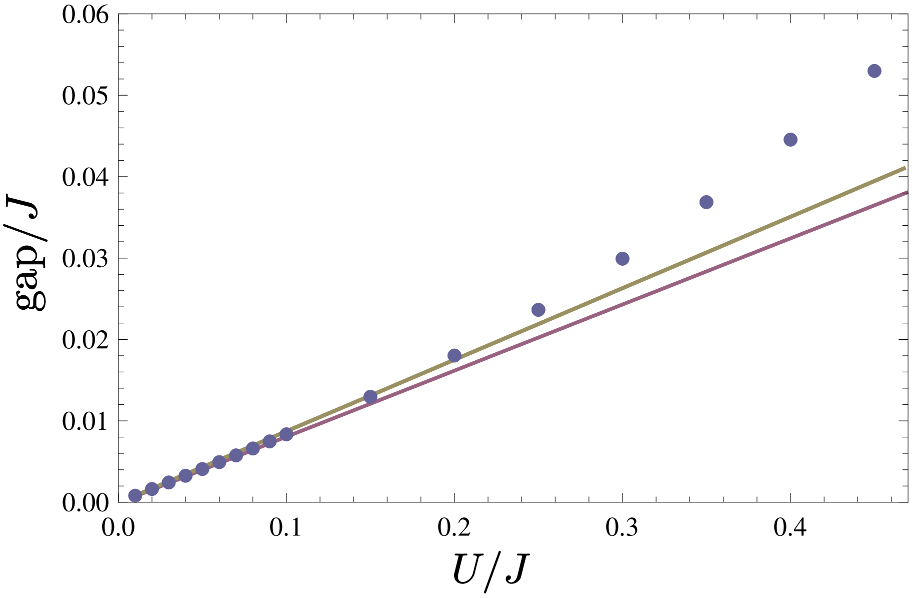

Fig. 4.6: Energy gap for $L = N = 4$, $t/J = 0.7$, $\theta = \pi/4$ as a function of U/J from exact diagonalization (blue points), effective Hamiltonian (red line) and the gap formula (yellow line).

In Fig. 4.6 we plot the energy gap between the two lowest-energy states of the many-body spectrum as a function of the on-site interaction U/J for $L = N = 4$, $t/J = 0.7$ and $\theta = \pi/4$. We find that the analytic formula (4.7) agrees very well with the diagonalization of the effective Hamiltonian (4.20) and at small interaction strengths $U < 0.2$ also with the exact diagonalization of the full many-body Hamiltonian (4.3).

In order to understand the influence of the superlattice potential on the formation of the cat state, we show in Fig. 4.7, for the example of $N = 4$ particles on $L = 4$ lattice sites, the *quasi-momentum* states $|n_{q=0}, n_{q=1}, n_{q=2}, n_{q=3}\rangle$ which contribute to the ground and first excited state in lowest non-vanishing order of perturbation theory. Solid lines signify coupling due to the interaction Hamiltonian $\hat{H}_{\text{int}}$ which is present in uniform ring lattices ($J = t$) as well as ring superlattices ($J \neq t$); dashed lines stand for the coupling due to the off-diagonal part of the single-particle Hamiltonian $\hat{H}_{\text{sp}}$ induced by the superlattice. The three states $|3, 0, 1, 0\rangle$, $|0, 3, 0, 1\rangle$ and $|2, 2, 0, 0\rangle$ have total quasi-momentum $K = 2$ and are not coupled to the states $|4, 0, 0, 0\rangle$ and $|0, 4, 0, 0\rangle$ in the case of the uniform ring lattice.

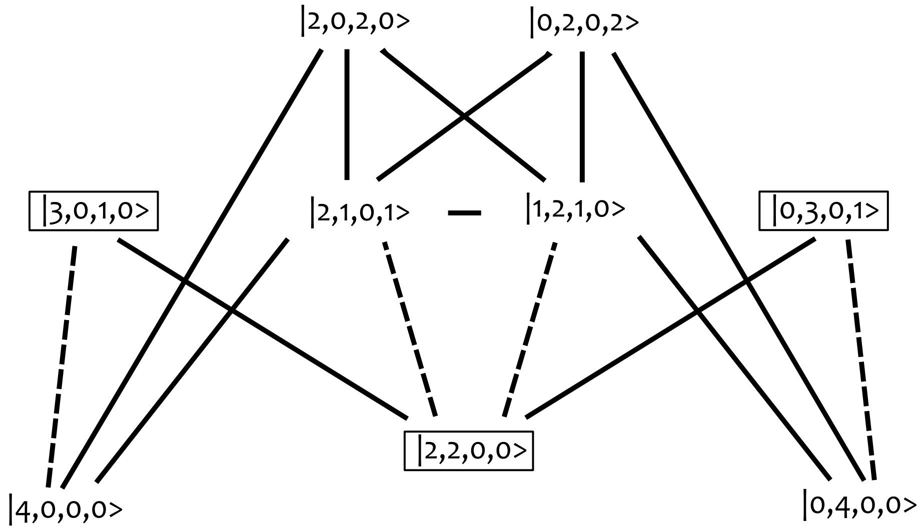

Fig. 4.7: For $N = 4$ particles on $L = 4$ lattice sites, we show the non-zero matrix elements between the quasi-momentum states $|n_{q=0}, n_{q=1}, n_{q=2}, n_{q=3}\rangle$. Solid lines signify coupling due to scattering $\hat{H}_{\mathrm{int}}$ and dashed lines due to the off-diagonal part of the single-particle Hamiltonian $\hat{H}_{\mathrm{sp}}$ in case of the superlattice ($J \neq t$). We only show states which contribute in lowest non-vanishing order of perturbation theory to the cat state at the critical phase twist. All states with(out) box have total quasi-momentum $K = 2$ ($K = 0$).

They introduce four efficient coupling paths involving only $N/2 = 2$ scattering processes where the intermediate state $|2, 2, 0, 0\rangle$ lies in the degenerate subspace.

Let us compare our result (4.25) with the coupling Δ in the case of a uniform ring lattice (4.7) ($t = J$). Unfortunately, an analytic expression equivalent to Eq. (4.25) has not been found in this case, but we see from Eq. (4.7) that the coupling Δ in first non-vanishing order for unity filling $N/L = 1$ is proportional to $\Delta/J \propto (\frac{U}{2LJ})^{N-1}$. In both cases the coupling Δ decreases exponentially with the number of particles N. This is because multiple two-particle scattering processes are the microscopic origin of the coupling Δ and transitions between the two configurations $|N, 0\rangle$ and $|0, N\rangle$ are thus highly off-resonant $N/2$-th and $N - 1$-th order processes, respectively. Consequently, the energy gap vanishes in the thermodynamic limit $N \to \infty$ and cat state production both in uniform and slightly non-uniform ring lattices is restricted to modest numbers of atoms. However,

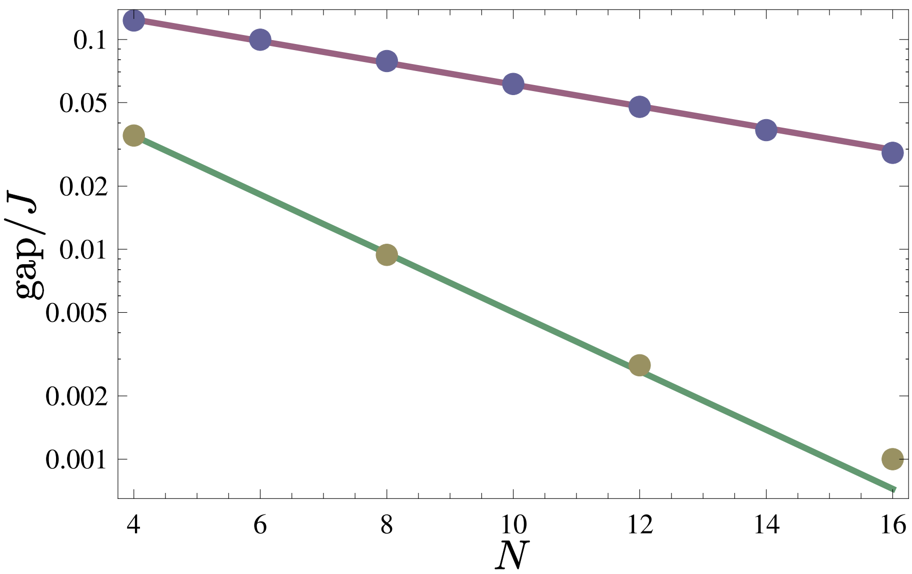

Fig. 4.8: Energy gap as a function of particle number N with $t/J = 0.7$ (upper curve) and $t/J = 1$ (lower curve) for the ring of $L = 4$ sites and $U/J = 0.5$. The solid lines are exponential fits to guide the eye.

since the energy gap in first non-vanishing order is proportional to $U(\eta/2)^{N/2}$ for slightly non-uniform rings as compared to $U(U/J)^{N-1}$ for uniform rings, it can be one order of magnitude bigger in the relevant parameter regime. Furthermore, we point out that the appearance of cat states in slightly non-uniform rings is not limited to commensurate filling as long as the number of particles N is even.

In Fig. 4.8 we plot the energy gap $L = 4$ and $U/J = 0.5$ as a function of number of particles N for $t/J = 0.7$ and $t/J = 1$. The solid line is an exponential fit to the points to guide the eye. We see that by changing from $t/J = 1$ to $t/J = 0.7$ the energy gap increases by over one order of magnitude for numbers of particles $N \geq 8$. As experiments are typically limited to 1s and typical hopping energies are of order of $0.05E_r \sim 10^2$Hz, the detection of cat states by non-equilibrium dynamics is limited to $\Delta/J = 10^{-2}$. This in turn restricts our cat-state production scheme to a few tens of particles in contrast to less than ten particles for uniform ring lattices (see Fig. 4.8).

4.4.3 Product states in the limit of isolated double-well potentials

Let us now try to understand the properties of the slightly non-uniform ring by looking at the opposite limit $t/J = 0$ where the system becomes an array of $L/2$ isolated double-well potentials. In this section we will focus on the case of $L = 4$ sites for notational convenience, but our arguments are valid for all L and N.

Since the double-wells are isolated for $t/J = 0$, we can treat the atoms in each double-well separately. Without interactions $U = 0$ the states $|n, N-n\rangle$ ($0 \leq n \leq N$) with n atoms in the ground state of the first and $N-n$ in the ground state of the second double-well have the same single-particle energy. In first-order perturbation theory the on-site interaction shifts the ground state energy of a double-well with n particles by $U/2 \cdot n(n-1)/2$ and thus breaks this degeneracy. The energies of the states $|n, N-n\rangle$ become

$$E_n^{(1)} = \frac{U}{4} \cdot \Big(N^2 - N - 2n(N-n)\Big). \tag{4.29}$$

As expected, repulsive interactions favor states of equal numbers in the two double-wells, so that the states $|N/2, N/2\rangle$ and $|N/2 \pm 1, N/2 \mp 1\rangle$ are the lowest-lying states. The energy difference between the ground and the two-fold degenerate excited state is thus $U/2$. We note that the opposite sign of the energy shift due to the on-site interaction in Eqs. (4.20) and (4.29) stem from the two different single-particle basis sets used to span the two-mode Fock states[2].

In Fig. 4.9 we compare the excitation energies of the effective Hamiltonian (4.20) with the full many-body Hamiltonian (4.3) as a function of t/J and find that they agree for all ratios t/J. Furthermore, we see that in the limit $t/J \to 0$ the excitation energies agree

[2] One simple example where this effect occurs is the two-mode approximation for N particles in a double-well potential. In the site basis $|n_L, N-n_L\rangle$ with n_L particles on the left and $N-n_L$ particles on the right-hand side of the double-well, the energy shift due to the on-site interaction Hamiltonian (4.19) is $\langle n_L, N-n_L|\hat{H}_{\mathrm{int}}|n_L, N-n_L\rangle = U/2 \cdot (N^2 - N - 2n_L(N-n_L))$ which shows the minus sign similar to Eq. (4.29). Changing the single-particle basis set to quasi-momentum states using $\hat{b}_\pm = (\hat{a}_L \pm \hat{a}_R)/\sqrt{2}$ we obtain $\langle n_+, N-n_+|\hat{H}_{\mathrm{int}}|n_+, N-n_+\rangle = U/4 \cdot (N^2 - N + 2n_+(N-n_+))$ where n_+ particles are in the symmetric and $N-n_+$ particles are in the anti-symmetric orbital and which shows the plus sign similar to Eq. (4.20).

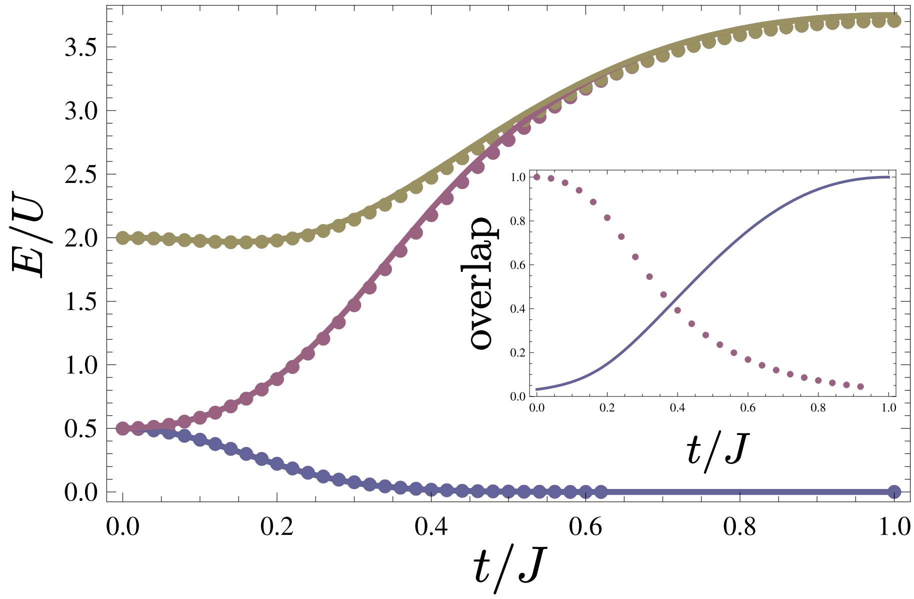

Fig. 4.9: Excitation energies for $L = 4$, $N = 16$ and $\theta = \pi/4$ as a function of t/J from the effective Hamiltonian (4.20) (solid line) and the full Hamiltonian (4.3) (dotted line). The inset shows for the same parameters the overlap of the ground state with the ground state of the isolated double-wells $t/J = 0$ (red dotted line) as well as the uniform ring $t/J = 1$ (blue solid line) as a function of t/J.

with the picture of the isolated double-wells. In the inset of Fig. 4.9 we plot the overlap of the ground state of the system with the ground state of the isolated double-wells $t/J = 0$ as well as the uniform ring $t/J = 1$. We find that as the ratio t/J decreases, the overlap with the cat-like superposition of two quasi-momentum states decreases while the overlap with the ground state of the isolated double-wells increases.

We further note that in the limit $t/J \to 0$ the physics is independent of the number of particles N and the applied phase twist θ (see Eq. (4.18)). As the exact ground state of the effective Hamiltonian (4.20) for arbitrary t/J and N is very non-trivial, a legitimate way to gain some physical insight about its properties is to interpolate between the two limits discussed above. Using this perspective one can attribute the less severe scaling of the energy gap with the number of particles, to hybridization of the cat and product states.

4.4.4 Bigger energy gaps and weaker sensitivity

A fair comparison between cat state production in uniform and non-uniform ring lattices has to contrast the gain in energy gap with the degradation of the cat fidelity or "cattiness". To quantify the "cattiness" of a quantum state we consider two measures: (i) we define the cattiness of the first kind as the overlap of the ground state with the quasi-momentum cat state

$$|\psi_1\rangle = \frac{1}{\sqrt{2N!}}\left[\left(\hat{b}_0^\dagger\right)^N + \left(\hat{b}_{L/4}^\dagger\right)^N\right]|\mathrm{vac}\rangle \tag{4.30}$$

and (ii) we define the cattiness of the second kind as the overlap of the ground state with the cat-like superposition of the two single-particle modes

$$|\psi_2\rangle = \frac{1}{\sqrt{2N!}}\left[\left(\hat{c}_0^\dagger\right)^N + i^{N/2}\left(\hat{c}_{L/4}^\dagger\right)^N\right]|\mathrm{vac}\rangle \tag{4.31}$$

which depends on the ratio t/J as defined in Eq. (4.15).

In this section we demonstrate that while there is a trade-off between bigger energy gaps and cattiness of the first kind, non-uniform ring lattices offer bigger energy gaps at fixed cattiness of the second kind. Consequently, they are less sensitive to detunings of the rotation frequency which is an important practical advantage. On the other hand it is clear that to detect a cat state in two single-particle modes which do not have well defined quasi-momentum is more demanding experimentally.

Both cat-state measures can be calculated perturbatively in the limit of weakly non-uniform rings $t/J \approx 1$ and weak on-site interactions $U/J \ll 1$. The quasi-momentum cat state $|\psi_1\rangle$ is the ground state for $t/J = 1$ and $U/J \to 0$. Deviations are due to the off-diagonal part of the single-particle Hamiltonian in quasi-momentum representation (4.13) as well as the on-site interactions (4.19). We obtain for the overlap

$$|\langle\psi_1|\psi_0\rangle|^2 = 1 - \frac{N}{4}\left(\frac{J-t}{J+t}\right)^2 - \left(\frac{U\sqrt{N(N-1)}}{2L\sqrt{J^2+t^2}}\right)^2 \tag{4.32}$$

where $|\psi_0\rangle$ denotes the ground state of the system at finite t/J and U/J. In case of the cattiness of the second kind, depletion is due to the off-diagonal terms of the effective Hamiltonian (4.20) as well as the part of the interaction Hamiltonian (4.19) which couples states within the subspace to states outside the subspace of the effective Hamiltonian. We obtain

$$|\langle\psi_2|\psi_0\rangle|^2 = 1 - \frac{N(N-1)\eta^2}{8(N-2)^2} - \left(\frac{U\sqrt{N(N-1)}}{2L\sqrt{J^2+t^2}}\right)^2. \tag{4.33}$$

In Fig. 4.10 we plot the energy gap versus the two cat-state measures for $t/J = 0.7$ and $t/J = 1$, respectively. The other parameters are $L = 4$, $N = 16$, $\theta = \pi/4$. We find that: (i) the larger U/J, the bigger the energy gap but the smaller are both cat-state measures. This is readily understood from Eqs. (4.7), (4.32) and (4.33): stronger on-site interactions increase the coupling $|\Delta|$ and, therefore, increase the energy gap. However they also increase coupling to other states outside of the subspace of $\hat{H}_{2\times 2}$ and the cat state is gradually depleted [81]. (ii) The smaller t/J, the bigger the energy gap but the smaller is the cattiness of the first kind at fixed U/J. This is in agreement with Eqs. (4.7) and (4.33). Physically, this means that the off-diagonal part of the single-particle Hamiltonian increases the coupling $|\Delta|$ but also dilutes the many-body correlation in the quasi-momentum basis. Consequentially, there is a trade-off between energy gap and cattiness of the first kind. We note that it might be a sizeable advantage to sacrifice part of the cat-like correlation (and therefore a weaker signal in the many-body oscillations we discuss in the next section) but make it visible on experimentally accessible time scales. Finally, we find that (iii) one can increase the energy gap by about an order of magnitude (for $N = 16$ particles) at fixed cattiness of the second kind when the ratio t/J is changed from $t/J = 1$ to $t/J = 0.7$. While we believe that this is the natural measure of comparison between uniform and non-uniform ring lattices, we admit that probing the cat state in the single-particle basis is a non-trivial task, since – as we will show below – time-of-flight imaging maps more closely on the quasi-momentum basis.

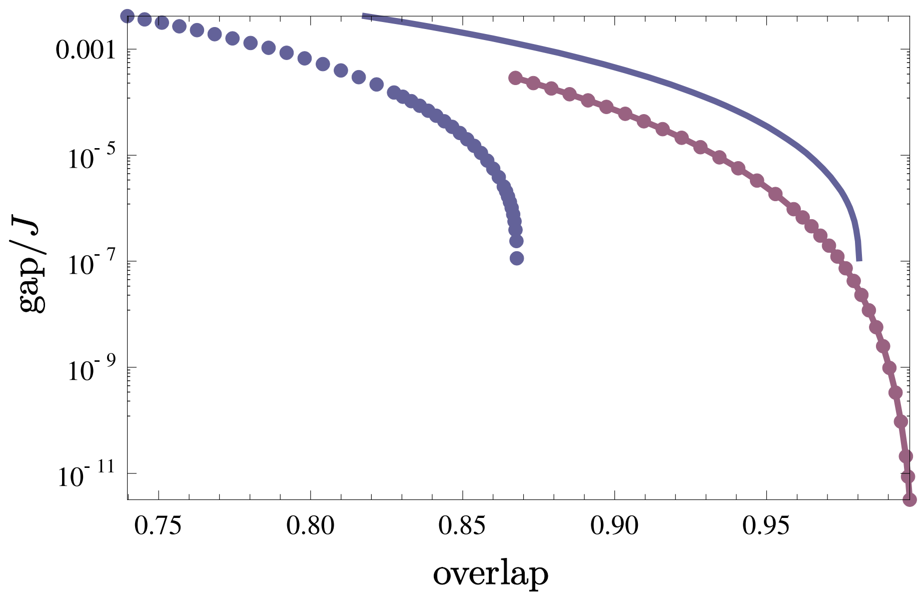

Fig. 4.10: Energy gap versus cat-state measure of the first kind (dotted points) as well as of the second kind (solid lines) for $t/J = 0.7$ (upper blue) and $t/J = 1$ (lower red). The other parameters are $L = 4$, $N = 16$ and $\theta = \pi/4$.

Increasing the coupling $|\Delta|$ with non-uniform ring lattices has important implications for the sensitivity to detunings of the rotation frequency away from the critical phase twist. In Fig. 4.11 we plot the cat-state measure of the second kind as a function of t/J and the detuning $\Delta\theta$ while $L = 4$, $N = 16$ and $U = 0.2$ are fixed. We find that the system is much less sensitive to detunings away from the critical phase twist for $t/J < 1$, i.e. the requirements on the phase control precision $\Delta\theta$ are relaxed. To understand how this comes about let us go back to the two-by-two Hamiltonian (4.23). Similar to the two-state Hamiltonian for a single particle in a double-well potential, its ground state depends on the ratio of energy difference ΔE to the coupling energy $|\Delta|$: for $|\Delta E| \gg |\Delta|$ the system is in one of the states $|N, 0\rangle$ (in the double-well analogy on the left-hand side) or $|0, N\rangle$ (on the right hand side) whereas it is in their superposition state in the limit where the coupling energy dominates $|\Delta E| \ll |\Delta|$. As the coupling $|\Delta|$ in Eq. (4.7) decreases exponentially with increasing number of particles N, more control over the rotation frequency is needed to tune systems with more particles into resonance, i.e. to make the energy difference $|\Delta E|$

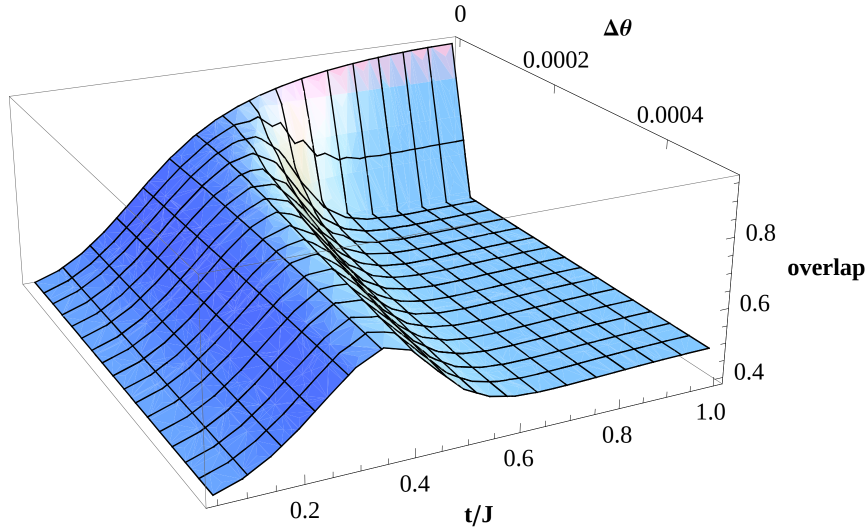

Fig. 4.11: Cat-state measure of the second kind as a function of t/J and the detuning $\Delta\theta$ while $L = 4$, $N = 16$ and $U = 0.2$ are fixed.

between the states $|N, 0\rangle$ and $|0, N\rangle$ smaller than their coupling $|\Delta|$. This was identified as one of the barriers for creating large cat-like states [81]. As the gap increases when t/J is decreased (see Eq. (4.7)), we conclude that using non-uniform ring lattices $t \neq J$ can improve the situation on this issue.

4.5 Dynamical detection of cat-like correlations

In this section we propose to induce many-body oscillations by suddenly changing the applied phase twist θ in order to detect the coherent superposition of two quasi-momentum states $|N, 0\rangle = (\hat{b}_0^\dagger)^N|\text{vac}\rangle/\sqrt{N!}$ and $|0, N\rangle = (\hat{b}_{L/4}^\dagger)^N|\text{vac}\rangle/\sqrt{N!}$ at the anti-crossing of the many-body spectrum.

If we assume the system is initially in the ground state of the full Hamiltonian at $\theta = 0$ which will predominantly be the state $|N, 0\rangle$, i.e. $|\psi(t = 0)\rangle \approx |N, 0\rangle$. Then, the phase twist is changed to $\theta = \pi/4$, where the eigenstates are approximately $|\pm\rangle \approx (|N, 0\rangle \pm |0, N\rangle)/\sqrt{2}$.

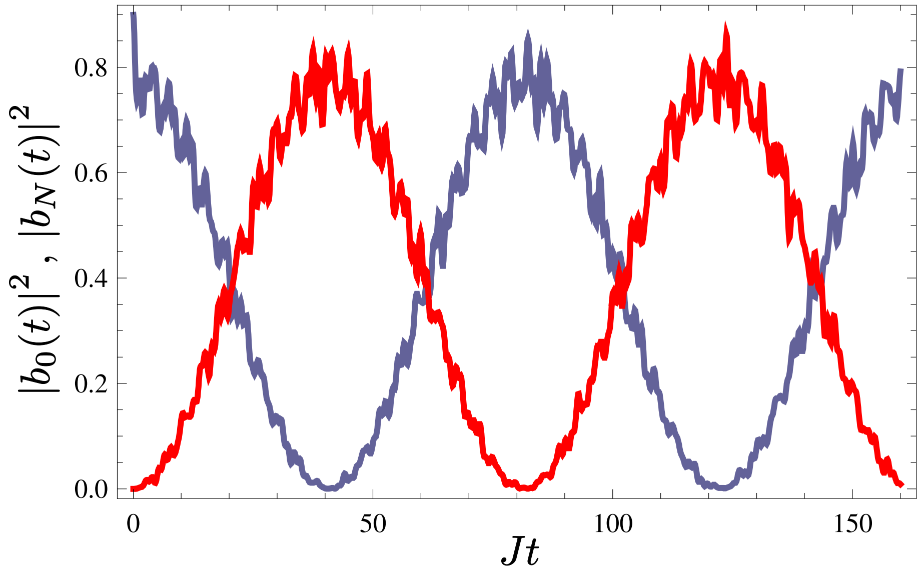

Fig. 4.12: Many-body dynamics $|b_0(t)|^2$ and $|b_N(t)|^2$ for $L = 4$ and $N = 8$ following a sudden change in phase twist from $\theta = 0$ to $\theta = \pi/4$ at $U/J = 1$ and $t/J = 0.7$.

The time evolution of the probability to be in the state $|N, 0\rangle$ and $|0, N\rangle$ is

$$|b_0(t)|^2 = |\langle N, 0|\psi(t)\rangle|^2 \approx \frac{1 + \cos \nu t}{2} \tag{4.34}$$

and $|b_N(t)|^2 \approx 1 - |b_0(t)|^2$ where $\hbar\nu = E_+ - E_-$ denotes the energy gap and where the approximate signs indicate that we neglect the depletion due to the non-diagonal part of the single-particle Hamiltonian (4.13) and the on-site interaction Hamiltonian (4.19).

In Fig. 4.12 we show the many-body dynamics, i.e. $|b_0(t)|^2$ and $|b_N(t)|^2$ for $L = 4$ and $N = 8$ following a sudden change in phase twist from $\theta = 0$ to $\theta = \pi/4$ at time $t = 0$ with $U/J = 1$ and $t/J = 0.7$. We see that the many-body oscillations following this sudden change occur at the frequency of the gap $\hbar\nu$. These oscillations are modulated by an oscillation with frequency $U(N-1)/L$ which is the energy difference between the nearly-degenerate ground states and the next lowest-lying intermediate states $|2, N-2\rangle$ and $|N-2, 2\rangle$. The amplitude of the oscillations is smaller than one, i.e. $|b_0(t)|^2 + |b_N(t)|^2 < 1$, due to the depletion of the quasi-momentum cat state $|\langle\psi_1|\psi_0\rangle|^2$ (see Eq. (4.32)).

4.6 Signatures of quasi-momentum states in time-of-flight images

In this section we study the spatial density profile of an atomic cloud when it is allowed to freely expand after turning off the ring lattice potential. Our analysis shows that states with different quasi-momentum states exhibit a distinctive time-of-flight pattern and that therefore the latter can be used as an experimental probe for detecting the many-body oscillations between the states $|0, N\rangle$ and $|N, 0\rangle$ discussed in the previous section.

For this discussion we will consider the expansion of the wave function of a single atom initially confined in a 1D lattice ring geometry. For simplicity we approximate the axial, radial and angular Wannier functions as Gaussians with width σ_z, σ_r and $\rho_0\sigma_\Theta$, respectively, and localized in a ring of radius ρ_0 at $z = 0$

$$\psi(\mathbf{r}, t = 0) = Ae^{-\frac{z^2}{2\sigma_z^2}} e^{-\frac{(r-\rho_0)^2}{2\sigma_r^2}} \sum_{n=1}^{L} c_n e^{-\frac{(\Theta-2\pi n/L)^2}{2\sigma_\Theta^2}} \tag{4.35}$$

where A is a normalization constant. If at time $t = 0$ the atom is in an eigenstate of the uniform ring with quasi-momentum $\hbar 2\pi q_0/La$ then $c_n = \frac{1}{\sqrt{L}} e^{i(2\pi n q_0/L)}$.

At sufficiently large times $t \gg M\rho_0/\hbar$ one can take the far-field limit and approximate the density of the expanded cloud as being proportional to the momentum distribution of the initial state, i.e.

$$|\psi(\mathbf{r}, t \to \infty)|^2 \approx \left(\frac{M}{ht}\right)^3 |\phi(\mathbf{Q}(\mathbf{r}))|^2 \tag{4.36}$$

where $\mathbf{Q}(\mathbf{r}) = M\mathbf{r}/\hbar t$ and $|\phi(\mathbf{k})|^2$ is the momentum distribution of the initial state. After integrating along the z axis, one can write a simple analytical expression of the transverse spatial density distribution in the limit of strongly confined Wannier orbitals (i.e. $\sigma_r \to 0$ and $\sigma_\Theta \to 0$)

$$|\psi(\rho, \Theta, t \to \infty)|^2 = \int |\psi(\mathbf{r}, t \to \infty)|^2 dz \propto \left(\frac{M\rho_0}{Lht}\right)^2 \left|\sum_n e^{(i\frac{2\pi n q_0}{L} - iQ(\rho)\rho_0 \cos(\frac{2\pi n q_0}{L} - \Theta))}\right|^2. \tag{4.37}$$

In the limit of a large number of lattice sites L, the sum in Eq. (4.37) can be approximated by an integral and the time-of-flight profile reduces to

$$|\psi(\rho, \Theta, t \to \infty)|^2 \to \left(\frac{M\rho_0}{ht}\right)^2 \left|J_{q_0}[Q(\rho)\rho_0]\right|^2 \tag{4.38}$$

where $J_{q_0}(x)$ are Bessel functions of the first kind. This case corresponds to the rotationally symmetric case discussed in Ref. [90] where the position of the zeros and maxima of the Bessel functions provide a full characterization of the density profile. A state initially with zero quasi-momentum for example will exhibit an interference peak at the origin while a state with non-zero quasi-momentum will exhibit a central hole. As the position of the first maximum of $J_{q_0}[Q(\rho)\rho_0]$ is an increasing function of q_0, the larger the initial quasi-momentum the wider the central hole. For a finite number of lattice sites the sum does not correspond exactly to a Bessel function and the momentum distribution does not become fully radially symmetric. However, there is still a unique correspondence between the position of the peaks in the absorption image and the initial quasi-momentum distribution (see also Ref. [91]). Consequently, the latter provides a means to experimentally determine the quasi-momentum of the wave function before the release.

In Fig. 4.13 we show the numerically calculated time-of-flight images of different ring lattice geometries for two states with initial quasi-momentum $q_0 = 0$ and $L/4$, respectively. These states correspond to the two types of initial distributions that one has to experimentally distinguish in order to probe the many-body oscillations we have discussed in the previous section. The figure shows the distinctive interference pattern of each of the two initial states and the asymptotic approach to radial symmetry as the number of lattice sites L is increased.

4.7 Conclusion

We investigated the effects of rotation on the ground state properties of bosonic atoms in a rotating ring lattice. We found that at commensurate filling there exists a critical rotation frequency, at which the ground state of the weakly-interacting gas is fragmented into a macroscopic superposition of different quasi-momentum states. Introducing a superlattice the energy gap between the cat-like ground and first excited states scales more favorably with the number of particles and the constraints on phase twist control and commensurate filling are relaxed. This makes the cat less sensitive to imperfections in the system, but sacrifices overlap with a macroscopic superposition of different flow (cattiness of the first kind). Finally, we have proposed to probe the cat-like correlations via the many-body oscillations induced by a sudden change in the rotation frequency. Since the exponential scaling of the energy gap with the number of particles remains, we suspect that cat state production in ultracold atomic gases is limited to modest number of atoms.

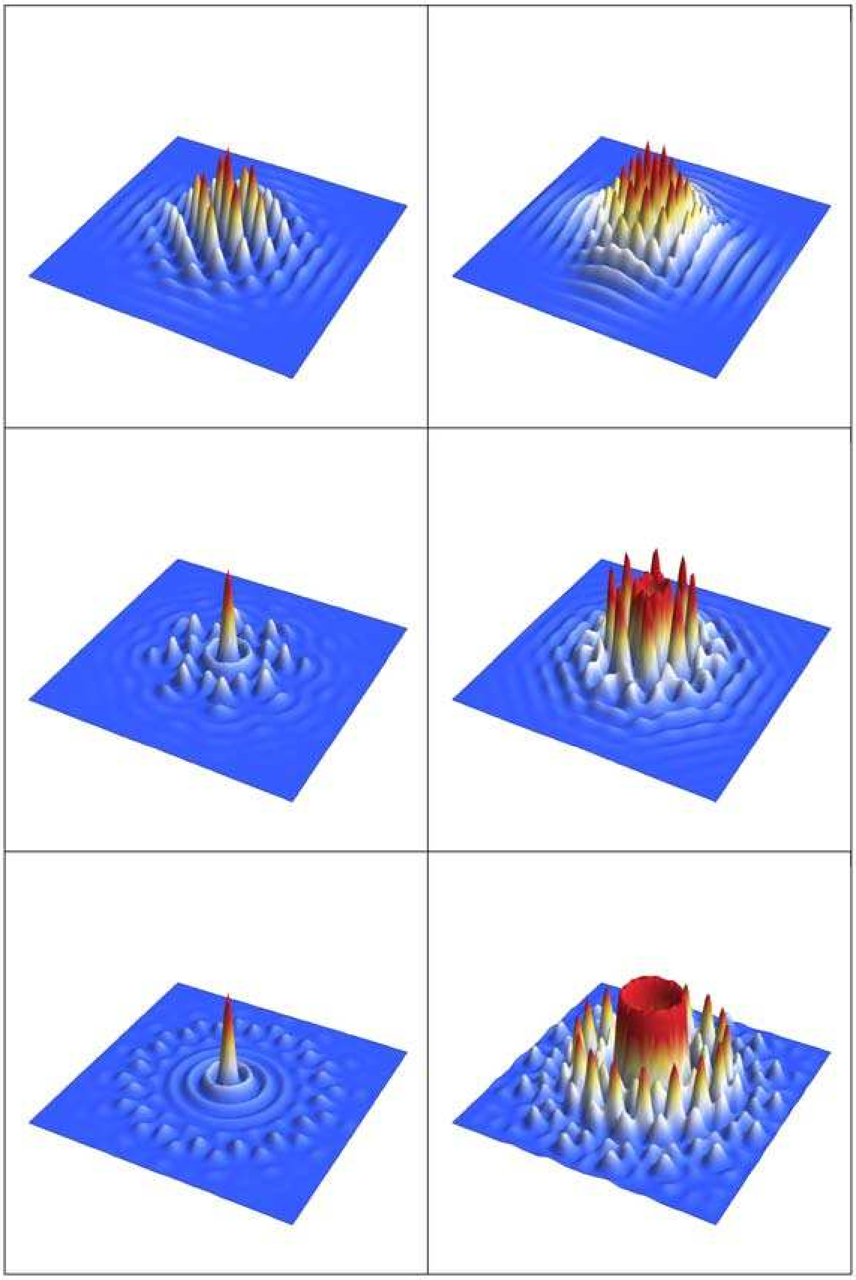

Fig. 4.13: Transverse time-of-flight images of an initial state with quasi-momentum $q_0 = 0$ (left) and $q_0 = L/4$ (right) for different ring lattice geometries (top $L = 4$, center $L = 8$ and bottom $L = 16$).

Chapter 5

Macroscopic superposition states of flux qubit devices

In this chapter, we study macroscopic superposition states produced in flux qubit devices. We first derive the effective action of these "artificial" quantum devices in the limit of low temperatures and small frequencies. We find that the magnetic flux threading the superconducting ring is the only essential variable, since fluctuations in all other macroscopic variables are strongly suppressed due to the energy gap in the charged superconductor. We show that macroscopic superposition states can be achieved in the macroscopic quantum coherence regime, where the tunneling barrier of the adiabatic potential is small even for a large number of Cooper pairs. Finally, we compare the two different mechanisms leading to macroscopic superposition states: correlated tunneling and tunneling in adiabatic potentials.

5.1 Introduction

In the previous chapter, we showed that ultracold bosons in rotating ring lattices form macroscopic superpositions of different quasi-momentum states. Since the coupling between the two configurations is a highly off-resonant process, the many-body tunneling rate decreases exponentially with increasing number of particles. Consequently, the achievable size of macroscopic superposition states with these systems will remain very limited on accessible experimental timescales.

Experiments with superconducting quantum interference devices (SQUID), so-called flux qubit devices, however, have convincingly demonstrated superposition states of macroscopically distinct flow, both spectroscopically [92] and by observing real-time oscillations [93]. How is this possible? In what respect are these macroscopic superposition states different from each other?

5.2 Effective action of flux qubit devices

A superconducting quantum interference device (SQUID) is a superconducting ring with a weak link at which superconductivity has been deliberately destroyed, i.e. it is a superconducting tunnel junction whose two electrodes are joined in a loop. The effective action of a superconducting tunnel junction was first derived in Ref. [94]. The authors start from a microscopic theory, i.e. the BCS theory of superconductivity, a tunneling Hamiltonian describing the junction as well as the charging energy due to the Coulomb interaction across the barrier. Using a path-integral description, they perform a Hubbard-Stratonovich transformation to eliminate the quartic interaction terms of the BCS Hamiltonian. In this way, they make explicit the essential macroscopic variables, i.e. the superconducting order parameter $\Delta(\mathbf{x})$, the supercurrent density $\mathbf{j}_s(x)$, the phase difference ϕ and the voltage drop V across the junction. Analyzing the fluctuations around the classical mean-field configuration, they find that for temperatures well below the critical temperature of the superconductor and for frequencies smaller than the plasma frequency the following fluctuations are suppressed:

- spatial fluctuations in the modulus of the order parameters $|\Delta(\mathbf{x})|$,
- deviations from the Meissner law, $\nabla^2\mathbf{B} - \frac{1}{\lambda_L^2}\mathbf{B} = 0$ with the magnetic field $\mathbf{B}$ and the London penetration depth λ_L, and
- deviations from the classical Josephson relations, $V = \frac{\hbar}{2e}\frac{\partial\phi}{\partial t}$ and $I = I_c \sin\phi$ with the critical current I_c of the junction.

In imaginary-time path-integral representation, the partition function of a SQUID then reads, up to irrelevant factors, $Z \propto \int D\Phi\, e^{-S[\Phi]/\hbar}$. The effective action $S[\Phi]$ [94] is

$$S[\Phi] = \int_0^{\hbar\beta} d\tau \left(\frac{C}{2}\left(\frac{\partial\Phi}{\partial\tau}\right)^2 + U(\Phi) \right) \tag{5.1}$$

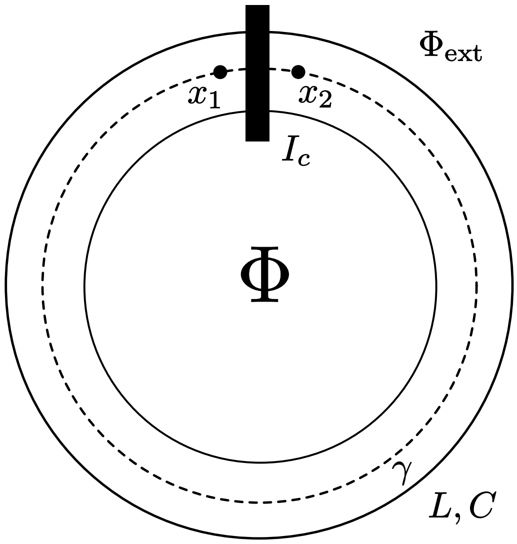

Fig. 5.1: Superconducting ring with conductance C and inductance L. The tunneling barrier between the points x_1 and x_2 (black rectangle) has a critical current I_c. The ring is threaded by a magnetic flux Φ, while the external flux is $\Phi_{\rm ext}$. The dotted line is the integration path γ inside the superconductor.

with the potential

$$U(\Phi) = \frac{1}{2L}\left(\Phi - \Phi_{\rm ext}\right)^2 - \frac{\hbar I_c}{2e}\cos\left(2\pi\frac{\Phi}{\Phi_0}\right), \tag{5.2}$$

where I_c is the critical current of the junction, $\Phi_0 = h/2e$ the magnetic flux quantum, L the geometrical inductance of the loop, and $\Phi_{\rm ext}$ the external magnetic flux. The first term in Eq. (5.1) is the electric energy $\frac{C}{2}V^2$ combined with the classical Josephson relation $V = \frac{\hbar}{2e}\frac{\partial\phi}{\partial t}$. The first term of Eq. (5.2) is the magnetic energy due to the current flowing along the ring and the second term of Eq. (5.2) is the classical Josephson energy for a tunnel junction $E = \int VI\,dt = E_J\int\sin\phi\,d\phi = -E_J\cos\phi$ with $E_J = \hbar I_c/2e$. We see that the flux qubit is characterized by three parameters: the capacitance C and the inductance of the ring L as well as the critical current of the junction I_c.

Following Ref. [95], one can arrive at a description equivalent to the effective action (5.1) by quantizing the classical equation of motion for the magnetic flux Φ. First, we note that a Josephson junction can be approximated by a capacitor with capacitance C connected in parallel with a non-linear circuit element characterized by the Josephson relation $I_J = I_c \sin\phi$, where I_c is the critical current and ϕ is the phase of the junction. Second, we write down Kirchhoff's law for the circuit, $I = \dot{Q} + I_J$, where I is the current in the loop and Q is the charge on the capacitor. Third, Faraday's law of induction tells us that the magnetic flux Φ through the ring is related to the voltage V over the junction by $\dot{\Phi} = -V = -Q/C$, where the magnetic flux Φ consists of the external magnetic flux Φ_{ext} as well as the flux due to the inductance L of the ring, $\Phi = \Phi_{\text{ext}} + LI$.

Within the phenomenological Ginzburg-Landau theory, we now relate the phase of the junction ϕ to the magnetic flux through the ring Φ. We describe the superconductor by a complex order parameter $\Delta(\mathbf{x}) = \sqrt{\rho(\mathbf{x})}e^{i\varphi(\mathbf{x})}$, whose modulus squared is the density of the Cooper pairs $\rho(\mathbf{x})$. If spatial fluctuations of the order parameter are heavily suppressed, we can approximate the order parameter to be $\Delta(\mathbf{x}) = \sqrt{\rho_0}e^{i\varphi(\mathbf{x})}$ with a constant density ρ_0. According to the Meissner effect, a superconductor is a perfect diamagnet, i.e. an external magnetic field is completely expelled from the interior of the superconductor, so that there are no supercurrents below the London penetration depth λ_L, $0 = \mathbf{j}_s = -\frac{2e}{\hbar}\rho_s\left(\nabla\varphi + \frac{2e}{\hbar}\mathbf{A}\right)$, thus $\mathbf{A}/\Phi_0 = -\nabla\varphi/2\pi$ with the magnetic flux quantum $\Phi_0 = h/2e$. In Fig. 5.1 we show the geometry of a SQUID, where we marked two points x_1 and x_2 close to the tunnel barrier and indicated an integration path γ connecting these two points inside the ring below the penetration depth λ_L. The line integral over the vector potential $\mathbf{A}$ is related to the magnetic flux Φ by

$$\Phi = \int_{S(\gamma)} \mathbf{B}\cdot d\mathbf{S} = \int_\gamma \mathbf{A}\cdot d\mathbf{x} \approx -\frac{\Phi_0}{2\pi}\int_{x_1}^{x_2} \nabla\varphi\cdot d\mathbf{x} = -\frac{\Phi_0}{2\pi}\left(\varphi(x_2) - \varphi(x_1)\right) = -\frac{\Phi_0}{2\pi}\phi. \quad (5.3)$$

Here, $S(\gamma)$ is the area of the ring and γ is the integration path inside the superconductor. The approximate sign comes from neglecting the region of the small barrier. We find that the magnetic flux Φ is proportional to the phase around the loop $\varphi(x_2) - \varphi(x_1)$ which is also the phase across the junction ϕ. Please note that two values ϕ and $\phi + 2\pi$ refer to a different physical state of the system.

We can now write down the equation of motion for the magnetic flux

$$C\ddot{\Phi} + \frac{\Phi - \Phi_{\mathrm{ext}}}{L} - I_c \sin\left(\frac{2\pi\Phi}{\Phi_0}\right) = 0. \tag{5.4}$$

This equation can be derived via the principle of minimal action from the Lagrangian $L_\Phi = \frac{1}{2}C\dot{\Phi}^2 - U(\Phi)$ where the potential $U(\Phi)$ is given by Eq. (5.2). The momentum Π_Φ conjugate to the magnetic flux Φ is the electric charge $\Pi_\Phi = \frac{\partial L}{\partial \dot{\Phi}} = C\dot{\Phi} = -CV = -Q$, so that we obtain the corresponding Hamiltonian $H_\Phi = \Pi_\Phi\dot{\Phi} - L_\Phi = \frac{\Pi_\Phi^2}{2C} + U(\Phi)$, which is the sum of electric $\frac{Q^2}{2C}$, magnetic $\frac{(\Phi-\Phi_{\mathrm{ext}})^2}{2L}$ and Josephson energy $-\frac{\hbar I_c}{2e}\cos\left(2\pi\frac{\Phi}{\Phi_0}\right)$. From the microscopic derivation [94], we are justified to write down the corresponding Schrödinger equation

$$i\hbar\frac{d}{dt}|\psi(t)\rangle = \hat{H}_\Phi\,|\psi(t)\rangle \tag{5.5}$$

where the magnetic flux $\hat{\Phi}$ and electric charge $\hat{\Pi}_\Phi$ satisfy the canonical commutation relation $\left[\hat{\Phi}, \hat{\Pi}_\Phi\right] = i\hbar$.

5.3 Flux-quantization and macroscopic quantum coherence regime

Following Ref. [95], we define the dimensionless quantities $\theta = 2\pi\Phi/\Phi_0$ and $\theta_{\mathrm{ext}} = 2\pi\Phi_{\mathrm{ext}}/\Phi_0$ and rewrite the flux potential (5.2) in the form

$$U(\Phi) = \frac{I_c\Phi_0}{2\pi}\tilde{U}(\theta) \text{ with } \tilde{U}(\theta) = \frac{\gamma}{2}(\theta - \theta_{\mathrm{ext}})^2 - \cos\theta \text{ and } \gamma = \frac{\Phi_0}{2\pi L I_c}. \tag{5.6}$$

We note that, using a superconducting ring with three or four Josephson junctions, the critical current I_c of the circuit and thus the parameter γ can be controlled by means of an additional external magnetic flux [96].

In Fig. 5.2 we plot the potential energy $\tilde{U}(\Phi)$ as a function of the magnetic flux Φ in two different regimes:

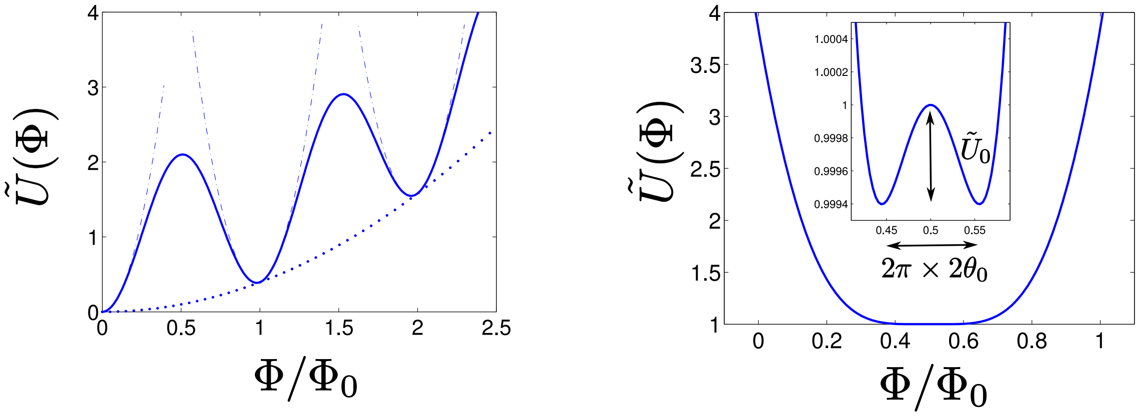

Fig. 5.2: Potential energy $\tilde{U}(\Phi)$ (5.6) as a function of the magnetic flux Φ. On the left, the flux-quantization regime with $\gamma = 0.02$ and $\Phi_{\rm ext} = 0$. We additionally show the magnetic energy contribution (dotted) and the harmonic approximation around integer magnetic flux quanta in the ring (dash-dotted). On the right, the macroscopic quantum coherence regime for $\gamma = 0.98$ and $\Phi_{\rm ext} = \Phi_0/2$.

- In the *flux-quantization regime* for $\gamma \approx 0$, we obtain a series of energy minima at which the flux is an integer multiple of the flux quantum Φ_0. Thermal activation and quantum tunneling allow transitions between neighboring metastable minima. If the energy barriers are much larger than the zero-point motion due to the charging energy $\frac{Q^2}{2C}$, the tunneling rates are small and persistent currents have an extremely long life time.

- In the *macroscopic quantum coherence regime* for $\gamma \lesssim 1$ and $\Phi_{\rm ext}/\Phi_0 = 1/2$, we obtain a symmetric double-well potential whose minima are close to $\Phi/\Phi_0 = 1/2$. Expanding the potential to third order around $\theta = \pi$, the minima are located at $\theta = \pi \pm \theta_0 = \pi \pm \sqrt{6(1-\gamma)}$ and the potential barrier height is $\tilde{U}_0 = \frac{3}{2}(1-\gamma)^2$. We see that for $\gamma \to 1$ the energy barrier separating the two minima becomes small $\tilde{U}_0 \to 0$ and the minima move closer together $\theta_0 \to 0$. In this limit, the zero-point motion due to the charging energy $\frac{Q^2}{2C}$ (where the effective mass is the capacitance C) leads to tunneling across the barrier and couples two macroscopic states with slightly different flux $\pi \pm \theta_0 \approx \pi \pm 10^{-4}$ [92]. That means, although the number of electrons which contribute to the current Φ_0/L corresponding to one flux quantum Φ_0 is *large*, the height $\tilde{U}_0$ of the potential barrier controlling the tunneling process and the difference in flux (which potentially leads to decoherence) can be *small*.

5.4 Two different mechanisms leading to macroscopic superposition states

In this section, we first show that the macroscopic superposition states in flux qubit devices can be understood within the framework of the Born-Oppenheimer approximation [97]. We then point out that the macroscopic superposition states formed during correlated tunneling processes in double-well potentials and those occurring in rotating ring lattices are two sides of the same coin. Finally, we compare these two different mechanisms leading to macroscopic superposition states, correlated tunneling and tunneling in adiabatic potentials, with each other.

Let us start by reviewing the Born-Oppenheimer approximation for the electronic and nuclear degrees of freedom of a molecule. The Hamiltonian for electrons and nuclei is

$$\hat{H} = \hat{T}_N + \hat{H}_e \text{ with } \hat{H}_e = \hat{T}_e + \hat{V}_{ee} + \hat{V}_{eN} + \hat{V}_{NN} \tag{5.7}$$

$$\text{where } \hat{T}_N = \sum_n \frac{\hat{P}_n^2}{2M_n} \text{ and } \hat{T}_e = \sum_i \frac{\hat{p}_i^2}{2m}. \tag{5.8}$$

$\hat{T}_e$ is the kinetic energy of the electrons with mass m, $\hat{T}_N$ the kinetic energy of the nuclei with masses M_n, $\hat{V}_{ee}$ the interaction of the electrons, $\hat{V}_{eN}$ the interaction between electrons and nuclei, and $\hat{V}_{NN}$ the interaction of the nuclei. The momentum and position operators of the electrons are $\hat{p}_i$ and $\hat{x}_i$ and the ones of the nuclei are $\hat{P}_n$ and $\hat{X}_n$.

Suppose we had solved the Schrödinger equation of the electronic degrees of freedom $x = \{x_i\}$ for fixed nuclear coordinates $X = \{X_i\}$

$$\hat{H}_e\, \varphi_n(x; X) = \varepsilon_n(X)\, \varphi_n(x; X). \tag{5.9}$$

In this expression, the notation $\varphi_n(x; X)$ and $\varepsilon_n(X)$ reminds us that the electronic wave functions and their energy parametrically depend on the positions of the nuclei X. The total wave function $\Psi(x, X)$ can then be expanded as follows

$$\Psi(x, X) = \sum_n \varphi_n(x; X)\, \Phi_n(X). \tag{5.10}$$

In this basis the full Schrödinger equation $\hat{H}\Psi = E\Psi$ is turned into a set of coupled eigenvalue equations by multiplication with $\varphi_m^*(x; X)$ and integration over x

$$\sum_n \Big(\langle \varphi_m |\, \hat{T}_N \,| \varphi_n \rangle + \varepsilon_n(X)\, \delta_{mn} \Big)\, \Phi_n(X) = E\, \Phi_m(X). \tag{5.11}$$

The nuclear kinetic energy operator $\hat{T}_N$ couples states of different adiabatic potentials $\varepsilon_n(X)$. If these non-adiabatic matrix elements $\langle \varphi_m | \hat{T}_N | \varphi_n \rangle$ are small compared to the energy difference between the adiabatic potentials $\varepsilon_m(X) - \varepsilon_n(X)$, the set of equations (5.11) decouples and the effective Schrödinger equation becomes

$$\Big(\langle \varphi_n |\, \hat{T}_N \,| \varphi_n \rangle + \varepsilon_n(X) \Big)\, \Phi_n(X) = E \Phi_n(X). \tag{5.12}$$

In contrast to the gapless single-particle spectrum of a neutral superfluid, the energy separation in case of the flux qubit device is given by either the plasma energy for density excitations or the superconducting energy gap for single-particle excitations. That is why, the non-adiabatic matrix elements are typically much smaller than the energy separation, and we can interpret the Schrödinger equation for the magnetic flux Φ (5.5) as an effective Schrödinger equation in the sense of Eq. (5.12), where the magnetic flux Φ takes the role of the nuclear degrees of freedom X and $U(\Phi)$ is the adiabatic potential. Thus, we see that macroscopic superposition states of flux qubit devices can be described within a similar framework as those which occur in tunneling processes between different configurations of ammonium NH_4 or ethane C_2H_6 as well as matter-wave diffraction experiments with Buckminster fullerene molecules C_{60} [98], where the single-particle motion is suppressed due to the binding energy instead of the superconducting energy gap.

On the other hand, the superposition states which occur during the correlated tunneling processes discussed in Chapter 3 are closely related to those in rotating ring lattices studied in Chapter 4. Both of them are driven by perturbative coupling through many off-resonant intermediate states (see Figs. 3.3 and 4.2). In the former case, the superposition involves the spatially localized modes centered at the left and right side of the double-well potential, whereas they are formed out of delocalized quasi-momentum states in case of the rotating ring lattice. While correlated motion in real space occurs in the interaction-dominated regime $U \gg J$, superpositions of different flow appear in the weakly-interacting regime $J \gg U$. We see that there is a one-to-one correspondence between these two types of macroscopic superposition states.

Let us now compare the two different mechanisms leading to macroscopic superposition states: correlated tunneling in double-well potentials and tunneling in adiabatic potentials. In order to have correlated motion in the former case, the detuning between the intermediate states, proportional to the on-site interaction energy U, must be much larger than the coupling between the states, proportional to the tunneling energy J, i.e. correlated motion takes place in the interaction-dominated regime: $J \ll U$. The coupling Δ_N (3.5) between the macroscopic states $|0, N\rangle$ and $|N, 0\rangle$ decreases exponentially in the *small* parameter J/U: $\Delta_N \propto (J/U)^N$. In the case of tunneling in adiabatic potentials, the tunneling probability also decreases exponentially with increasing number of particles, since the zero-point motion of the center-of-mass coordinate decreases with increasing total mass. However, since the single-particle motion is suppressed by the molecular binding energy or the superconducting energy gap, correlated motion of many particles is still possible, as long as there are two low-lying states of the adiabatic potential which are separated only by a *small* energy barrier. That is why macroscopic quantum coherence phenomena with a large number of particles can be observed in flux qubit devices, but not with the systems of neutral atoms we discussed.

5.5 Conclusion

We showed that macroscopic superposition states can be achieved with flux qubit devices, because the tunneling barrier of the adiabatic potential in the macroscopic quantum coherence regime is small even for a large number of Cooper pairs. In this case, correlated motion of all the particles occurs, since single-particle and density excitations are suppressed by the energy gap and the plasma frequency in the charged superconductor.

Chapter 6

Creation of resilient entangled states and a resource for measurement-based quantum computation with optical superlattices

In this chapter, we investigate how to create entangled states of ultracold atoms trapped in optical lattices by dynamically manipulating the shape of the lattice potential. We consider an additional potential (the superlattice) that allows both the splitting of each site into a double-well potential, and the control of the height of potential barrier between sites. We use superlattice manipulations to perform entangling operations between neighboring qubits encoded on the Zeeman levels of the atoms without having to perform transfers between the different vibrational states of the atoms. We show how to use superlattices to engineer many-body entangled states resilient to collective dephasing noise. Also, we present a method to realize a 2D resource for measurement-based quantum computing via Bell-pair measurements. We analyze measurement networks that allow the execution of quantum algorithms while maintaining the resilience properties of the system throughout the computation.

6.1 Introduction

The experimental realization of bosonic spinor condensates in optical lattices has opened up the possibility to exploit the spin degree of freedom for a wide range of applications [99, 100]. Further experiments have proved that these systems are promising candidates for quantum information processing purposes (see [66] and references therein) and the study of quantum magnetism [65]. Recently, the time-resolved observation and control of superexchange interactions in optical superlattices have been reported [67]. [1]

[1] Apart from Section 6.7, this chapter was published as Ref. [30]. My main contribution was the analytical description of the creation of a Bell state on every lattice site and of the implementation of an entangling gate, presented in Section 6.3 and Section 6.4, respectively.

In the literature there are several proposals using spinor condensates in optical lattices, e.g. to create macroscopic entangled states [101, 102] or to explore magnetic quantum phases [103]. In this chapter, we consider the possibility of using optical superlattices to manipulate the spin degrees of freedom of the atoms and engineer many-body entangled states among others for quantum information purposes.

Superlattice setups allow the transformation of every site of the optical lattice into a double-well potential, and also the control of the potential barrier between sites [104, 105, 65]. Atoms with overlapping motional wave functions interact via cold collisions that coherently modify their spin, while conserving the total magnetization of the system [106, 56]. Thus, by splitting each lattice site into a double-well potential, two atoms occupying the same site become separated by a potential barrier, and the interactions between them are switched off. Similarly, interactions between atoms can be switched on again for a certain time by lowering the potential barrier between the two sides of the double-well. Therefore, superlattice manipulations offer the possibility to apply operations between large numbers of atoms in parallel. In this work, we propose to exploit this parallelism to engineer highly-entangled many-body states.

The process of splitting a Bose-Einstein condensate using double-well potentials has already been studied in the context of mean-field theory [107, 108, 109]. In the first part of this chapter, we will derive a two-mode effective Hamiltonian that allows an accurate description of the system as the superlattice is progressively turned on. Our approach differs from previous treatments of double-well potentials (see e.g. Ref. [107]) or the work in Ref. [103], as the effective model we use is valid even for low barrier heights. We will use this effective Hamiltonian to analyze the process of splitting every site into a double-well potential starting with two atoms per site. We will show that this process creates a Bell state encoded on the Zeeman levels of the atoms in every site, each atom occupying one side of the double-well. Since these states are resilient to collective dephasing noise, we will use a lattice with a Bell pair in every site as a starting point to engineer many-body entangled states.

In the second part, we present a new method for implementing an entangling $\sqrt{\text{SWAP}}$ gate that does not require to transfer the atoms between different vibrational states. We will show that the application of this entangling gate between (or inside) Bell pairs allows the creation of many-body entangled states resilient to collective dephasing noise. [2]

In the final part, we propose a new method involving superlattice manipulations to realize a 2D resource state for measurement-based quantum computation (MBQC) formally similar to a Bell-encoded cluster state. Since the realization of logical gates between non-neighboring qubits is practically very difficult in optical lattices [113], the one-way model for quantum computation is particularly relevant for these systems [61, 62, 114]. The resource state we propose is resilient to collective dephasing noise, which makes it less prone to decoherence than the usual cluster states. Its utilization as a resource for MBQC requires adjustments of the measurement patterns used for cluster states, which we describe in the last section. We note that the realization of Bell-encoded cluster states as a resource for MBQC was proposed in Ref. [115] using lattice manipulations in three dimensions. The distinguishing feature of our proposal is that the resource state is created via 2D superlattice operations which have been demonstrated in the lab already.

This chapter is organized as follows. In Sec. 6.2 we derive an effective model for describing the dynamics of atoms within one site in the presence of a superlattice potential. In Sec. 6.3, starting with a lattice where every site contains two atoms of opposite spin, we show how to create a Bell pair in each site by splitting it using a superlattice potential. In Sec. 6.4, we present how to perform a gate between two neighboring qubits by manipulating the superlattice potential, and in Sec. 6.5 and Sec. 6.6 we show how to

[2] After our paper [30] had been published, we became aware of Ref. [110]. Refs. [111, 112] also considered the dynamics of spinor bosonic atoms in an array of double-well potentials.

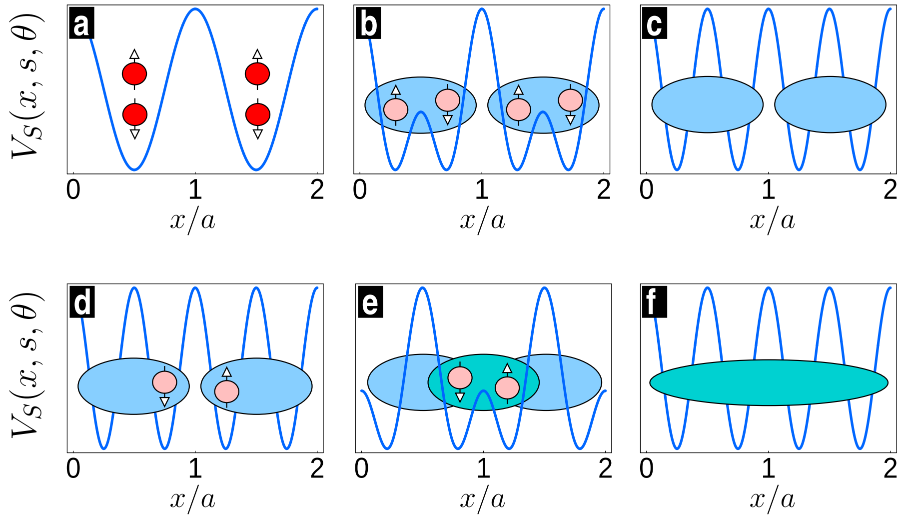

Fig. 6.1: (a) The system is initialized with two atoms per site in the state $w_a(\mathbf{r})^2 \otimes \mathcal{S}(|f_1 = 1, m_1 = +1; f_2 = 1, m_2 = -1\rangle)$ and the lattice parameters are $s = 0$ and $\theta = 0$. (b) The lattice potential is smoothly altered by increasing the lattice parameter s while $\theta = 0$. (c) At the end of the first step, the lattice parameter is $s = 1$. Each lattice site then contains a Bell pair. (d-f) After setting the angle to $\theta = \pi/2$, the other set of barriers are lowered by decreasing the lattice parameter s from $s = 1$ (d) to $0 < s < 1$ (e) and back to $s = 1$ (f).

use this gate to create many-body entangled states. In Sec. 6.7 we review the basics of MBQC, and finally, in Sec. 6.8, we propose a method for creating a resource for MBQC via Bell-pair measurements and provide measurement networks to implement a universal set of gates. We conclude in Sec. 6.9.

6.2 Model

We consider a gas of ultracold alkali atoms loaded into a deep optical lattice. The atoms are assumed to be bosons initialized in the $f = 1$ hyperfine manifold [100]. The lattice potential is given by $V_{OL}(\mathbf{r}, s, \theta) = V_T[\sin^2(\pi z/a) + \sin^2(\pi y/a) + V_S(x, s, \theta)]$ where V_T is the depth of the potential and

$$V_S(x, s, \theta) = (1 - s)\sin^2\left(\frac{\pi x}{a} + \theta\right) + s \sin^2\left(\frac{2\pi x}{a}\right). \qquad (6.1)$$

The depth of the potential will be given in units of the recoil energy $E_R = \hbar^2\pi^2/(2Ma^2)$ where M is the mass of the atoms. The parameter $s \in [0, 1]$ is determined by the relative intensities of the two pairs of lasers. The constant a corresponds to the size of a unit cell when $s = 0$ (see Fig. 6.1a). We will refer to unit cells when $s = 0$ as to *lattice sites*. Changing the value of s from 0 to 1 transforms each site in a double-well potential. We will refer to each side of this double-well potential when $s = 1$ as to a *subsite*. The angle θ allows for the manipulation of the potential barrier *inside* each site ($\theta = 0$) or *between* sites ($\theta = \pi/2$). A few lattice profiles corresponding to different parameters s and θ are shown in Fig. 6.1. In the following, we will refer to the lattice profiles corresponding to the values of $s \approx 0$ and $s \approx 1$ as to the *large* and *small* lattice limits, respectively.

We assume the lattice depth V_T to be sufficiently large so that hopping can be neglected in the small and in the large lattice limits [116].

The Hamiltonian of the system is given by

$$\hat{H} = \hat{H}_K + \hat{H}_Z + \hat{H}_{\text{int}} \tag{6.2}$$

where $\hat{H}_K$ describes the kinetic energy, $\hat{H}_Z$ is the Zeeman term, and $\hat{H}_{\text{int}}$ describes the interactions between particles. These terms are defined by [117, 118]

$$\hat{H}_K = \int d\mathbf{r} \sum_{\sigma=-1,0,1} \hat{\Psi}^\dagger_\sigma(\mathbf{r})\, \hat{h}_0(\mathbf{r}, s, \theta)\, \hat{\Psi}_\sigma(\mathbf{r}), \tag{6.3}$$

$$\hat{H}_Z = \int d\mathbf{r} \sum_{\sigma=-1,0,1} \Delta E_{Z,\sigma}(B)\, \hat{\Psi}^\dagger_\sigma(\mathbf{r})\hat{\Psi}_\sigma(\mathbf{r}), \tag{6.4}$$

$$\hat{H}_{\text{int}} = \frac{1}{2} \int d\mathbf{r}\Big[c_0 \hat{A}^\dagger_{00}(\mathbf{r})\hat{A}_{00}(\mathbf{r}) + c_2 \sum_{m=-2}^{2} \hat{A}^\dagger_{2m}(\mathbf{r})\hat{A}_{2m}(\mathbf{r})\Big], \tag{6.5}$$

where $c_0 = 4\pi\hbar^2(2a_2 + a_0)/(3M)$ and $c_2 = 4\pi\hbar^2(a_2 - a_0)/(3M)$ with a_F the s-wave scattering length of the channel associated with the total angular momentum F, $\hat{h}_0 = (-\hbar^2\nabla^2/2M) + V_{OL}(\mathbf{r}, s, \theta)$ and $\Delta E_{Z,\sigma}(B)$ is the energy shift caused by the Zeeman effect in the presence of a magnetic field $\mathbf{B} = (0, 0, B)$ oriented in the z–direction. The operator

$\hat{A}_{Fm_F}(\mathbf{r})$ is given by

$$\hat{A}_{Fm_F}(\mathbf{r}) = \sum_{m_1,m_2=-f}^{f} \langle F, m_F | f_1, m_1;\, f_2, m_2 \rangle \hat{\Psi}_{m_1}(\mathbf{r}) \hat{\Psi}_{m_2}(\mathbf{r}), \tag{6.6}$$

where $|f_1, m_1;\, f_2, m_2\rangle = |f_1, m_1\rangle \otimes |f_2, m_2\rangle$ and $\langle F, m_F | f_1, m_1;\, f_2, m_2\rangle$ is a Clebsch-Gordan coefficient.

In Sec. 6.10 we derive the effective Hamiltonian describing the dynamics of the atoms at one site using the field operator

$$\hat{\Psi}^{\dagger}_{\sigma}(\mathbf{r}) = \hat{a}^{\dagger}_{\sigma} w_a(\mathbf{r}) + \hat{b}^{\dagger}_{\sigma} w_b(\mathbf{r}), \tag{6.7}$$

where $\hat{a}^{\dagger}_{\sigma}(\hat{b}^{\dagger}_{\sigma})$ is the operator that creates a particle with spin $|f = 1, m_f = \sigma\rangle$ ($\sigma = \{-1, 0, 1\}$ denotes the Zeeman level) in a motional state associated with the symmetric (anti-symmetric) mode function $w_a(w_b)$. The mode functions are centered in the middle of the site, and their shape depends on the lattice parameter s. The field operators obey the canonical bosonic commutation relations $[\hat{\Psi}_{\sigma}(\mathbf{r}), \hat{\Psi}^{\dagger}_{\sigma'}(\mathbf{r}')] = \delta_{\sigma\sigma'}\delta(\mathbf{r} - \mathbf{r}')$ and $[\hat{\Psi}_{\sigma}(\mathbf{r}), \hat{\Psi}_{\sigma'}(\mathbf{r}')] = [\hat{\Psi}^{\dagger}_{\sigma}(\mathbf{r}), \hat{\Psi}^{\dagger}_{\sigma'}(\mathbf{r}')] = 0$. We will see in the next section that the inclusion of a second motional mode in the Hamiltonian allows an accurate description of the dynamics of the system in both the large *and* the small lattice limit [119]. A more detailed explanation of the interaction term (6.5) as well as the full Hamiltonian of the system in terms of creation (annihilation) operators can be found in Sec. 6.10.

6.3 Creation of a Bell state on every lattice site

In this section, we use the effective Hamiltonian introduced in the previous section to show how to generate a lattice where every site contains a Bell state encoded on the Zeeman levels of the atoms. This procedure will be used as a preliminary step to engineer several types of many-body entangled states.

We start with a deep optical lattice in the large lattice limit (LLL) and two atoms per lattice site in the state

$$|\psi_{\rm init}\rangle = w_a(\mathbf{r})^2 \otimes \mathcal{S}\left(|f_1 = 1, m_1 = +1; f_2 = 1, m_2 = -1\rangle\right), \tag{6.8}$$

where $\mathcal{S}$ is the symmetrization operator. In general, the two atoms can undergo spin-changing collisions coupling to various hyperfine levels. As we want to implement qubits on the Zeeman levels, we will limit the spin dynamics effectively to two hyperfine states. There are several ways to achieve this in practice: (i) One possibility is to exploit the conservation of angular momentum and choose two states such as $|f = 2, m_f = +2\rangle$ and $|f = 1, m_f = +1\rangle$, which are not coupled to any other hyperfine states by the interatomic interaction. (ii) An accidental degeneracy in ^{87}Rb offers another possible route: since the two s-wave scattering lengths a_0 and a_2 are almost equal, transitions between the states $|f_1 = 1, m_1 = +1; f_2 = 1, m_2 = -1\rangle$ and $|f_1 = 1, m_1 = 0; f_2 = 1, m_2 = 0\rangle$ occur on a time scale $(c_0 + c_2)/c_2 \approx 3a_2/(a_2 - a_0) \approx 300$ times slower than any other allowed transition. Hence, after initializing the system at time $t = 0$ in state (6.8), we can limit our dynamical description to transitions between states with opposite spins, as long as the manipulations we are about to propose happen on a faster time scale than this transition. Notice that the use of fast-switched microwave fields that suppress spin-changing collisions [99] allows the relaxation of the constraint to be faster than the original time-scale of spin-changing collisions. The preparation of the state (6.8) has already been experimentally achieved [56, 100].

The first step in our proposal consists of raising the superlattice potential, i.e. changing the lattice parameter $s(t)$ from the LLL at time $t = 0$ to the small lattice limit (SLL) at some time $t = T$ sufficiently slowly so that the ramp does not create excitations in the system. Once the superlattice is fully ramped up, each site is split in two, atoms no longer interact with each other and their spin state remains frozen in time.

The shape of the mode functions $w_a(\mathbf{r})$ and $w_b(\mathbf{r})$ depends on the lattice parameter. In the LLL, they correspond to the ground and first excited state of each lattice site. However, as the lattice parameter s approaches the SLL, the mode functions transform into the symmetric and anti-symmetric superpositions $w_a(\mathbf{r}) = [\varphi_L(\mathbf{r}) + \varphi_R(\mathbf{r})]/\sqrt{2}$ and $w_b(\mathbf{r}) = [\varphi_L(\mathbf{r}) - \varphi_R(\mathbf{r})]/\sqrt{2}$, where the mode functions $\varphi_L(\mathbf{r})$ and $\varphi_R(\mathbf{r})$ are centered on either side of the double-well potential [119, 107]. Hence, when the mode functions $w_{L,R}(\mathbf{r})$ become centered within each subsite [119], it is convenient to write the Hamiltonian of the system in terms of the operators

$$
\begin{aligned}
\hat{c}^\dagger_{L,\sigma} &= (\hat{a}^\dagger_\sigma + \hat{b}^\dagger_\sigma)/\sqrt{2} \\
\hat{c}^\dagger_{R,\sigma} &= (\hat{a}^\dagger_\sigma - \hat{b}^\dagger_\sigma)/\sqrt{2},
\end{aligned}
\tag{6.9}
$$

which create a particle with spin σ on the left and right side of the double-well potential, respectively. In the basis

$$
\begin{aligned}
|\uparrow\downarrow,\rangle &= \hat{c}^\dagger_{L,\uparrow}\hat{c}^\dagger_{L,\downarrow}|\mathrm{vac}\rangle = (\hat{a}^\dagger_\uparrow + \hat{b}^\dagger_\uparrow)(\hat{a}^\dagger_\downarrow + \hat{b}^\dagger_\downarrow)/2|\mathrm{vac}\rangle, \\
|\uparrow,\downarrow\rangle &= \hat{c}^\dagger_{L,\uparrow}\hat{c}^\dagger_{R,\downarrow}|\mathrm{vac}\rangle = (\hat{a}^\dagger_\uparrow + \hat{b}^\dagger_\uparrow)(\hat{a}^\dagger_\downarrow - \hat{b}^\dagger_\downarrow)/2|\mathrm{vac}\rangle, \\
|\downarrow,\uparrow\rangle &= \hat{c}^\dagger_{L,\uparrow}\hat{c}^\dagger_{R,\downarrow}|\mathrm{vac}\rangle = (\hat{a}^\dagger_\uparrow - \hat{b}^\dagger_\uparrow)(\hat{a}^\dagger_\downarrow + \hat{b}^\dagger_\downarrow)/2|\mathrm{vac}\rangle, \\
|,\uparrow\downarrow\rangle &= \hat{c}^\dagger_{R,\uparrow}\hat{c}^\dagger_{R,\downarrow}|\mathrm{vac}\rangle = (\hat{a}^\dagger_\uparrow - \hat{b}^\dagger_\uparrow)(\hat{a}^\dagger_\downarrow - \hat{b}^\dagger_\downarrow)/2|\mathrm{vac}\rangle,
\end{aligned}
\tag{6.10}
$$

the Hamiltonian of the system reads (see 6.10)

$$
\hat{H}_{\uparrow\downarrow} = \begin{pmatrix}
\tilde{E} + \tilde{U}_{\uparrow\downarrow} & \tilde{J}_{\uparrow\downarrow} & \tilde{J}_{\uparrow\downarrow} & \chi_{\uparrow\downarrow} \\
\tilde{J}_{\uparrow\downarrow} & \tilde{E} + \chi_{\uparrow\downarrow} & \chi_{\uparrow\downarrow} & \tilde{J}_{\uparrow\downarrow} \\
\tilde{J}_{\uparrow\downarrow} & \chi_{\uparrow\downarrow} & \tilde{E} + \chi_{\uparrow\downarrow} & \tilde{J}_{\uparrow\downarrow} \\
\chi_{\uparrow\downarrow} & \tilde{J}_{\uparrow\downarrow} & \tilde{J}_{\uparrow\downarrow} & \tilde{E} + \tilde{U}_{\uparrow\downarrow}
\end{pmatrix},
\tag{6.11}
$$

where $\tilde{E} = V_a + V_b$ with $V_\nu = \int d\mathbf{r}\, w^*_\nu(\mathbf{r})\hat{h}_0\, w_\nu(\mathbf{r})$ and $\hat{h}_0 = (-\hbar^2\nabla^2/2M) + V_{OL}(\mathbf{r}, s, \theta)$ is the sum of the single-particle energies, $\tilde{U}_{\uparrow\downarrow} = \gamma_{\uparrow\downarrow}(U_{aa} + U_{bb} + 6U_{ab})/4$ with $U_{\nu\nu'} = \int d\mathbf{r}\,(|w_\nu(\mathbf{r})||w_{\nu'}(\mathbf{r})|)^2$ and $\gamma_{\uparrow\downarrow} = c_0 - c_2$ is the generalized on-site interaction, $\tilde{J}_{\uparrow\downarrow} = (V_a - V_b)/2 + \gamma_{\uparrow\downarrow}(U_{aa} - U_{bb})/4$ the generalized tunneling matrix element between the two sides of the well, and $\chi_{\uparrow\downarrow} = \gamma_{\uparrow\downarrow}(U_{aa} + U_{bb} - 2U_{ab})/4$ corresponds to the density-density

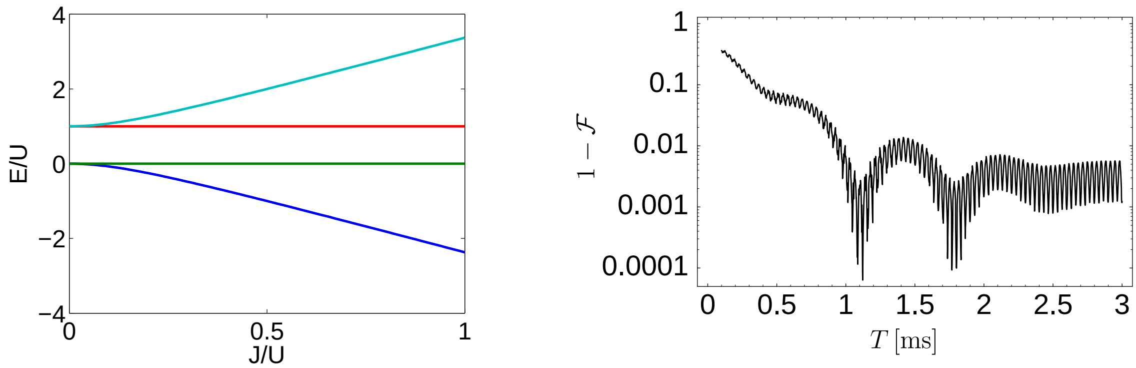

Fig. 6.2: (Left) Energy spectrum of the Hamiltonian $\hat{H}^{\mathrm{SLL}}_{\uparrow\downarrow}$ in Eq. (6.12) as a function of the ratio J/U. (Right) Numerical calculation of the anti-fidelity $1-\mathcal{F}$ where $\mathcal{F} = |\langle\psi|\psi_0\rangle|^2$ with $|\psi\rangle$ the state of the two atoms at the end of the ramping. We have used the parameters of a lattice with period $a = \lambda/2$, $\lambda = 840\,\mathrm{nm}$, and $V_T = 60E_R$, initialized with two ^{87}Rb atoms per site in the state (6.8) at time $T = 0$ and a magnetic field of $B = 30\,\mathrm{G}$.

interaction energy between the two sides of the double-well. The latter is proportional to the overlap between the functions $\varphi_L(\mathbf{r})$ and $\varphi_R(\mathbf{r})$. It cancels in the small lattice limit as a consequence of the localization of the mode functions $\varphi_L(\mathbf{r})$ and $\varphi_R(\mathbf{r})$ inside each subsite.

Our two-mode model does not only describe the system well in both limits, it also takes into account the effects of density-density interactions between two subsites when the potential barrier between them is still not fully ramped up. This property makes it particularly valuable for the study of the system dynamics *between* the two limits.

In the SLL, the Hamiltonian (6.11) reduces (up to the energy shift E) to

$$\hat{H}^{\mathrm{SLL}}_{\uparrow\downarrow} = \begin{pmatrix} U_{\uparrow\downarrow} & -J & -J & 0 \\ -J & 0 & 0 & -J \\ -J & 0 & 0 & -J \\ 0 & -J & -J & U_{\uparrow\downarrow} \end{pmatrix}. \tag{6.12}$$

where $V_a = E - J$ and $V_b = E + J$ with $E = \int \mathrm{d}\mathbf{r}\, \varphi_L^*(\mathbf{r})\hat{h}_0\, \varphi_L(\mathbf{r})$ is the single-particle energy and $J = \int \mathrm{d}\mathbf{r}\, \varphi_L^*(\mathbf{r})\hat{h}_0\, \varphi_R(\mathbf{r})$ the hopping integral, and $U_{\uparrow\downarrow} = \gamma_{\uparrow\downarrow} \int \mathrm{d}\mathbf{r}\, |\varphi_L|^4$ is the on-site interaction [119]. Its spectrum as a function of the ratio J/U is shown in Fig. 6.2.

For zero tunneling $J = 0$, the Hamiltonian $\hat{H}^{\mathrm{SLL}}_{\uparrow\downarrow}$ has two degenerate ground states:

$|\uparrow,\downarrow\rangle$ and $|\downarrow,\uparrow\rangle$. This degeneracy is lifted at finite J where the symmetric superposition

$$|\psi_0\rangle = \frac{1}{\sqrt{2}}(|\uparrow,\downarrow\rangle + |\downarrow,\uparrow\rangle) \tag{6.13}$$

is the ground and the antisymmetric superposition the first excited state. These two low-lying energy levels with an energy splitting of $4J^2/U_{\uparrow\downarrow}$ are separated from the other excited states by the interaction energy $U_{\uparrow\downarrow}$.

We have carried out a dynamical simulation of the splitting dynamics using the exact *full* Hamiltonian defined in Eq. (6.2) and Sec. 6.10 for two particles and one site. For the time-scales considered throughout this chapter, non-adiabatic effects due to the changes of shape of the mode functions can be safely neglected [119]. We have used $s(t) = \sin^2[t/(2T)]$, and computed the anti-fidelity $1-\mathcal{F}$ with $\mathcal{F} = |\langle\psi|\psi_0\rangle|^2$ between the state $|\psi\rangle$ of the system at the end of the numerical simulation of the ramp and the Bell state (6.13). For the parameters considered, we have found that the anti-fidelity reaches $1-\mathcal{F} \approx 10^{-3}$ for a quench time of $T \sim 1.1 \pm 0.1$ ms (see Fig. 6.2). It is expected that better fidelity can be obtained for larger values of $U_{\uparrow\downarrow}$ [120]. This observation makes our scheme relevant for current experimental setups.

Thus, changing the topology of the optical lattice from the LLL to the SLL drives the state of the atoms within each lattice site from (6.8) to the maximally-entangled Bell state (6.13). Non-adiabatic transitions to excited states are suppressed by opposite parity in the case of the first excited state and by the on-site interaction $U_{\uparrow\downarrow}$ in the case of the other excited states. After this first step has been completed, a system of initially N sites contains $k = 2N$ subsites and its state is given by a tensor product of Bell pairs

$$|\Phi_k^{(0)}\rangle = \bigotimes_{i=1}^{N} |\psi_0\rangle. \tag{6.14}$$

Remarkably, the system in state (6.14) is resilient to dephasing noise for a magnetic field slowly varying over a distance of one lattice site [66].

6.4 Implementation of an entangling gate

Since the interactions between two atoms depend on the overlap between their wave functions, they can be dynamically switched on and off by lowering and raising the potential barrier between the two subsites. This is done by varying the lattice parameter s from $s = 1$ at time $t = 0$ to $s = 1 - \eta$ and back to $s = 1$ at time $t = \tau$. In the SLL, where $\tilde{J}_{\uparrow\downarrow}/\tilde{U}_{\uparrow\downarrow} \ll 1$, tunneling can be treated perturbatively, and the Hamiltonian (6.11) can be projected onto the subspace of singly-occupied sites.

We distinguish two cases: either the neighboring subsites are occupied by atoms with opposite or equal spins. For two atoms with opposite spins, we can use Eq. (6.11) and the effective Hamiltonian in the basis $|\uparrow,\downarrow\rangle$ and $|\downarrow,\uparrow\rangle$ reads (up to a constant energy shift) in second-order perturbation theory

$$\hat{H}^{(\mathrm{eff})}_{\uparrow\downarrow} = \left(\frac{2\tilde{J}^2_{\uparrow\downarrow}}{\tilde{U}_{\uparrow\downarrow}} + \chi_{\uparrow\downarrow}\right)\begin{pmatrix} 1 & 1 \\ 1 & 1 \end{pmatrix}. \tag{6.15}$$

Since the effective Hamiltonian commutes with itself at different times, we obtain the following analytical expression for the time evolution operator

$$\hat{U}(\tau) = \exp\left(-\frac{\mathrm{i}}{\hbar}\int_0^\tau H^{(\mathrm{eff})}_{\uparrow\downarrow}\,\mathrm{d}t\right) = \begin{pmatrix} \mathrm{e}^{-\mathrm{i}\phi}\cos\phi & -\mathrm{i}\mathrm{e}^{-\mathrm{i}\phi}\sin\phi \\ -\mathrm{i}\mathrm{e}^{-\mathrm{i}\phi}\sin\phi & \mathrm{e}^{-\mathrm{i}\phi}\cos\phi \end{pmatrix}, \tag{6.16}$$

where the phase ϕ is given by

$$\phi(\tau) = \frac{1}{\hbar}\int_0^\tau \left(\frac{2\tilde{J}^2_{\uparrow\downarrow}}{\tilde{U}_{\uparrow\downarrow}} + \chi_{\uparrow\downarrow}\right)\mathrm{d}t. \tag{6.17}$$

While the first term in Eq. (6.17) is due to second-order tunneling [103, 65], the second term is due to density-density interactions. This term is negligible in the SLL, but when the potential barrier between the two sides of the double-well is reduced, it adds an extra phase between neighboring particles with different spins because of the difference between the scattering lengths c_0 and c_2.

For atoms with equal spins $\sigma = \{\uparrow, \downarrow\}$ we start by writing down the basis states as

$$
\begin{aligned}
|\sigma\sigma,\rangle &= \hat{c}^\dagger_{L,\sigma}\hat{c}^\dagger_{L,\sigma}|\text{vac}\rangle = (\hat{a}^\dagger_\sigma + \hat{b}^\dagger_\sigma)(\hat{a}^\dagger_\sigma + \hat{b}^\dagger_\sigma)/(2\sqrt{2})|\text{vac}\rangle \\
|\sigma,\sigma\rangle &= \hat{c}^\dagger_{L,\sigma}\hat{c}^\dagger_{R,\sigma}|\text{vac}\rangle = (\hat{a}^\dagger_\sigma + \hat{b}^\dagger_\sigma)(\hat{a}^\dagger_\sigma - \hat{b}^\dagger_\sigma)/2|\text{vac}\rangle \\
|,\sigma\sigma\rangle &= \hat{c}^\dagger_{R,\sigma}\hat{c}^\dagger_{R,\sigma}|\text{vac}\rangle = (\hat{a}^\dagger_\sigma - \hat{b}^\dagger_\sigma)(\hat{a}^\dagger_\sigma - \hat{b}^\dagger_\sigma)/(2\sqrt{2})|\text{vac}\rangle,
\end{aligned}
\tag{6.18}
$$

in which the Hamiltonian reads

$$
\hat{H}_{\sigma\sigma} = \begin{pmatrix} \tilde{E}_{\sigma\sigma} + \tilde{U}_{\sigma\sigma} & \tilde{J}_{\sigma\sigma} & \chi_{\sigma\sigma} \\ \tilde{J}_{\sigma\sigma} & \tilde{E}_{\sigma\sigma} + \chi_{\sigma\sigma} & \tilde{J}_{\sigma\sigma} \\ \chi_{\sigma\sigma} & \tilde{J}_{\sigma\sigma} & \tilde{E}_{\sigma\sigma} + \tilde{U}_{\sigma\sigma} \end{pmatrix}, \tag{6.19}
$$

where $\gamma_{\sigma\sigma} = c_0 + c_2$ is the interaction constant for particles with equal spin σ, $\tilde{E}_{\sigma\sigma} = V_a + V_b \pm E_Z$ the sum of single-particle energies, $E_Z = -g\mu_B B\tau/2\hbar$ the Zeeman energy shift in the first order, $\tilde{J}_{\sigma\sigma} = (V_a - V_b)/\sqrt{2} + \gamma_{\sigma\sigma}(U_{aa} - U_{bb})/4$ the generalized tunneling matrix element, $\tilde{U}_{\sigma\sigma} = \gamma_{\sigma\sigma}(U_{aa} + U_{bb} + 6U_{ab})/4$ the generalized on-site interaction and $\chi_{\sigma\sigma} = \gamma_{\sigma\sigma}(U_{aa} + U_{bb} - 2U_{ab})/4$ the off-site density-density interaction.

In the SLL this reduces (up to the energy shift of $\tilde{E}_{\sigma\sigma}$) to

$$
\hat{H}^{SLL}_{\sigma\sigma} = \begin{pmatrix} U_{\sigma\sigma} & -\sqrt{2}J & 0 \\ -\sqrt{2}J & 0 & -\sqrt{2}J \\ 0 & -\sqrt{2}J & U_{\sigma\sigma} \end{pmatrix}. \tag{6.20}
$$

For the state $|\sigma,\sigma\rangle$ there are no other low-energy states accessible, so that it acquires only the phase factor $\mathrm{e}^{\mathrm{i}\kappa}$ during the sweep. In second-order perturbation theory we find that κ is similar to (6.17)

$$
\kappa = \frac{1}{\hbar}\int_0^\tau \left(\frac{2\tilde{J}^2_{\sigma\sigma}}{\tilde{U}_{\sigma\sigma}} + \chi_{\sigma\sigma}\right)\mathrm{d}t. \tag{6.21}
$$

Since $\tilde{J}_{\uparrow\downarrow} \to -J$, $\tilde{J}_{\sigma\sigma} \to -\sqrt{2}J$ and $\gamma_{\uparrow\downarrow}/\gamma_{\sigma\sigma} = (c_0 - c_2)/(c_0 + c_2) \approx 1$, we get $\kappa \approx 2\phi$.

Putting the results of this section together we find that lowering and raising the potential barrier between two subsites n and $n+1$ implements the two-qubit gate $\hat{U}$

$$
\hat{U}\begin{pmatrix} |00\rangle \\ |01\rangle \\ |10\rangle \\ |11\rangle \end{pmatrix} = \begin{pmatrix} \mathrm{e}^{\mathrm{i}E_Z\tau} & 0 & 0 & 0 \\ 0 & \mathrm{e}^{\mathrm{i}\phi}\cos\phi & -\mathrm{i}\mathrm{e}^{\mathrm{i}\phi}\sin\phi & 0 \\ 0 & -\mathrm{i}\mathrm{e}^{\mathrm{i}\phi}\sin\phi & \mathrm{e}^{\mathrm{i}\phi}\cos\phi & 0 \\ 0 & 0 & 0 & \mathrm{e}^{-\mathrm{i}E_Z\tau} \end{pmatrix}\begin{pmatrix} |00\rangle \\ |01\rangle \\ |10\rangle \\ |11\rangle \end{pmatrix}, \tag{6.22}
$$

where $|ij\rangle = |i\rangle_n \otimes |j\rangle_{n+1}$ with $|1\rangle_n = \hat{c}^\dagger_{n,\uparrow}|\text{vac}\rangle$ and $|0\rangle_n = \hat{c}^\dagger_{n,\downarrow}|\text{vac}\rangle$ where $\hat{c}^\dagger_{n,\downarrow}$ and $\hat{c}^\dagger_{n,\uparrow}$ are the creation operators of a particle at subsite n with spin $\downarrow$ and $\uparrow$, respectively.

Numerical simulations of the system dynamics have been carried out using the exact full Hamiltonian for two particles and one site—that is, including the contribution of spin changing collisions to the $m_f = 0$ state—for a system of ^{87}Rb atoms, $V_T = 60E_R$ and $\eta = 0.3$. We have computed the overlap between the states resulting from the numerical simulation with their analytical approximation and found that for the parameters considered and switching times τ up to tens of milliseconds, the time evolution operator of the system is accurately approximated by Eq. (6.22). For longer times τ, the evolution of the system in the reduced Hilbert becomes non-unitary due to slow transitions to the state where the two particles have spins $\sigma = 0$, as expected.

Since the application of the gate $\hat{U}$ is realized in parallel on all qubits in the x–direction, the phase due to the Zeeman shift in the first order in B cancels for systems with an equal number of atoms in the $\sigma = +1$ and $\sigma = -1$ state. For such systems, we find that for ramping times τ such that $\phi(\tau) = \{\pi/4, \pi/2, 3\pi/4\}$, lattice manipulations realize the gates (in the usual computational basis) [26]

$$\hat{U}_{\frac{\pi}{4}} = \sqrt{\text{SWAP}} \tag{6.23}$$

$$\hat{U}_{\frac{\pi}{2}} = \text{SWAP}, \tag{6.24}$$

$$\hat{U}_{\frac{3\pi}{4}} = \text{SWAP}\sqrt{\text{SWAP}} = \sqrt{\text{SWAP}}^\dagger. \tag{6.25}$$

In the remainder of this chapter we will show that, using a lattice of Bell pairs as a starting point, this gate[3] can be used to create both many-body entangled states and a resource state for MBQC.

[3] In the context of optical lattices, different methods to implement this gate have been put forward for different encodings of the logical qubits [121, 122, 123]. Recently, a $\sqrt{\text{SWAP}}$ gate between qubits encoded on the internal spin state of the atoms was realized experimentally by manipulating both the spin and motional degrees of freedom of the atoms by means of optical superlattices [66].

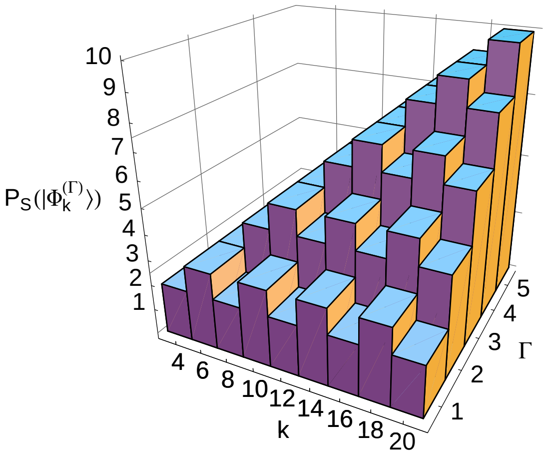

Fig. 6.3: Schmidt measure of the state (6.29) as a function of Γ and k. The Schmidt decomposition of the state (6.29) was calculated by partitioning the system in equal parts, which yields the maximum possible Schmidt rank.

6.5 Creation and detection of a state with a tunable amount of entanglement

Depending on whether the lattice parameter θ is set to $\theta = 0$ or $\theta = \pi/2$, the gate U_ϕ in Eq. (6.22) is applied between neighboring subsites inside or between lattice sites, respectively. Up to an irrelevant global phase, these operations read

$$\hat{\mathcal{U}}^{\text{in}}(\hat{U}) = \bigotimes_{n=1}^{N} \hat{U} \tag{6.26}$$

or

$$\hat{\mathcal{U}}^{\text{bw}}(\hat{U}) = \hat{\mathbb{1}} \otimes \bigotimes_{n=1}^{N-1} \hat{U} \otimes \hat{\mathbb{1}}. \tag{6.27}$$

Using this notation, we define a *knitting* operator by

$$\hat{\mathcal{K}}(\hat{U}) = \hat{\mathcal{U}}^{\text{in}}(\hat{U})\hat{\mathcal{U}}^{\text{bw}}(\hat{U}). \tag{6.28}$$

Starting from a lattice of Bell pairs, the state resulting from Γ successive applications of the operator $\hat{\mathcal{K}}(\hat{\mathcal{U}}_{\frac{\pi}{4}})$ on the state (6.14) is denoted by

$$|\Phi_k^{(\Gamma)}\rangle = \hat{\mathcal{K}}(\hat{U}_{\frac{\pi}{4}})^{\Gamma}|\Phi_k^{(0)}\rangle. \tag{6.29}$$

In Fig. 6.3, we have plotted the Schmidt measure P_s^L of the state (6.29) for up to $k = 20$ qubits and partitions of size $L = 10$ as a function of Γ [124, 61]. We find that the Schmidt rank of the state is directly proportional to Γ, i.e. applying the entangling knitting operator (6.28) first connects the initial Bell pairs and then further increases the entanglement content of the state. The largest possible Schmidt measure $\max[P_s^L(|\Phi_k^{(\Gamma)}\rangle)] = k/2$ is reached after $\Gamma = N/2$ applications of the operator (6.28). Once the maximum value for the Schmidt measure is reached, it remains unaffected by further applications of the operator (6.28). We note that since the operator $\hat{U}$ conserves the total number of spins, the state (6.29) is resilient to collective dephasing noise. Recent experimental results suggest that resilience to this type of noise significantly increases the decoherence time of the system [66].

Since the application of the gate $\hat{\mathcal{K}}(\hat{U}_{\frac{\pi}{4}})$ affects the density correlations in the lattice, its effect on the system can be observed experimentally via state-selective measurement of the quasi-momentum distribution (QMD) of atoms with spin up [17, 66]

$$n_q^{\uparrow} = \frac{1}{2N} \sum_{i,j=1}^{2N} \mathrm{e}^{-\mathrm{i}\pi q(i-j)/N} \langle \hat{c}_{i,\uparrow}^{\dagger} \hat{c}_{j,\uparrow} \rangle. \tag{6.30}$$

As an illustration, we have plotted in Fig. 6.4 the QMD of a system of $k = 14$ atoms after $\Gamma = 1$ and $\Gamma = 7$ applications of the operator $\hat{\mathcal{K}}(\hat{U}_{\frac{\pi}{4}})$ on the state (6.14). Hence, starting from a lattice of Bell pairs, superlattice manipulations allow the creation of an entangled state with a tunable Schmidt rank that has a distinct experimental signature and is resilient to collective dephasing noise. These properties make this state suitable for experimental studies of many-body entanglement.

6.6 Creation of maximally entangled states

Together with site-selective single-qubit operations applied in parallel on every second atom, superlattice manipulations can be used to implement the entangling phase-gate op-

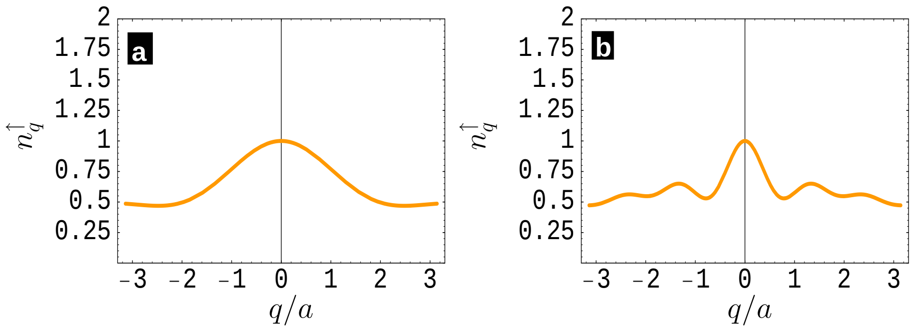

Fig. 6.4: (a) Quasi-momentum distribution of $k = 14$ atoms after the application of the gate $\hat{\mathcal{K}}(\hat{U}_{\frac{\pi}{4}})^{\Gamma}$ on the state (6.14) for (a) $\Gamma = 1$ and (b) $\Gamma = 7$. After $\Gamma = 7$ applications of the knitting operator, the state is maximally entangled.

eration

$$\hat{C}_{\mathrm{i}} = \hat{U}_{\frac{\pi}{4}}(\hat{Z} \otimes \hat{\mathbb{1}})\hat{U}_{\frac{\pi}{4}}(\hat{\mathbb{1}} \otimes \hat{Z}), \tag{6.31}$$

where $\hat{C}_{\mathrm{i}} = \mathrm{diag}(1, -\mathrm{i}, -\mathrm{i}, 1)$ and $\hat{Z}$ is the Pauli matrix defined as $\hat{Z} = \mathrm{diag}(1, -1)$ in the usual computational basis. The gate $\hat{C}_{\mathrm{i}}$ is related to the operation $\hat{C}_Z = \mathrm{diag}(1, 1, 1, -1)$ by applying the single-qubit gate $\sqrt{\hat{Z}} \otimes \sqrt{\hat{Z}}$ on every site of the lattice. A proposal for realizing arbitrary single-qubit gates on individual atoms in an optical lattice can be found in Ref. [125]. Notice that the single-qubit operations required to implement the gate (6.31) between sites can be performed in parallel, and so each site need not be addressed separately. The implementation of a phase gate directly followed by a SWAP gate

$$(\mathrm{SWAP})\,\hat{C}_i = \hat{U}^{\dagger}_{\frac{\pi}{4}}(\hat{Z} \otimes \hat{\mathbb{1}})\hat{U}_{\frac{\pi}{4}}(\hat{\mathbb{1}} \otimes \hat{Z}) \tag{6.32}$$

is accomplished by adjusting the switching time τ of the last gate. The operation (6.32) is equivalent to $(\mathrm{SWAP})\,\hat{C}_Z$ up to the unitary transformation $\sqrt{\hat{Z}} \otimes \sqrt{\hat{Z}}$. Since the $\hat{C}_Z$ operations between different qubits commute, $k/2$ successive applications of the operator $\hat{\mathcal{K}}((\mathrm{SWAP})\hat{C}_Z)$ on the state $|+\rangle^{\otimes k}$ ($|\pm\rangle = (|0\rangle \pm |1\rangle)/\sqrt{2}$) create a complete graph state $|K_N\rangle$. Complete graphs have the property that each vertex is connected to all the vertices of the graph, i.e. a complete graph of k vertices contains $k(k-1)/2$ edges. Graph states

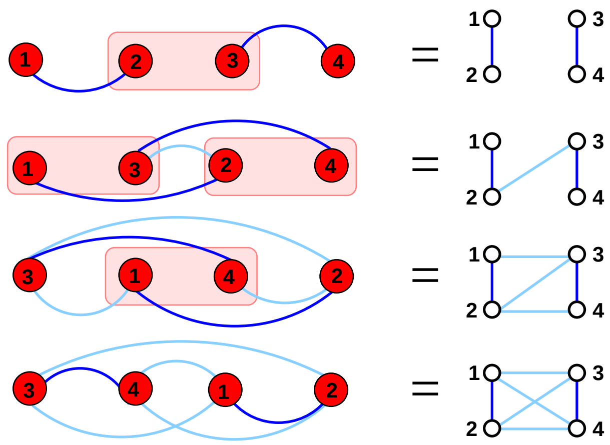

Fig. 6.5: Schematic representations of the process leading to state (6.33). Qubits initially forming a Bell pair are linked by a dark blue line. The boxes depict the location where the $\sqrt{\mathrm{SWAP}}^{\dagger} = \mathrm{SWAP}\sqrt{\mathrm{SWAP}}$ is performed. After a $\sqrt{\mathrm{SWAP}}$ gate has been applied between two qubits, they are connected by a (light) blue line. Numerical calculations show that for up to 8 qubits, the state (6.33) is equivalent to a complete graph state under local unitary operations.

of complete graphs are equivalent to the maximally entangled state $|GHZ\rangle = (|0\rangle^{\otimes k} + |1\rangle^{\otimes k})/\sqrt{2}$ up to local unitary operations.

Superlattice manipulations alone allow the realization of the state

$$|\Phi_k^{\mathrm{graph}}\rangle = \hat{\mathcal{U}}^{\mathrm{bw}}(\hat{U}_{\frac{\pi}{4}}^{\dagger})\hat{\mathcal{K}}(\hat{U}_{\frac{\pi}{4}}^{\dagger})^{(k/2)-1}|\Phi_k^{(0)}\rangle \tag{6.33}$$

resulting from $k-1$ successive applications of the operator (6.25) between and inside each site. The process leading to state (6.33) is schematically represented in Fig. 6.5. This state is resilient to collective dephasing noise, and possesses a structure similar to a complete graph state (see Fig. 6.5). Via the brute-force numerical calculation of the parameters of single-qubit unitary operations, we have found that (6.33) is locally equivalent to a complete graph state of the same size for up to $k = \{4, 6, 8\}$ qubits. This suggests that this property holds for an arbitrary number of qubits.

The resilience of this state to collective dephasing noise, and its symmetry properties make it a good candidate for the improvement of the sensitivity of quantum spectroscopic measurements in noisy environments (see Ref. [126]).

6.7 Measurement-based quantum computation

In the circuit model of quantum computation, unitary operations are decomposed into a network of elementary quantum gases such as the CNOT gate and single-qubit rotations [26]. In one-way quantum computation or measurement-based quantum computation (MBQC), on the other hand, the quantum correlations in an entangled state are exploited for universal quantum computation through single-qubit measurements alone [62, 114]. In this section we review the basics of MBQC following the review article [127].

The initial entangled resource state is usually assumed to be a cluster state. Nowadays, the term cluster or graph state does not refer to a single quantum state, but rather to a family of quantum states. A graph is defined as a network of connected nodes. A cluster state corresponding to a certain graph is obtained by (1) placing a qubit at each of the nodes prepared in the state $|+\rangle = (|0\rangle + |1\rangle) / \sqrt{2}$ and (2) applying a controlled-phase gate, i.e. $\hat{C}_Z = |0\rangle\langle 0| \otimes \hat{\mathbb{1}} + |1\rangle\langle 1| \otimes \hat{Z}$ with $\hat{Z}\,|0\rangle = |0\rangle$ and $\hat{Z}\,|1\rangle = -|1\rangle$, between the qubits whose corresponding nodes are connected. Since controlled phase gates commute with each other, the order in which these gates are applied need not to be specified.

Once the cluster state is prepared, the computation is performed by a sequence of single-qubit measurements in a certain order and in certain basis sets. To understand the key idea, let us follow a simple example related to single-qubit teleportation [26]. Consider a two qubit system: one in an unknown quantum state $|\psi\rangle = \alpha|0\rangle + \beta|1\rangle$ and the other initialized in the state $|+\rangle = (|0\rangle + |1\rangle)/\sqrt{2}$. After applying a controlled phase gate, the two qubits are in the state $\alpha|0\rangle|+\rangle + \beta|1\rangle|-\rangle$. If we measure the first qubit in the basis $\{(|0\rangle \pm e^{i\phi}|1\rangle)/\sqrt{2}\}$, there are two outcomes with equal probability. If the measurement returns $+1$, the second qubit is projected into the state $\alpha|+\rangle + e^{i\phi}\beta|-\rangle$. If it returns -1, it is

$\alpha|+\rangle - e^{i\phi}\beta|-\rangle$. Encoding the measurement outcome +1 with $m = 0$ and −1 with $m = 1$, this state can be written as

$$\hat{X}^m \hat{H} \hat{U}_z(\phi)|\psi\rangle \tag{6.34}$$

with the Pauli matrix $\hat{X}$, i.e. $\hat{X}|\pm\rangle = \pm|\pm\rangle$, the Hadamard gate $\hat{H} = \frac{1}{\sqrt{2}}\begin{pmatrix} 1 & 1 \\ 1 & -1 \end{pmatrix}$ and $U_z(\phi)$ the operator which rotates the Bloch vector of the state $|\psi\rangle$ about the angle ϕ around the z axis.

In this simple example we already find three important features of MBQC:

- the unknown quantum state $|\psi\rangle$ has been teleported to the second qubit and the quantum information is therefore not lost despite the measurement process on the first qubit
- depending on the choice of the measurement basis a single-qubit rotation $\hat{U}_z(\phi)$ is applied on the quantum state $|\psi\rangle$ and
- the final state depends on the outcome of the measurement m on the first qubit and the two outcomes differ by an additional Pauli matrix $\hat{X}$, a so-called by-product operator. This introduces a temporal ordering in the computing scheme, since the choice of later measurement basis sets will depend on earlier measurement outcomes.

The generalization to arbitrary single-qubit rotations is straightforward via Euler's rotation theorem, and two qubit gates are realized with the controlled phase gates which are already at hand in the cluster state preparation. If we take for example the cluster corresponding to a 2D square lattice, quantum information can be propagated horizontally through the lattice by measuring qubits along this axis alongside with single-qubit rotations, while qubits on vertical connections are used to realize two-qubit quantum gates.

Cluster states have been realized using cold collisions of ultracold bosons in state-dependent one-dimensional optical lattices [128] as proposed in Ref. [58]. Current technology does not allow for measurements of atoms at single sites of the optical lattice, but one-way quantum computation has been demonstrated with a small cluster state of photons [129, 130].

6.8 Creation of a resource for MBQC

In this section, we will show how to create a state useful for MBQC via the application of the $\hat{C}_Z$ gate via lattice manipulations in both the x and y direction. This state is formally similar to a Bell-encoded cluster state, and hence its utilization as a resource for MBQC only requires an adjustment of the measurement networks used for cluster states. To demonstrate the universality of our resource for MBQC and derive the measurement networks required to perform quantum algorithms, we will employ the method recently developed by Gross and Eisert in Ref. [131, 132], which connects the matrix product representation (MPR) of a state with its computational power. A review of the basics concepts presented in Ref. [131] can be found in Sec. 6.10.

The MPR for a chain of k systems of dimension $d = 2$ (qubits) is given by

$$|\psi_\Lambda\rangle = \sum_{i_1 \ldots i_k = \{0,1\}} \langle R|\hat{\Lambda}_1^{[i_1]} \cdots \hat{\Lambda}_k^{[i_k]}|L\rangle |i_1 \cdots i_k\rangle. \tag{6.35}$$

It is specified by a set of $2k$ $D \times D$-matrices, which we will refer to as the correlation matrices, and two D-dimensional vectors $|L\rangle$ and $|R\rangle$ representing boundary conditions. The parameter D is proportional to the amount of correlation between two consecutive blocks of the chain. Notice that the right boundary condition vector $|R\rangle$ appears on the left. This choice improves the clarity of calculations later when we will use the graphical notation explained in Sec. 6.10.

Starting from a lattice of Bell pairs, we find that the state resulting from the application of the gate $\hat{\mathcal{U}}^{\rm bw}(\hat{C}_Z)$ on the state $|\Phi_k^{(0)}\rangle$ (6.14) has the MPS

$$|\psi_{AB}\rangle = \sum_{i_1 \ldots i_k = \{0,1\}} \langle R|\hat{A}^{[i_1]}\hat{B}^{[i_2]}\cdots\hat{A}^{[i_{k-1}]}\hat{B}^{[i_k]}|L\rangle|i_1\cdots i_k\rangle, \tag{6.36}$$

where

$$\hat{A}^{[0]} = |+\rangle\langle 0|, \quad \hat{A}^{[1]} = |-\rangle\langle 1|, \tag{6.37}$$

$$\hat{B}^{[0]} = |1\rangle\langle 0|, \quad \hat{B}^{[1]} = |0\rangle\langle 1|, \tag{6.38}$$

$$|L\rangle = |+\rangle, \qquad |R\rangle = \sqrt{2}|0\rangle. \tag{6.39}$$

Here, each atom is labelled from 1 to k, and the correlation matrices $\hat{A}^{[0/1]}$ and $\hat{B}^{[0/1]}$ are associated with odd and even atoms, respectively. Equivalently, it can be written as

$$|\psi_C\rangle = \sum_{\bar{i}_1 \ldots \bar{i}_N = 0}^{1} \langle R|\hat{C}^{[\bar{i}_1]}\cdots\hat{C}^{[\bar{i}_N]}|L\rangle|\bar{i}_1\cdots\bar{i}_N\rangle, \tag{6.40}$$

where

$$\begin{aligned} \hat{C}^{[\bar{0}]} &= \hat{A}^{[1]}\hat{B}^{[0]} = |-\rangle\langle 0| \\ \hat{C}^{[\bar{1}]} &= \hat{A}^{[0]}\hat{B}^{[1]} = |+\rangle\langle 1|, \\ |\bar{0}\rangle &= |10\rangle,\ |\bar{1}\rangle = |01\rangle. \end{aligned} \tag{6.41}$$

In this representation, each site is labelled from 1 to N and the correlation matrix $\hat{C}^{[\bar{0}/\bar{1}]}$ is associated with a pair of atoms. The measurement of odd and even atoms in the X-eigenbasis $\mathcal{B}_X = \{|\pm\rangle = (|0\rangle \pm |1\rangle)/\sqrt{2}\}$ on the state (6.36) projects the auxiliary matrix associated with the measured atom onto the eigenstate $(|0\rangle + (-1)^s|1\rangle)/\sqrt{2}$ depending on the measurement outcome s (see Eq. (6.70) in Sec. 6.10). In the graphical notation, this implements the operations

$$\longrightarrow\boxed{A[X]}\longrightarrow \quad \propto \hat{X}^s\hat{H}, \tag{6.42}$$

$$\longrightarrow\boxed{B[X]}\longrightarrow \quad \propto \hat{X}\hat{Z}^s, \tag{6.43}$$

for odd and even atoms, respectively. Here, the operator $\hat{H}$ is the Hadamard gate and $\hat{X}$ the Pauli-X matrix [26]. Similarly, measurements in the ϕ-eigenbasis $\mathcal{B}_\phi = \{(|0\rangle \pm e^{i\phi}|1\rangle)/\sqrt{2}\}$ yield

$$\longrightarrow\boxed{A[\phi]}\longrightarrow \quad \propto \hat{X}^s\hat{H}\hat{S}(\phi), \tag{6.44}$$

$$\longrightarrow\boxed{B[\phi]}\longrightarrow \quad \propto \hat{X}\hat{Z}^s\hat{S}(\phi), \tag{6.45}$$

where $\hat{S}(\phi) = \mathrm{diag}(1, e^{i\phi})$ in the usual computational basis. Also, we find that since the measurement of the ith and $(i+1)$th atoms (i odd) in the Bell basis has only two possible outcomes, we have

$$\longrightarrow\boxed{C[\bar{X}]}\longrightarrow \quad \propto \hat{Z}\hat{X}^s\hat{H}, \tag{6.46}$$

$$\longrightarrow\boxed{C[\bar{\phi}]}\longrightarrow \quad \propto \hat{Z}\hat{X}^s\hat{H}\hat{S}(\phi), \tag{6.47}$$

where the measurement eigenbases are given by $\mathcal{B}_{\bar{X}} = \{(|\bar{0}\rangle \pm |\bar{1}\rangle)/\sqrt{2}\}$ and $\mathcal{B}_{\bar{\phi}} = \{(|\bar{0}\rangle \pm e^{i\phi}|\bar{1}\rangle)/\sqrt{2}\}$, respectively. Since any single-qubit gate can be decomposed into Euler angles, i.e.

$$\hat{U}_{\mathrm{rot}}(\zeta, \eta, \xi) = \hat{S}(\zeta)\hat{H}\hat{S}(\eta)\hat{H}\hat{S}(\xi), \tag{6.48}$$

the application of one of the following sequence of measurements

$$\longrightarrow\boxed{\hat{B}[X_1]}\longrightarrow\boxed{A[\phi_2]}\longrightarrow\boxed{B[\phi_3]}\longrightarrow\boxed{A[X_4]}\longrightarrow\boxed{B[\phi_5]}\longrightarrow\boxed{A[X_6]}\longrightarrow \;, \tag{6.49}$$

$$\longrightarrow\boxed{C[\bar{X}_1]}\longrightarrow\boxed{C[\bar{\phi}_2]}\longrightarrow\boxed{C[\bar{\phi}_3]}\longrightarrow\boxed{C[\bar{\phi}_4]}\longrightarrow \tag{6.50}$$

on the state (6.36) realize arbitrary qubit gates, up to a known by-product operator $\hat{U}_\Sigma$. For instance, applying the measurement sequence (6.49) with measurement outcomes $\mathrm{s} = (1, 0, 0, 0, 1, 1)$, where s_i denotes the outcome of X_i or ϕ_i, implements the operation $\hat{U}_\Sigma\hat{U}_{\mathrm{rot}}(\phi_2, \phi_3, \phi_5)$ with $\hat{U}_\Sigma = \hat{H}\hat{Z}\hat{X}$ on the state of the correlation space. Similarly, the measurement sequence (6.50) with outcomes $\mathrm{s} = (0, 0, 1, 0)$ implements the operation

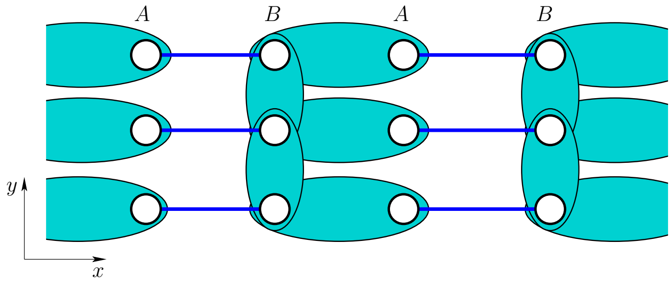

Fig. 6.6: Starting with 1D system (x–direction) in the state (6.36), a 2D state useful for MBQC is obtained by applying $\hat{C}_Z$ gates between even subsites (denoted by the letter B) in the y–direction.

$\hat{U}_\Sigma\hat{U}_{\rm rot}(\phi_2, \phi_3, \phi_4)$ with $\hat{U}_\Sigma = \hat{Z}\hat{X}\hat{Z}$. Although both measurement sequences (6.49) and (6.50) preserve the system's immunity to collective dephasing, fewer measurements are required using the sequence (6.49). The state of the correlation space can be read-out using a scheme described in Sec. 6.10.

Superlattice manipulations can also be used to engineer 2D systems. In the remainder of this section, we will consider the MPR of the 2D state $|\psi_{2D}\rangle$ resulting from the coupling of 1D systems in the state (6.36) via the application of a $\hat{C}_Z$ gate between *even* subsites[4] in the y–direction (see Fig. 6.6). The MPR of this state is given by

$$\begin{array}{c} u\uparrow \\ \xrightarrow{r}\boxed{C^{[0]}}\xrightarrow{l} \\ d\uparrow \end{array} = |-\rangle_r\langle 0|_l \otimes |+\rangle_u\langle 0|_d, \tag{6.51}$$

$$\begin{array}{c} u\uparrow \\ \xrightarrow{r}\boxed{C^{[1]}}\xrightarrow{l} \\ d\uparrow \end{array} = |+\rangle_r\langle 1|_l \otimes |-\rangle_u\langle 1|_d. \tag{6.52}$$

Also, the expansion coefficients of $|\psi_{2D}\rangle$ are represented by

$$\langle \bar{i}_{1,1}\dots\bar{i}_{2,2}|\psi_{2D}\rangle = \begin{array}{ccccccc} & & \boxed{U} & & \boxed{U} & & \\ & & \uparrow & & \uparrow & & \\ \boxed{L} & \rightarrow & \boxed{C^{[\bar{i}_{1,1}]}} & \rightarrow & \boxed{C^{[\bar{i}_{1,2}]}} & \rightarrow & \boxed{R} \\ & & \uparrow & & \uparrow & & \\ \boxed{L} & \rightarrow & \boxed{C^{[\bar{i}_{2,1}]}} & \rightarrow & \boxed{C^{[\bar{i}_{2,2}]}} & \rightarrow & \boxed{R} \\ & & \uparrow & & \uparrow & & \\ & & \boxed{D} & & \boxed{D} & & \end{array} \tag{6.53}$$

where $|U\rangle = |0\rangle$ and $|D\rangle = |+\rangle$.

[4] See e.g. Refs. [63, 66] for relevant 2D superlattice setups

This state is formally similar to a cluster state where qubits are encoded on two atoms and the $|+\rangle$ state corresponds to the Bell state (6.13). Although the application of the $\hat{C}_Z$ gate between *sites* in the y–direction implements the same operation between *encoded qubits*, it corresponds to a *different* operation between encoded qubits in the x–direction. Therefore, it is not possible to execute algorithms designed for cluster states using the state $|\psi_{2D}\rangle$ as a resource by simply interchanging, e.g. X measurements with Bell-pair measurements $\bar{X}$.

In the remainder of this section, we will show that $|\psi_{2D}\rangle$ constitute a universal resource for MBQC by presenting how to control information flows through the lattice, and by providing a measurement network that implements an entangling two-qubit gate.

Since the tensors of Eqs. (6.51) and (6.52) factor, they can be represented graphically by

$$\begin{array}{c} u\uparrow \\ \xrightarrow{r}\boxed{C^{[0]}}\xrightarrow{l} \\ d\uparrow \end{array} \quad = \quad \begin{array}{ccc} & u\,| & \\ & \boxed{+} & \\ \overset{l}{-}\boxed{0} & & \boxed{-}\overset{r}{-} \\ & \boxed{0} & \\ & d\,| & \end{array} \; . \tag{6.54}$$

Using this representation and Eqs. (6.51) and (6.52), we find that

$$\begin{array}{c} \boxed{C[\bar{Z}_1]} \\ \uparrow \\ \rightarrow\boxed{C[\bar{X}_2]}\rightarrow \\ \uparrow \\ \boxed{C[\bar{Z}_3]} \end{array} \quad \propto \quad \hat{X}\hat{Z}^{s_1+s_2+s_3}\hat{H}. \tag{6.55}$$

Thus, measurements in the basis $\mathcal{B}_{\bar{X}}$ cause the information to flow from left to right, and measurements of the vertically adjacent sites in the $\mathcal{B}_{\bar{Z}}$ basis shields the information from the rest of the lattice [131]. Since we can isolate horizontal lines, they can be used as logical qubits.

An entangling two-qubit gate between two horizontal lines is realized as follows. Consider the following measurement network [131]

$$
\begin{tikzcd}
 \arrow[r] & \boxed{C[\overline{X}_5]} \arrow[r] & {} \\
\boxed{C[\overline{Z}_3]} \arrow[r] & \boxed{C[\overline{Y}_2]} \arrow[u] \arrow[r] & \boxed{C[\overline{Z}_4]} \\
\boxed{|c\rangle} \arrow[r] & \boxed{C[\overline{X}_1]} \arrow[u] \arrow[r] & {}
\end{tikzcd}, \tag{6.56}
$$

where the middle site is measured in the basis $\mathcal{B}_{\overline{Y}} = \{(|\overline{0}\rangle \pm \mathrm{i}|\overline{1}\rangle)/\sqrt{2}\}$ and $c \in \{0, 1\}$. The lower part of the network reduces to

$$
\begin{tikzcd}
 & {} \\
\boxed{|c\rangle} \arrow[r] & \boxed{C[\overline{X}_1]} \arrow[u] \arrow[r] & {}
\end{tikzcd}
\quad \propto \quad
\begin{tikzcd}
{} \\
\boxed{Z^c|+\rangle} \arrow[u] \\
\boxed{(-1)^{s_1} XH|c\rangle} \arrow[r] & {}
\end{tikzcd} . \tag{6.57}
$$

Plugging (6.57) into the middle line yields

$$
\begin{tikzcd}
 & {} & \\
\boxed{C[\overline{Z}_3]} \arrow[r] & \boxed{C[\overline{Y}_2]} \arrow[u] \arrow[r] & \boxed{C[\overline{Z}_4]} \\
 & \boxed{Z^c|+\rangle} \arrow[u] &
\end{tikzcd}
\quad \propto \quad
\begin{tikzcd}
{} \\
\boxed{HZ^{s_2+s_3+c+1}[(-1)^{s_4}|0\rangle + \mathrm{i}|1\rangle]} \arrow[u]
\end{tikzcd} . \tag{6.58}
$$

Finally, plugging (6.58) into the upper of the network gives

$$
\begin{tikzcd}
{} \arrow[r] & \boxed{C[\overline{X}_5]} \arrow[r] & {} \\
 & \boxed{HZ^{s_2+s_3+c+1}[(-1)^{s_4}|0\rangle + \mathrm{i}|1\rangle]} \arrow[u] &
\end{tikzcd}
\quad \propto \quad \hat{U}_\Sigma(-\mathrm{i}\hat{Z})^c \tag{6.59}
$$

where $\hat{U}_\Sigma = \mathrm{e}^{\mathrm{i}\frac{\pi}{4}}(\mathrm{i}\hat{X})^{s_4}\hat{H}\hat{X}\hat{S}(\frac{\pi}{2})^\dagger\hat{Z}^{s_5}(-\mathrm{i}\hat{Z})^{s_2+s_3+1}$. Thus, the measurement network (6.56) implements an entangling controlled-phase gate between the upper and lower horizontal lines up to a know by-product operator. Since arbitrary single-qubit gates can be applied on each horizontal lines independently, this completes the proof of universality. The way of dealing with by-product operators at the end of the measurement sequences does not differ from the usual MBQC scheme with cluster states (see e.g. [114]). Notice that since single and two-qubit gates are performed via the application of pairwise measurements, the system remains invariant to collective dephasing at any time during the execution of an algorithm.

6.9 Conclusion

We have analyzed the dynamics of a bosonic spinor condensate in a superlattice potential, and shown that a lattice with a Bell pair in every lattice site can be realized via the dynamical splitting of each site. We have proposed a scheme that allows the application of an entangling $\sqrt{\mathrm{SWAP}}$ gate between and inside Bell pairs. The successive application of this gate between and inside lattice sites was shown to create an entangled state with a tunable Schmidt rank that is resilient to collective dephasing noise; and a maximally entangled state which, as numerical evidence suggests, is locally equivalent to a GHZ state. Finally, we have presented a state that is obtained by connecting Bell pairs in two dimensions via an entangling phase gate, and shown that it constitutes a resource for MBQC formally similar to a Bell-encoded cluster state. We have provided measurement networks for implementing a two-qubit entangling gate as well as arbitrary local unitary operations. Our implementation has the advantage that it allows the execution of quantum algorithms while leaving the system unaffected by collective dephasing noise.

6.10 Appendices

The full Hamiltonian

Using the field operator (6.7), the single-particle terms of the Hamiltonian (6.2) in second quantized form are given by

$$\begin{aligned}\hat{H}_0 &= \hat{H}_K + \hat{H}_Z \\ &= \sum_{\sigma=-1,0,1} [V_a + \Delta E_{Z,\sigma}(B)]\, \hat{a}^\dagger_\sigma \hat{a}_\sigma + \sum_{\sigma=-1,0,1} [V_b + \Delta E_{Z,\sigma}(B)]\, \hat{b}^\dagger_\sigma \hat{b}_\sigma,\end{aligned} \tag{6.60}$$

where $V_\nu = \int \mathrm{d}\mathbf{r}\, w^*_\nu(\mathbf{r})\hat{h}_0\, w_\nu(\mathbf{r})$. Assuming that the magnetic field is weak ($B < 200\,\mathrm{G}$), the Zeeman shift $\Delta E_{Z,\sigma}(B)$ is accurately approximated to the second order in B [13]

$$\Delta E_{Z,\sigma}(B) = \begin{cases} \frac{g\mu_B B}{4} - \frac{3(g\mu_B B)^2}{16\Delta E_{\mathrm{hf}}} & \text{if } \sigma = -1, \\ -\frac{(g\mu_B B)^2}{4\Delta E_{\mathrm{hf}}} & \text{if } \sigma = 0, \\ -\frac{g\mu_B B}{4} - \frac{3(g\mu_B B)^2}{16\Delta E_{\mathrm{hf}}} & \text{if } \sigma = 1, \end{cases} \tag{6.61}$$

where g is the gyromagnetic factor, ΔE_{hf} is the hyperfine splitting energy, and μ_B is the Bohr magneton.

In the low-energy limit, atomic interactions are well approximated by s-wave scattering, with the scattering length depending on the spin state of the colliding atoms. At ultracold temperatures, two colliding atoms in the lower hyperfine level f_{low} will remain in the same multiplet, since the interaction process is not energetic enough to promote either atom to a higher hyperfine level f_{high} [106]. Also, since alkalis have only two hyperfine multiplets, the conservation of the total angular momentum by the scattering process implies that interatomic interactions conserve the hyperfine spin f_1 and f_2 of the individual atoms. Thus, the interaction between two particles located at positions $\mathbf{r}_1$ and $\mathbf{r}_2$ is given by [106, 117, 133]

$$\hat{V}_{\mathrm{int}}(\mathbf{r}_1 - \mathbf{r}_2) = \frac{4\pi\hbar^2}{M}\delta(\mathbf{r}_1 - \mathbf{r}_2) \sum_{F=0,2} a_F \hat{\mathscr{P}}_F, \tag{6.62}$$

where $F = f_1 + f_2$ is the total angular momentum of the scattered pair, $\hat{\mathscr{P}}_F$ is the projection operator for the total angular momentum F, and a_F is the s-wave scattering length of the channel associated with the total angular momentum F. The operator $\hat{\mathscr{P}}_F$ is given by [133]

$$\hat{\mathscr{P}}_F = \sum_{m_F=-F}^{F} |F, m_F\rangle\langle F, m_F|, \tag{6.63}$$

where $|F, m_F\rangle$ is the state formed by two atoms with total angular momentum F and $m_F = m_1 + m_2$ with m_1 and m_2 the projection on the quantization axis of f_1 and f_2, respectively. The quantization axis is defined by the direction of the magnetic field present in the system. Boson statistics require the state $|F, m_F\rangle$ to be invariant under particle exchange, and hence only the terms corresponding to values of $F = \{0, 2\}$ appear in the sum of Eq. (6.62). Using the relation $\hat{\mathbf{f}}_1 \cdot \hat{\mathbf{f}}_2 = \hat{\mathscr{P}}_2 - 2\hat{\mathscr{P}}_0$, where $\hat{\mathbf{f}}_i = (\hat{f}^i_x, \hat{f}^i_y, \hat{f}^i_z)$ is the total angular momentum operator of the particle i, the interaction operator can be re-written as [106, 49]

$$\hat{V}_{\text{int}}(\mathbf{r}_1 - \mathbf{r}_2) = \delta(\mathbf{r}_1 - \mathbf{r}_2)\left(c_0 + c_2\hat{\mathbf{f}}_1 \cdot \hat{\mathbf{f}}_2\right). \tag{6.64}$$

From Eq. (6.64) we see that interactions conserve the quantum number m_F [13].

Using the field operator (6.7), the interaction term in second quantized form reads

$$\begin{aligned}\hat{H}_{\text{int}} =& \frac{1}{2}\int\int \mathrm{d}\mathbf{r}_1 \mathrm{d}\mathbf{r}_2\, \delta(\mathbf{r}_1 - \mathbf{r}_2) \times \\ & c_0 \,:\left(\hat{\mathbf{\Psi}}^\dagger(\mathbf{r}_1) \cdot \hat{\mathbf{\Psi}}(\mathbf{r}_1)\right)\left(\hat{\mathbf{\Psi}}^\dagger(\mathbf{r}_2) \cdot \hat{\mathbf{\Psi}}(\mathbf{r}_2)\right): \\ & + c_2 \sum_{\ell=x,y,z} :\left(\hat{\mathbf{\Psi}}^\dagger(\mathbf{r}_1)\hat{f}^1_\ell \hat{\mathbf{\Psi}}(\mathbf{r}_1)\right)\left(\hat{\mathbf{\Psi}}^\dagger(\mathbf{r}_2)\hat{f}^2_\ell \hat{\mathbf{\Psi}}(\mathbf{r}_2)\right):,\end{aligned} \tag{6.65}$$

where $:\hat{\circ}:$ represents the operator $\hat{\circ}$ in normal ordering, $\hat{\mathbf{\Psi}}(\mathbf{r}) = (\hat{\Psi}_{-1}(\mathbf{r}), \hat{\Psi}_0(\mathbf{r}), \hat{\Psi}_1(\mathbf{r}))$ and the matrices $\hat{f}_\ell$ are given by [118]

$$\hat{f}^i_x = \frac{1}{\sqrt{2}}\begin{pmatrix} 0 & 1 & 0 \\ 1 & 0 & 1 \\ 0 & 1 & 0 \end{pmatrix},\ \hat{f}^i_y = \frac{1}{\sqrt{2}\mathrm{i}}\begin{pmatrix} 0 & 1 & 0 \\ -1 & 0 & 1 \\ 0 & -1 & 0 \end{pmatrix},\ \hat{f}^i_z = \begin{pmatrix} 1 & 0 & 0 \\ 0 & 0 & 0 \\ 0 & 0 & -1 \end{pmatrix}. \tag{6.66}$$

The Hamiltonian given in (6.5) is a compact form of (6.65). In its expanded form, Eq. (6.65) reads [49]

$$\begin{aligned}\hat{H}_{\text{int}} = \frac{1}{2}\int d\mathbf{r}\times \\ &\Big\{(c_0+c_2)\left[\hat{\Psi}_1^\dagger(\mathbf{r})\hat{\Psi}_1^\dagger(\mathbf{r})\hat{\Psi}_1(\mathbf{r})\hat{\Psi}_1(\mathbf{r}) + \hat{\Psi}_{-1}^\dagger(\mathbf{r})\hat{\Psi}_{-1}^\dagger(\mathbf{r})\hat{\Psi}_{-1}(\mathbf{r})\hat{\Psi}_{-1}(\mathbf{r})\right] \\ &+ 2(c_0+c_2)\left[\hat{\Psi}_1^\dagger(\mathbf{r})\hat{\Psi}_0^\dagger(\mathbf{r})\hat{\Psi}_1(\mathbf{r})\hat{\Psi}_0(\mathbf{r}) + \hat{\Psi}_{-1}^\dagger(\mathbf{r})\hat{\Psi}_0^\dagger(\mathbf{r})\hat{\Psi}_{-1}(\mathbf{r})\hat{\Psi}_0(\mathbf{r})\right] \\ &+ 2c_2\left[\hat{\Psi}_0^\dagger(\mathbf{r})\hat{\Psi}_0^\dagger(\mathbf{r})\hat{\Psi}_1(\mathbf{r})\hat{\Psi}_{-1}(\mathbf{r}) + \hat{\Psi}_1^\dagger(\mathbf{r})\hat{\Psi}_{-1}^\dagger(\mathbf{r})\hat{\Psi}_0(\mathbf{r})\hat{\Psi}_0(\mathbf{r})\right] \\ &+ c_0\left[\hat{\Psi}_0^\dagger(\mathbf{r})\hat{\Psi}_0^\dagger(\mathbf{r})\hat{\Psi}_0(\mathbf{r})\hat{\Psi}_0(\mathbf{r})\right] \\ &+ 2(c_0-c_2)\left[\hat{\Psi}_1^\dagger(\mathbf{r})\hat{\Psi}_{-1}^\dagger(\mathbf{r})\hat{\Psi}_1(\mathbf{r})\hat{\Psi}_{-1}(\mathbf{r})\right]\Big\}. \qquad (6.67)\end{aligned}$$

The interaction Hamiltonian (6.67) can be expressed in terms of $\hat{a}_\sigma^\dagger$ and $\hat{b}_\sigma^\dagger$ operators using the relation

$$\begin{aligned}\frac{1}{2}\int d\mathbf{r}\,\hat{\Psi}_\sigma^\dagger(\mathbf{r})\hat{\Psi}_\gamma^\dagger(\mathbf{r})\hat{\Psi}_{\sigma'}(\mathbf{r})\hat{\Psi}_{\gamma'}(\mathbf{r}) &= \frac{U_{aa}}{2}\left(\hat{a}_\sigma^\dagger\hat{a}_\gamma^\dagger\hat{a}_{\sigma'}\hat{a}_{\gamma'}\right) + \frac{U_{bb}}{2}\left(\hat{b}_\sigma^\dagger\hat{b}_\gamma^\dagger\hat{b}_{\sigma'}\hat{b}_{\gamma'}\right) + \\ &\frac{U_{ab}}{2}\left(\hat{a}_\sigma^\dagger\hat{a}_\gamma^\dagger\hat{b}_{\sigma'}\hat{b}_{\gamma'} + \hat{b}_\sigma^\dagger\hat{b}_\gamma^\dagger\hat{a}_{\sigma'}\hat{a}_{\gamma'}\right) + \frac{U_{ab}}{2}\left(\hat{a}_\sigma^\dagger\hat{b}_\gamma^\dagger + \hat{b}_\sigma^\dagger\hat{a}_\gamma^\dagger\right)\left(\hat{a}_{\sigma'}\hat{b}_{\gamma'} + \hat{b}_{\sigma'}\hat{a}_{\gamma'}\right), \qquad (6.68)\end{aligned}$$

where $U_{\nu\nu'} = \int d\mathbf{r}\,(|w_\nu(\mathbf{r})||w_{\nu'}(\mathbf{r})|)^2$ and $\sigma, \gamma = -1, 0, +1$.

Measurement-based quantum computations and MPSs

General idea

In this section, we present the general idea developed in Ref. [132]. From Eq. (6.35), one can see that if the i_k site in the computational basis and the outcome s_k is obtained, then the state $|L\rangle$ of the auxiliary system becomes

$$|L\rangle' = \hat{\Lambda}_k^{[s_k]}|L\rangle. \qquad (6.69)$$

Thus, measurements change the state $|L\rangle$ of the auxiliary system. Similarly, if the measurement of a local observable at site k yields an outcome corresponding to the observable's eigenvector $|\phi_k\rangle$, then the matrix $\hat{\Lambda}_k^{[i_k]}$ transforms into

$$\hat{\Lambda}[\phi]_k = \langle\phi_k|0\rangle\hat{\Lambda}_k^{[0]} + \langle\phi_k|1\rangle\hat{\Lambda}_k^{[1]}, \qquad (6.70)$$

and the vector of the auxiliary system becomes

$$|L\rangle' = \hat{\Lambda}[\phi]_k|L\rangle. \tag{6.71}$$

From this point of view, a measurement on some physical site change the correlation properties between this site and the rest of the chain, i.e. it performs an operation on the auxiliary system state $|L\rangle$, which we will sometimes refer to as the state of the correlation space.

Graphical notation

In order to deal with the MPS of higher-dimensional states, the graphical notation introduced in Ref. [132] is very helpful. In this notation, tensors are represented by boxes, and their indices by edges. Vectors and matrices are thus symbolized by

$$|L\rangle = \boxed{L}\!\rightarrow\ , \tag{6.72}$$

$$\langle R| = \rightarrow\!\boxed{R^\dagger}\ , \tag{6.73}$$

$$\hat{\Lambda}^{[i]} = \rightarrow\!\boxed{\Lambda^{[i]}}\!\rightarrow\ . \tag{6.74}$$

Consequently, vector and matrix operations can be represented graphically by

$$\langle R|L\rangle = \boxed{L}\!-\!\boxed{R}\ , \tag{6.75}$$

$$\hat{B}\hat{A} = \rightarrow\!\boxed{A}\!\rightarrow\!\boxed{B}\!\rightarrow\ , \tag{6.76}$$

$$\hat{B}\hat{A}|L\rangle = \boxed{L}\!\rightarrow\!\boxed{A}\!\rightarrow\!\boxed{B}\!\rightarrow\ . \tag{6.77}$$

Read-out scheme

In order to use the state of the correlation space to process quantum information, we must be able to read it out at the end of the computation. It turns out that in our case a measurement of the $(i-1)$th site in the computational basis corresponds to a measurement of the correlation system just after the ith site. To illustrate this fact, assume that just after the measurement of the ith site, the correlation system is in the state $|0\rangle$, that is

$$\boxed{L} \to \boxed{B[\phi_1]} \to \boxed{A[\phi_2]} \to \cdots \quad \boxed{B[\phi_i]} \to \quad = |0\rangle, \tag{6.78}$$

or

$$\boxed{L} \to \boxed{B[\phi_1]} \to \boxed{A[\phi_2]} \to \cdots \quad \boxed{A[\phi_i]} \to \quad = |0\rangle. \tag{6.79}$$

Thus, using Eqs. (6.37) and (6.38) we have

$$\boxed{|0\rangle} \to \boxed{A[1]} \to \; \propto |-\rangle\langle 1|0\rangle \;=\; 0, \tag{6.80}$$

$$\boxed{|0\rangle} \to \boxed{B[1]} \to \; \propto |0\rangle\langle 1|0\rangle \;=\; 0. \tag{6.81}$$

Hence, the probability of obtaining the result 1 for a measurement on the $(i-1)$th site is zero. Consequently, if the state of the correlation system is in state $|0\rangle$ after the ith site, then the $(i-1)$th physical site must also be in that state. Since

$$\boxed{|0\rangle} \to \boxed{C[1]} \to \quad \propto |+\rangle\langle 1|0\rangle = 0, \tag{6.82}$$

the same observation applies if one measures the $(i-2)$th and $(i-1)$th sites (i odd) in the basis $\mathcal{B}_{\bar{Z}} = \{|\bar{0}\rangle, |\bar{1}\rangle\}$. Therefore, as a similar argument applies if the state of the correlation system is in the state $|1\rangle$ after the ith site, the description of the read-out scheme is complete.

Chapter 7

From rotating ring lattices to the fractional quantum Hall effect

In this chapter, we study ultracold bosons on a two-dimensional lattice in the presence of an effective magnetic field and point out a couple of features this system has in common with the rotating ring lattices we discussed in Chapter 4. Starting from the degenerate single-particle spectrum known as the Hofstadter butterfly, we find that interactions lift the huge degeneracy of the non-interacting system apart from topological degeneracies. Parallel to our previous work, we then derive an effective many-body Hamiltonian and show that weak random potentials can lead to a coupling between the degenerate ground states which decreases exponentially with increasing number of particles. For this reason fractional quantum Hall systems have been proposed as topologically-protected quantum memories.

7.1 Introduction

The integer and fractional quantum Hall effects are among the most intriguing phenomena of condensed-matter physics. Von Kitzling *et al.* [134] discovered that at large magnetic field and low temperature the Hall resistance R_H of a two-dimensional electron gas in a semiconductor heterostucture shows numerous plateaus as a function of the magnetic field B. On each plateau, the Hall resistance, defined as $R_H = V_H/I$ with the Hall voltage V_H and the current I, is given by h/ne^2 with n integer. Close to the plateaus, the longitudinal resistance, defined as $R_L = V_L/I$ with the voltage drop V_L in the direction of the current I, depends exponentially on the temperature T, $R_L \propto e^{-\Delta/2k_BT}$. This integer quantum Hall effect (IQHE) came as a great surprise, but it can be explained by the fact that the ground state at filling factor $\nu = \rho hc/eB = n$ and density ρ consists of n fully-occupied Landau levels and therefore shows a energy gap Δ to excitations.

The next twist to the story were the findings by Tsui *et al.* [135] who observed plateaus where the resistance is h/fe^2 with f a rational fraction and which occurred at magnetic fields corresponding to a fractional filling of the lowest Landau level $\nu = f$. This fractional quantum Hall effect (FQHE) cannot be explained in a single-particle picture, but it is a strong correlation effect brought along by interactions between the electrons in a partially-filled Laudau level. This is a very challenging problem, since the system is highly degenerate in the absence of interactions and the interactions set the only energy scale, so that there is no small parameter to expand in. Apart from exact diagonalization and the effective theory of composite fermions [136], much of the present understanding relies on trial wave functions, e.g. at the filling fractions $\nu = 1/m$, with m even for bosons and m odd for fermions, those first written down by Laughlin [137]

$$\Psi_{1/m} = \prod_{j<k} \left(z_j - z_k\right)^m e^{-\sum_i |z_i|^2/4}. \tag{7.1}$$

In this expression, $z_j = x_j + iy_j$ are the two-dimensional coordinates of the j-th particle and the magnetic length $l_B = \sqrt{\hbar c/eB}$ is the unit of length. The Laughlin state $\Psi_{1/m}$ is known to be the exact ground state of the many-body problem at filling factor $\nu = 1/m$ for short-ranged interactions [138].

Larmor's theorem tells us that rotation has a similar effect on neutral atoms as a uniform magnetic field on charged particles. It is therefore natural to ask whether the fractional quantum Hall effect can also be realized in rotating Bose gases [139, 140, 141]. However, achieving this goal experimentally has been difficult [142], because it requires the rotation frequency to closely match the trapping frequency. As an alternative, schemes for optical lattices with effective magnetic fields have been put forward [143, 144]. Since the lattice enhances the effects of the interactions, this approach should also lead to larger energy gaps compared to the harmonically trapped gas. This could stabilize the strongly-correlated ground state against external noise and thermal fluctuations. Several aspects of this system have been addressed in the literature, e.g. the linear response to external perturbations [88, 145, 146] and the topological order in the ground-state manifold via Chern number calculations [147, 148].

In this chapter, we study ultracold bosons on a 2D lattice in the presence of an effective magnetic field and point out features this system has in common with ultracold bosons in 1D rotating ring lattices. We first discuss the single-particle problem whose energy spectrum is known as the Hofstadter butterfly [149]. We present numerical results for interacting bosons on a lattice showing that interactions lift the huge degeneracy of the non-interacting system apart from topological degeneracies [147]. Parallel to our previous work, we then derive an effective many-body Hamiltonian [150, 151]. We discuss the exactly-solvable Tao-Thouless limit of a thin cylinder [152, 153] and point out its relationship with the Laughlin wave function [154, 151, 153, 155]. We also explain the degeneracy of the many-body spectrum using the magnetic translation group [156]. Finally, we show that a weak random potential can lift the topological degeneracies. The coupling between the degenerate ground states however decreases exponentially with increasing number of particles [157]. For this reason fractional quantum Hall systems have been proposed as topologically-protected quantum memories [158].

7.2 Model

We consider N ultracold bosons on a $N_x \times N_y$ square lattice described by a two-dimensional Bose-Hubbard Hamiltonian [18]. The presence of an effective uniform magnetic field perpendicular to the lattice in the $x-y$ plane, $\mathbf{B} = B\mathbf{e}_z$, leads, similar to the case of the rotating ring lattice in Chapter 4, to a Peierls phase factor [89] in the hopping term. The Hamiltonian has the form

$$\hat{H} = -J \sum_{\langle i,j \rangle} \left(\hat{a}_i^\dagger \hat{a}_j \exp\left(\frac{2\pi i}{\Phi_0} \int_{x_i}^{x_j} \mathbf{A} \cdot d\mathbf{x} \right) + H.c. \right) + \frac{U}{2} \sum_j \hat{n}_j (\hat{n}_j - 1). \tag{7.2}$$

In the Landau gauge, $\mathbf{A} = -By\mathbf{e}_x$, it reads [143, 144, 88, 147]

$$\hat{H} = -J \sum_{x,y} \left(\hat{a}^\dagger_{x+1,y} \hat{a}_{x,y} \mathrm{e}^{-\mathrm{i}2\pi\alpha y} + \hat{a}^\dagger_{x,y+1} \hat{a}_{x,y} + H.c. \right) + \frac{U}{2} \sum_{x,y} \hat{n}_{x,y} (\hat{n}_{x,y} - 1) \tag{7.3}$$

where α is the magnetic flux per plaquette in units of the flux quantum Φ_0, $\hat{a}_{x,y}$ annihilates a particle on the site x, y with $x \in \{1, \ldots, N_x\}$ and $y \in \{1, \ldots, N_y\}$, and all other notations are standard [18].

While the above Hamiltonian appears naturally for charged particles in a magnetic field, the realization of a system described by such a Hamiltonian with neutral atoms is much less straightforward. There are a couple of theoretical proposals in the literature to obtain such a Peierls phase factor [89], e.g. by using Raman transitions for the optical lattice setup [143], by alternating the tunneling and adding a quadratic superlattice potential [144] or by simply rotating the lattice [147].

In case of a homogeneous system it is customary to impose periodic boundary conditions (PBC). In the presence of a magnetic field, this turns out to be a non-trivial task. PBC, i.e. $\psi(x+N_x, y) = \psi(x, y)$ and $\psi(x, y+N_y) = \psi(x, y)$ for the single-particle wave function $\psi(x, y)$, are eigenvalue equations for the translation operators $\hat{t}_{N_x \mathbf{e}_x}$ and $\hat{t}_{N_y \mathbf{e}_y}$ with eigenvalue one. The translation operator $\hat{t}_{\mathbf{R}} = \mathrm{e}^{\mathrm{i}\mathbf{R}\cdot\hat{\mathbf{p}}}$ and the Hamiltonian for a single particle in a magnetic field do not commute for arbitrary $\mathbf{R}$, so that PBC cannot be imposed consistently. The magnetic translation operator (MTO) $\hat{\mathcal{T}}_{\mathbf{R}}$ is defined as an ordinary translation operator followed by a gauge transformation, so that the MTO commutes with the single-particle Hamiltonian. In the Landau gauge, the MTO has the form $\hat{\mathcal{T}}_{(X,Y)} = \mathrm{e}^{-\mathrm{i}2\pi\alpha Y x}\, \hat{T}_{(X,Y)}$. However, MTOs do generally not commute with each other. In order to impose consistent boundary conditions, we have to make sure that the two MTOs defining the boundary conditions commute, i.e. we require $\hat{\mathcal{T}}_{(N_x,0)} \hat{\mathcal{T}}_{(0,N_y)} = \mathrm{e}^{-\mathrm{i}2\pi\alpha N_x N_y} \hat{\mathcal{T}}_{(0,N_y)} \hat{\mathcal{T}}_{(N_x,0)} = \hat{\mathcal{T}}_{(0,N_y)} \hat{\mathcal{T}}_{(N_x,0)}$, i.e. the number of flux quanta penetrating the lattice $N_\Phi = \alpha N_x N_y = B L_x L_y / \Phi_0$ has to be an integer.

7.3 Single-particle problem

In this section, we discuss the physics of a single particle confined to a two-dimensional plane in the presence of an effective uniform magnetic field perpendicular to this plane. We first study this problem in the absence of a lattice potential which leads to the well-known Landau-level quantization. We then consider the tight-binding limit whose energy spectrum is the famous Hofstadter butterfly [149].

7.3.1 Landau levels in the absence of a lattice potential

The Hamiltonian for a particle with mass m and charge q moving in two dimensions in the presence of a vector potential $\mathbf{A}$ is given by

$$\hat{H} = \frac{1}{2m}\left(\hat{\mathbf{p}} - \frac{q}{c}\mathbf{A}\right)^2 . \tag{7.4}$$

For a uniform magnetic field, $\nabla \times \mathbf{A} = B\mathbf{e}_z$, the vector potential is a linear function of the spatial coordinates, so that $\hat{H}$ is a generalized two-dimensional harmonic oscillator which can be solved exactly.

In the Landau gauge, $\mathbf{A} = B(-y, 0, 0)$, the vector potential does not depend on x and therefore commutes with p_x. The momentum k_x is thus a good quantum number. Defining the magnetic length as $l_B = \sqrt{\hbar c/eB}$ and the cyclotron energy as $\omega_c = eB/mc$ the energy eigenvalues

$$E_n = \left(n + \frac{1}{2}\right)\hbar\omega_c \tag{7.5}$$

with $n = 0, 1, \ldots$ are called Landau levels and the associated eigenfunctions are

$$\eta_{n,k_x} = \frac{1}{\sqrt{\sqrt{\pi}2^n n!}} e^{ik_x x} \exp\left[-\frac{1}{2}\left(\frac{y}{l_B} - l_B k_x\right)^2\right] H_n\left(\frac{y}{l_B} - l_B k_x\right) \tag{7.6}$$

where H_n are Hermite polynomials.

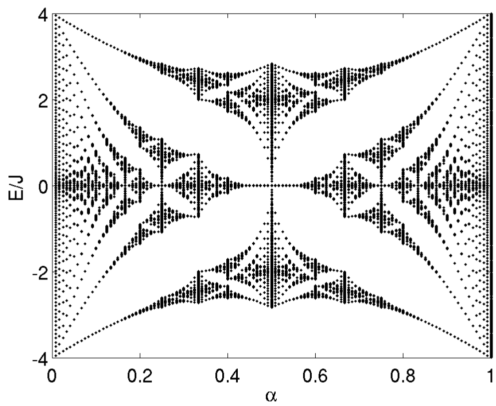

Fig. 7.1: Spectrum of a single particle on a $N_x \times N_y = 120 \times 120$ lattice as a function of the flux quanta per plaquette α known as the Hofstadter butterfly [149].

We note that the energy does not depend on k_x, so that eigenstates with different k_x and the same n are degenerate, and that in the y-direction the ground-state wavefunctions are Gaussians of width l_B centered at $y = k_x l_B^2$. To count the degeneracy, we impose periodic boundary conditions in the x-direction $e^{ik_x(x+L_x)} = e^{ik_x x}$. The allowed values of k_x are $k_x = 2\pi n_x/L_x$ with n_x integer, so that the number of degenerate states in a given area $L_x L_y$ is $N_x = L_x L_y/2\pi l_B^2 = BL_x L_y/\Phi_0 = N_\Phi$ where N_Φ is the number of flux quanta.

7.3.2 Hofstadter butterfly in the tight-binding limit

In the tight-binding limit the single-particle wave function $\psi(x, y)$ obeys the Schrödinger equation with the Hamiltonian (7.3) and $U = 0$

$$-J\left(\psi(x-1, y)\mathrm{e}^{-\mathrm{i}2\pi\alpha y} + \psi(x+1, y)\mathrm{e}^{\mathrm{i}2\pi\alpha y} + \psi(x, y-1) + \psi(x, y+1)\right) = E\psi(x, y). \quad (7.7)$$

Making a plane wave ansatz along the x-direction, $\psi(x, y) = \mathrm{e}^{\mathrm{i}k_x x}u(y)$, this equation reduces to the one-dimensional *Harper equation* [159]

$$u(y-1) + u(y+1) + 2\cos(2\pi\alpha y - k_x)\, u(y) = Eu(y) \quad (7.8)$$

where the momentum k_x is quantized, i.e. $k_x = 2\pi s/N_x$ with $0 \le s \le N_x$ integer.

Since $\alpha = N_\Phi/N_xN_y$ is a rational number, i.e. $\alpha = p/q$ with p and q co-prime, the term $\cos(2\pi\alpha y)$ is q-periodic, so that there is a so-called magnetic supercell of size q. Consequentially, the first Bloch band with $M = N_xN_y$ states breaks into q bands with $M/q = N_\Phi/p$ degenerate states [149]. In the continuum limit, i.e. $\alpha \to 0$, p subbands become degenerate and the N_Φ-fold degeneracy of the Landau levels is recovered. The energy spectrum as a function of the flux per plaquette α is the famous *Hofstadter butterfly* [149], which is shown in Fig. 7.1. We note that the Harper equation also appears in studies of a single particle in one-dimensional quasi-periodic lattices [160].

7.4 Many-particle problem

In this section, we first present numerical results for the model Hamiltonian (7.3) showing that interactions lift the huge degeneracy of the non-interacting system [147]. We then derive an effective many-body Hamiltonian [150, 151], discuss the exactly-solvable Tao-Thouless limit of a thin cylinder [152] and point out its relationship with the Laughlin wave function [154, 151, 153, 155]. Finally, we explain the degeneracy of the many-body spectrum using the magnetic translation group [156].

At fixed filling fraction $\nu = N/N_\Phi = 1/2$ the properties of the system with the model Hamiltonian (7.3) depend on the parameter $\alpha = n/\nu$ (which is proportional to the density $n = N/N_xN_y$) and the ratio between the on-site interaction and tunneling energy U/J. In the following, we will focus on the limit of a small flux per plaquette, i.e $\alpha < 0.25$, where the lattice potential does not have a dominant effect, i.e. we are in the continuum limit. In the upper part of Fig. 7.2, we plot the many-body spectrum for $N = 2$ atoms on a $N_x \times N_y = 4 \times 4$ lattice threaded by a total magnetic flux of $N_\Phi = 4$ flux quanta as a function of the ratio U/J. In the absence of interactions $U = 0$, the many-body ground state is highly degenerate. If the single-particle spectrum is N_{deg}-fold degenerate,

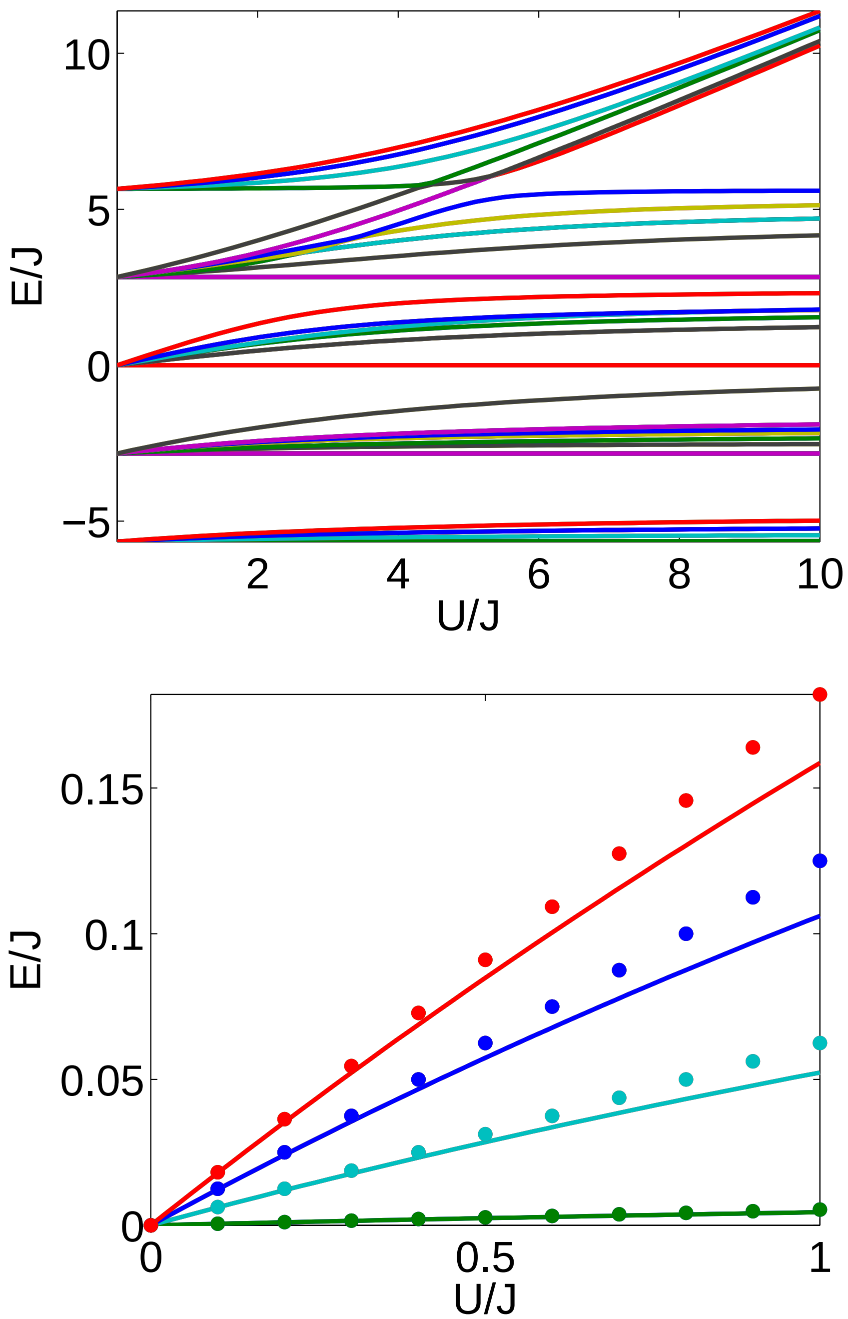

Fig. 7.2: Many-body spectrum for $N = 2$ atoms on a $N_x \times N_y = 4 \times 4$ lattice threaded by a total magnetic flux of $N_\Phi = 4$ flux quanta as a function of the on-site interaction U/J [147]. The bottom figure shows the spectrum as a function of U/J (solid line) and the spectrum of the effective Hamiltonian (points). [Help by Mohammad Hafezi is acknowledged.]

the degeneracy for the many-body system of N bosons is

$$\begin{pmatrix} N + N_{\text{deg}} - 1 \\ N_{\text{deg}} - 1 \end{pmatrix} = \frac{\left(N + N_{\text{deg}} - 1\right)!}{N!\left(N_{\text{deg}} - 1\right)!}. \tag{7.9}$$

The huge degeneracy of the non-interacting system is lifted by finite repulsive interactions, but all the states remain (at least) twice degenerate. We shall come back to this topological degeneracy further below. In the limit $U \ll J$ the energy differences are proportional to the on-site interaction U, while they become independent of U and proportional to the tunneling energy J in the hard-core limit $U \gg J$. In the continuum limit, $\alpha \to 0$, it has been shown that the two ground states have large overlap with the Laughlin wave functions on a torus [144, 147], which are known to be the exact ground states for short-ranged interactions in the absence of a lattice potential [138].

Parallel to our previous work, we now derive an effective many-body Hamiltonian. For small on-site interaction $U \ll J$, we can treat the on-site interaction in degenerate perturbation theory. To this end, we find a set of lowest-energy single-particle states and construct an effective Hamiltonian in the Fock basis of the degenerate subspace. In the bottom part of Fig. 7.2 we compare the spectrum of this effective Hamiltonian with that of the exact many-body Hamiltonian. We see that they agree very well for small interactions $U/J < 0.5$. Beyond this limit, the on-site interaction terms start mixing the different energy bands and the description by the effective Hamiltonian breaks down. In order to go beyond numerical results, we neglect the lattice potential and calculate the matrix elements of the interaction Hamiltonian in the lowest Landau level. Starting from the general many-body Hamiltonian for a contact interaction potential

$$\hat{H} = \int d\mathbf{x}\hat{\Phi}^{\dagger}(\mathbf{x})\left[\frac{\hbar^2}{2M}\left(\hat{\mathbf{p}} - \frac{q}{c}\mathbf{A}\right)^2\right]\hat{\Phi}(\mathbf{x}) + \frac{1}{2}\cdot\frac{4\pi a_s\hbar^2}{M}\int d\mathbf{x}\hat{\Phi}^{\dagger}(\mathbf{x})\hat{\Phi}^{\dagger}(\mathbf{x})\hat{\Phi}(\mathbf{x})\hat{\Phi}(\mathbf{x}), \tag{7.10}$$

we expand the particle operator as $\hat{\Phi}(\mathbf{x}) = \sum_{m=1}^{N_\Phi} \eta_{n=0,\,k_x=m}(\mathbf{x})\,\hat{a}_m$ where $\eta_{n=0,\,k_x=m}(\mathbf{x})$ are the wave functions (7.6) for the lowest Landau level on a cylinder with circumference L. They all have the same kinetic energy, so that we are left with the effective Hamiltonian

$$\hat{H}_{\text{eff}} = \frac{g\kappa}{2} \sum_{jkm} e^{-\kappa^2(k^2+m^2)/2} \, \hat{a}^\dagger_{j+k} \hat{a}^\dagger_{j+m} \hat{a}_{j+k+m} \hat{a}_j \tag{7.11}$$

where $g = V_0/(2\pi)^{3/2} l_B^2$, $V_0 = 4\pi a\hbar^2/M$ and $\kappa = 2\pi l_B/L$. The effective Hamiltonian contains two different contributions: the terms with $m = 0$ describe the repulsion between two particles k orbitals apart, whereas the others are the amplitudes for a correlated hopping process, in which two particles $k - m$ orbitals apart are transferred to orbitals $k + m$ apart while conserving the center-of-mass position at $(k + m)/2$. The ratio κ^{-1} is the effective range for the correlated tunneling processes [152, 150, 151].

In the so-called Tao-Thouless limit of a thin cylinder $L \to 0$, the effective range goes to zero $\kappa^{-1} \to 0$, and the on-site and nearest-neighbor interaction become the most important terms [152, 153]

$$\hat{H}_{\text{eff}} = \frac{g\kappa}{2} \sum_{j} \left(\hat{n}_j(\hat{n}_j - 1) + 4e^{-\kappa^2/2} \hat{n}_j \hat{n}_{j+1} \right) + \ldots . \tag{7.12}$$

In this limit, the effective Hamiltonian is diagonal in the Fock basis and thus exactly solvable. The energy is minimized for a regular occupation pattern in the single-particle basis of the lowest Landau level, i.e. at filling fraction $\nu = 1/2$ these are the two degenerate Tao-Thouless states $|10101010\ldots\rangle$ and $|01010101\ldots\rangle$ [152, 161].

As the circumference L is increased, the correlated hopping processes become more important and so-called squeezed states, e.g. $|100111001\rangle$ and $|10100200\rangle$, are mixed into the ground-state wave function. For the fermionic problem at odd denominator fractions, $\nu = 1/m$ with m odd, it has been shown that the Tao-Thouless states are adiabatically connected to the Laughlin states $\Psi_{1/m}$, i.e. there is no phase transition as the circumference L is increased [154, 151, 153]. For bosons at filling fraction $\nu = 1/m$ with m even, the Laughlin wave function $\Psi_{1/m}$ (7.1) is a so-called Jack polynomial whose dominant occupation-number configuration is the corresponding Tao-Thouless configuration [155].

Finally, we would like to give an argument for the degeneracy of the many-body spectrum by considering the magnetic translations on a torus [156, 157]. In the absence of a lattice potential, the magnetic translation operator has the form $\hat{\mathcal{T}}_{(X,Y)} = \mathrm{e}^{-\mathrm{i}Yx/l_B^2}\,\hat{t}_{(X,Y)}$. At filling fraction $\nu = p/q$, the number of particles is $N = N_\Phi p/q$ and the many-body operator $\hat{T}_\alpha = \prod_{j=1}^{N} \hat{\mathcal{T}}^{(j)}_{L_\alpha \mathbf{e}_\alpha/N}$, where $\hat{\mathcal{T}}^{(j)}$ acts on the coordinate of the j-th particle, commutes with the many-body Hamiltonian (7.10). Translations along the two different axes of the torus, $\hat{T}_1$ and $\hat{T}_2$, do not commute $\hat{T}_1\hat{T}_2 = e^{2\pi i p/q}\hat{T}_2\hat{T}_1$, but $\hat{T}_1$ and $\hat{T}_2^q$ do commute, so that $\{\hat{H}, \hat{T}_1, \hat{T}_2^q\}$ is a maximal set of commuting operators. $\hat{T}_2$ leaves the energy unchanged, but translates between the q different degenerate states. This was first interpreted as a center-of-mass degeneracy [156] and later reconsidered as topological degeneracy [157].

7.5 Ground-state splitting due to weak disorder

In this section, we show that a weak random potential can lead to ground-state splittings which decrease exponentially with increasing number of particles [157]. For this reason fractional quantum Hall systems have been proposed as topologically-protected quantum memories [158].

A random single-particle potential $U(\mathbf{x})$ can lead to a coupling between the states of the lowest Landau level, so that the effective Hamiltonian has the form

$$\hat{H}'_{\mathrm{eff}} = \hat{H}_{\mathrm{eff}} + \sum_{i,j} t_{ij}\,\hat{a}_i^\dagger \hat{a}_j \tag{7.13}$$

where $t_{ij} = \int d\mathbf{x}\,\eta^*_{n=0,\,k_x=i}(\mathbf{x})U(\mathbf{x})\eta_{n=0,\,k_x=j}(\mathbf{x})$ and $\hat{H}_{\mathrm{eff}}$ is the effective Hamiltonian (7.11). The off-diagonal single-particle terms t_{ij} connect the two degenerate ground states by an N-th order tunneling process, similar to the case of correlated tunneling in double-well potentials and macroscopic superpositions of different quasi-momentum states in rotating ring lattices we discussed in Chapters 3 and 4, respectively. Parallel to our previous discussion, this coupling leads to a ground-state splitting in systems of finite size, while in the thermodynamic limit the splitting goes to zero and the ground-state degeneracy is recovered [157].

The exponential scaling of the ground-state splitting has recently attracted much attention, since the degenerate ground-state manifold might be used as a topologically-protected quantum memory [158]. A qubit $|\psi\rangle = \alpha\,|0\rangle + \beta\,|1\rangle$ can be stored in the coefficients of the wave function in the ground-state manifold $|\psi\rangle = \alpha\,|\psi_1\rangle + \beta\,|\psi_2\rangle$ where $|\psi_1\rangle$ and $|\psi_2\rangle$ are the degenerate many-body states. All other many-body states are separated from the ground-state manifold by the energy gap and transitions between the different states within the ground-state manifold due to external noise are exponentially suppressed.

7.6 Conclusion

In this chapter, we studied ultracold bosons on a two-dimensional square optical lattice in the presence of an effective magnetic field and pointed out a couple of features this system has in common with ultracold bosons in one-dimensional rotating ring lattices. We saw that in the presence of a magnetic field, the kinetic energy of a single particle is quantized into degenerate energy levels. Repulsive interactions lift the huge degeneracy of the non-interacting system and lead to strongly-correlated ground states such as the Laughlin state. On a manifold which is not simply-connected, e.g. on a torus, there remains a topological degeneracy of the many-body spectrum. In a finite system weak disorder potentials couple the degenerate states in N-th order perturbation theory and lead to superpositions of topologically distinct states. Similar to the case of correlated tunneling in double-well potentials and macroscopic superposition states in rotating ring lattices, these energy splittings decrease exponentially with increasing number of particles. For this reason the fractional quantum Hall systems have been proposed as a topologically-protected quantum memories.

Chapter 8

Summary and outlook

In this thesis we presented our research on strong correlations in ultracold atomic gases. In particular, we focused on ultracold bosons in rotating ring lattices and arrays of double-well potentials. In the first part, we studied the tunneling dynamics of bosons in double-well potentials. In the second part, we extended previous studies on bosons in rotating ring lattices to the case of ring superlattices and described a possible detection scheme to probe macroscopic superposition states of distinct flow. We then compared these macroscopic superposition states to those occurring in superconducting quantum interference devices. In the third part, we proposed to use dynamical modulations of double-well lattices to engineer robust entangled states on the hyperfine degrees of the atoms and described how to use them for measurement-based quantum computation. Finally, we studied ultracold bosons on a 2D lattice in the presence of an effective magnetic field and pointed out a couple of features this system has in common with 1D rotating ring lattices.

As outlined in the introduction, ultracold atomic gases have become a playground for many-body physics. Further research on the ground-state phase diagrams and the dynamics of quantum lattice models are an interesting topic for future investigations. One can consider bosonic and fermionic atomic gases with and without spin degrees of freedom; bosonic, fermionic or Bose-Fermi mixtures with or without disorder; systems with and without rotation in one-, two- or three-dimensional lattices with simple square or more complicated lattice geometries. Most important directions seem to be the study of quantum magnetism [162], quantum Hall physics, and interacting systems with disorder. A crucial road block both for quantum simulation and quantum information applications might be the lack of single-site measurements and addressability so far.

Finally, ultracold gases have also renewed the interest in some foundational questions of quantum many-body theory such as the dynamics of interacting quantum systems relaxing to equilibrium [163, 164, 165, 166, 167, 168].

Bibliography

[1] M. H. Anderson, J. R. Ensher, M. R. Matthews, C. E. Wieman, and E. A. Cornell. Observation of Bose-Einstein condensation in a dilute atomic vapor. *Science* **269**, 198 (1995).

[2] C. C. Bradley, C. A. Sackett, J. J. Tollett, and R. G. Hulet. Evidence of Bose-Einstein condensation in an atomic gas with attractive interactions. *Physical Review Letters* **75**, 1687 (1995). *ibid.* 79:1170, 1997.

[3] K. B. Davis, M.-O. Mewes, M. R. Andrews, N. J. van Druten, D. S. Durfee, D. M. Kurn, and W. Ketterle. Bose-Einstein condensation in a gas of sodium atoms. *Physical Review Letters* **75**, 3969 (1995).

[4] B. DeMarco and D. S. Jin. Onset of Fermi degeneracy in a trapped atomic gas. *Science* **285**, 1703 (1999).

[5] F. Schreck, L. Khaykovich, K. L. Corwin, G. Ferrari, T. Bourdel, J. Cubizolles, and C. Salomon. Quasipure Bose-Einstein condensate immersed in a Fermi sea. *Physical Review Letters* **87**, 080403 (2001).

[6] A. G. Truscott, K. E. Strecker, W. I. McAlexander, G. B. Partridge, and R. G. Hulet. Observation of Fermi pressure in a gas of trapped atoms. *Science* **291**, 2570 (2001).

[7] M. R. Andrews, C. G. Townsend, H.-J. Miesner, D. S. Durfee, D. M. Kurn, and W. Ketterle. Observation of interference between two Bose condensates. *Science* **275**, 637 (1997).

[8] I. Bloch, T. W. Hänsch, and T. Esslinger. Measurement of the spatial coherence of a trapped Bose gas at the phase transition. *Nature* **403**, 166 (2000).

[9] K. W. Madison, F. Chevy, W. Wohlleben, and J. Dalibard. Vortex formation in a stirred Bose-Einstein condensate. *Physical Review Letters* **84**, 806 (2000).

[10] J. R. Abo-Shaeer, C. Raman, J. M. Vogels, and W. Ketterle. Observation of vortex lattices in Bose-Einstein condensates. *Science* **292**, 476 (2001).

[11] Franco Dalfovo, Stefano Giorgini, Lev P. Pitaevskii, and Sandro Stringari. Theory of Bose-Einstein condensation in trapped gases. *Review of Modern Physics* **71**, 463 (1999).

[12] Anthony J. Leggett. Bose-Einstein condensation in the alkali gases: Some fundamental concepts. *Review of Modern Physics* **73**, 307 (2001).

[13] C. J. Pethick and H. Smith. *Bose-Einstein Condensation in Dilute Gases*. Cambridge University Press, (2002).

[14] L. Pitaevskii and S. Stringari. *Bose-Einstein condensation*. Oxford University Press, (2003).

[15] Ph. Courteille, R. S. Freeland, D. J. Heinzen, F. A. van Abeelen, and B. J. Verhaar. Observation of a Feshbach resonance in cold atom scattering. *Physical Review Letters* **81**, 69 (1998).

[16] S. Inouye, M. R. Andrews, J. Stenger, H.-J. Miesner, D. M. Stamper-Kurn, and W. Ketterle. Observation of Feshbach resonances in a Bose-Einstein condensate. *Nature* **392**, 151 (1998).

[17] M. Greiner, O. Mandel, T. Esslinger, T. W. Hänsch, and I. Bloch. Quantum phase

transition from a superfluid to a Mott insulator in a gas of ultracold atoms. *Nature* **415**, 39 (2002).

[18] D. Jaksch, C. Bruder, J. I. Cirac, C. W. Gardiner, and P. Zoller. Cold bosonic atoms in optical lattices. *Physical Review Letters* **81**, 3108 (1998).

[19] C. A. Regal, M. Greiner, and D. S. Jin. Observation of resonance condensation of fermionic atom pairs. *Physical Review Letters* **92**, 040403 (2004).

[20] M. Bartenstein, A. Altmeyer, S. Riedl, R. Geursen, S. Jochim, C. Chin, J. Hecker Denschlag, R. Grimm, A. Simoni, E. Tiesinga, C. J. Williams, and P. S. Julienne. Precise determination of ^{6}Li cold collision parameters by radio-frequency spectroscopy on weakly bound molecules. *Physical Review Letters* **94**, 103201 (2005).

[21] G. B. Partridge, K. E. Strecker, R. I. Kamar, M. W. Jack, and R. G. Hulet. Molecular probe of pairing in the BEC-BCS crossover. *Physical Review Letters* **95**, 020404 (2005).

[22] M. W. Zwierlein, J. R. Abo-Shaeer, A. Schirotzek, C. H. Schunck, and W. Ketterle. Vortices and superfluidity in a strongly interacting Fermi gas. *Nature* **435**, 1047 (2005).

[23] Immanuel Bloch, Jean Dalibard, and Wilhelm Zwerger. Many-body physics with ultracold gases. *Reviews of Modern Physics* **80**, 885 (2008).

[24] A. J. Leggett. Testing the limits of quantum mechanics: motivation, state of play, prospects. *Journal of Physics: Condensed Matter* **14**, R415 (2002).

[25] Richard P. Feynman. Simulating physics with computers. *International Journal of Theoretical Physics* **21**, 467 (1982).

[26] Michael A. Nielsen and Isaac L. Chuang. *Quantum Computation and Quantum Information*. Cambridge University Press, (2000).

[27] M. J. Holland and K. Burnett. Interferometric detection of optical phase shifts at the Heisenberg limit. *Physical Review Letters* **71**, 1355 (1993).

[28] Andreas Nunnenkamp, Ana Maria Rey, and Keith Burnett. Generation of macroscopic superposition states in ring superlattices. *Physical Review A* **77**, 023622 (2008).

[29] Andreas Nunnenkamp and Ana Maria Rey. Macroscopic superposition states in rotating ring lattices. arXiv:0802.4309, (2008).

[30] B. Vaucher, A. Nunnenkamp, and D. Jaksch. Creation of resilient entangled states and a resource for measurement-based quantum computation with optical superlattices. *New Journal of Physics* **10**, 023005 (2008).

[31] A. Nunnenkamp, J. N. Milstein, and K. Burnett. Classical field techniques for condensates in one-dimensional rings at finite temperatures. *Physical Review A* **75**, 033604 (2007).

[32] Matthew P. A. Fisher, Peter B. Weichman, G. Grinstein, and Daniel S. Fisher. Boson localization and the superfluid-insulator transition. *Physical Review B* **40**, 546 (1989).

[33] D. Jaksch and P. Zoller. The cold atom Hubbard toolbox. *Annals of Physics* **315**, 52 (2005).

[34] Nicola Marzari and David Vanderbilt. Maximally localised generalised Wannier functions for composite energy bands. *Physical Review B* **56**, 12847 (1997).

[35] Lixin He and David Vanderbilt. Exponential decay of Wannier functions and related quantities. *Physical Review Letters* **86**, 5341 (2001).

[36] H. P. Büchler, G. Blatter, and W. Zwerger. Commensurate-incommensurate transition of cold atoms in an optical lattice. *Physical Review Letters* **90**, 130401 (2003).

[37] Subir Sachdev. *Quantum Phase Transitions*. Cambridge University Press, (1999).

[38] Fabrice Gerbier, Artur Widera, Simon Fölling, Olaf Mandel, Tatjana Gericke, and Immanuel Bloch. Phase coherence of an atomic Mott insulator. *Physical Review Letters* **95**, 050404 (2005).

[39] Fabrice Gerbier, Simon Fölling, Arthur Widera, Olaf Mandel, and Immanuel Bloch. Probing the number statistics of ultracold atoms across the superfluid-Mott insulator transition. *Physical Review Letters* **96**, 090401 (2006).

[40] D. Van Oosten, P. van der Straten, and H. T. Stoof. Quantum phases in an optical lattices. *Physical Review A* **63**, 053601 (2001).

[41] Keith Burnett, Mark Edwards, Charles W Clark, and Martin Shotter. The Bogoliubov approach to number squeezing of atoms in an optical lattice. *Journal of Physics B* **35**, 1671 (2002).

[42] Ana Maria Rey, Keith Burnett, Robert Roth, Mark Edwards, Carl J Williams, and Charles W Clark. Bogoliubov approach to superfluidity of atoms in an optical lattice. *Journal of Physics B* **36**, 825–841 (2003).

[43] Thilo Stöferle, Henning Moritz, Christian Schori, Michael Köhl, and Tilman Esslinger. Transition from a strongly interacting 1D superfluid to a Mott insulator. *Physical Review Letters* **92**, 130403 (2004).

[44] Simon Fölling, Artur Widera, Torben Müller, Fabrice Gerbier, and Immanuel Bloch. Formation of spatial shell structure in the superfluid to Mott insulator transition. *Physical Review Letters* **97**, 060403 (2006).

[45] Gretchen K. Campbell, Jongchul Mun, Micah Boyd, Patrick Medley, Aaron E. Leanhardt, Luis G. Marcassa, David E. Pritchard, and Wolfgang Ketterle. Imaging the Mott insulator shells by using atomic clock shifts. *Science* **313**, 649 (2006).

[46] J. K. Freericks and H. Monien. Strong-coupling expansions for the pure and disordered Bose-Hubbard model. *Physical Review B* **53**, 2691 (1996).

[47] N. Elstner and H. Monien. Dynamics and thermodynamics of the Bose-Hubbard model. *Physical Review B* **59**, 12184 (1999).

[48] Ana Maria Rey, P. Blair Blakie, Guido Pupillo, Carl J. Williams, and Charles W. Clark. Bragg spectroscopy of ultracold atoms loaded in an optical lattice. *Physical Review A* **72**, 023407 (2005).

[49] D.M. Stamper-Kurn and W. Ketterle. *Course 2: Spinor Condensates and Light Scattering from Bose-Einstein Condensates*, volume 72/2001 of *Les Houches*. Springer Berlin / Heidelberg, (2001).

[50] R. Roth and K. Burnett. Superfluidity and interference pattern of ultracold bosons in optical lattices. *Physical Review A* **67**, 031602 (2003).

[51] E. Toth, A. M. Rey, and P. B. Blakie. Theory of correlations between ultra-cold bosons released from an optical lattice. arXiv:0803.2922, (2008).

[52] Ehud Altman, Eugene Demler, and Mikhail D. Lukin. Probing many-body states of ultracold atoms via noise correlations. *Physical Review A* **70**, 013603 (2004).

[53] M. Greiner, C. A. Regal, J. T. Stewart, and D. S. Jin. Probing pair-correlated fermionic atoms through correlations in atom shot noise. *Physical Review Letters* **94**, 110401 (2005).

[54] S. Fölling, F. Gerbier, A. Widera, O. Mandel, T. Gericke, and I. Bloch. Spatial quantum noise interferometry in expanding ultracold atom clouds. *Nature* **434**, 481 (2005).

[55] T. Rom, Th. Best, D. van Oosten, U. Schneider, S. Fölling, B. Paredes, and I. Bloch. Free fermion antibunching in a degenerate atomic Fermi gas released from an optical lattice. *Nature* **444**, 733 (2006).

[56] Artur Widera, Fabrice Gerbier, Simon Fölling, Tatjana Gericke, Olaf Mandel, and Immanuel Bloch. Coherent collisional spin dynamics in optical lattices. *Physical Review Letters* **95**, 190405 (2005).

[57] Markus Greiner, Olaf Mandel, Theodor W. Hänsch, and Immanuel Bloch. Collapse and revival of the matter wave field of a Bose-Einstein condensate. *Nature* **419**, 51 (2002).

[58] D. Jaksch, H.-J. Briegel, J. I. Cirac, C. W. Gardiner, and P. Zoller. Entanglement of atoms via cold controlled collisions. *Physical Review Letters* **82**, 1975 (1999).

[59] Olaf Mandel, Markus Greiner, Artur Widera, Tim Rom, Theodor W. Hänsch, and Immanuel Bloch. Coherent transport of neutral atoms in spin-dependent optical lattice potentials. *Physical Review Letters* **91**, 010407 (2003).

[60] Olaf Mandel, Markus Greiner, Artur Widera, Tim Rom, Theodor W. Hansch, and Immanuel Bloch. Controlled collisions for multi-particle entanglement of optically trapped atoms. *Nature* **425**, 937 (2003).

[61] Hans J. Briegel and Robert Raussendorf. Persistent entanglement in arrays of interacting particles. *Physical Review Letters* **86**, 910 (2001).

[62] R. Raussendorf and H.-J. Briegel. A one-way quantum computer. *Physical Review Letters* **86**, 5188 (2001).

[63] J. Sebby-Strabley, M. Anderlini, P. S. Jessen, and J. V. Porto. Lattice of double wells for manipulating pairs of cold atoms. *Physical Review A* **73**, 033605 (2006).

[64] Marco Anderlini, Jennifer Sebby-Strabley, Jens Kruse, James V Porto, and William D Phillips. Controlled atom dynamics in a double-well optical lattice. *Journal of Physics B* **39**, S199 (2006).

[65] S. Fölling, S. Trotzky, P. Cheinet, M. Feld, R. Saers, A. Widera, T. Müller, and I. Bloch. Direct observation of second-order atom tunnelling. *Nature* **448**, 1029 (2007).

[66] Marco Anderlini, Patricia J. Lee, Benjamin L. Brown, Jennifer Sebby-Strabley, William D. Phillips, and J. V. Porto. Controlled exchange interaction between pairs of neutral atoms in an optical lattice. *Nature* **448**, 452 (2007).

[67] S. Trotzky, P. Cheinet, S. Fölling, M. Feld, U. Schnorrberger, A. M. Rey, A. Polkovnikov, E. A. Demler, M. D. Lukin, and I. Bloch. Time-resolved observation and control of superexchange interactions with ultracold atoms in optical lattices. *Science* **319**, 295 (2008).

[68] D. R. Dounas-Frazer and L. D. Carr. Tunneling resonances and entanglement dynamics of cold bosons in the double well. quant-ph/0610166, (2006).

[69] D. R. Dounas-Frazer, A. M. Hermundstad, and L. D. Carr. Ultracold bosons in a tilted multilevel double-well potential. *Physical Review Letters* **99**, 200402 (2007).

[70] Sascha Zöllner, Hans-Dieter Meyer, and Peter Schmelcher. Few-boson dynamics in double wells: From single-atom to correlated pair tunneling. *Physical Review Letters* **100**, 040401 (2008).

[71] K. Winkler, G. Thalhammer, F. Lang, R. Grimm, J. Hecker Denschlag, A. J. Daley, A. Kantian, H. P. Büchler, and P. Zoller. Repulsively bound atom pairs in an optical lattice. *Nature* **441**, 853 (2006).

[72] P. Cheinet, S. Trotzky, M. Feld, U. Schnorrberger, M. Moreno-Cardoner, S. Fölling, and I. Bloch. Counting atoms using interaction blockade in an optical superlattice. *Physical Review Letters* **101**, 090404 (2008).

[73] E. Schrödinger. Die gegenwärtige Situation in der Quantenmechanik. *Die Naturwissenschaften* **48**, 807 (1935).

[74] J. J . Bollinger, Wayne M. Itano, D. J. Wineland, and D. J. Heinzen. Optimal frequency measurements with maximally correlated states. *Physical Review A* **54**, R4649 (1996).

[75] D. Leibfried, E. Knill, S. Seidelin, J. Britton, R. B. Blakestad, J. Chiaverini, D. B. Hume, W. M. Itano, J. D. Jost, C. Langer, R. Ozeri, R. Reichle, and D. J. Wineland. Creation of a six-atom Schrödinger cat state. *Nature* **438**, 639 (2005).

[76] J. I. Cirac, M. Lewenstein, K. Mølmer, and P. Zoller. Quantum superposition states of Bose-Einstein condensates. *Physical Review A* **57**, 1208 (1998).

[77] A. Sørensen, L.-M. Duan, J. I. Cirac, and P. Zoller. Many-particle entanglement with Bose-Einstein condensates. *Nature* **409**, 63 (2001).

[78] Jacob Dunningham and David Hallwood. Creation of macroscopic superpositions of flow states with Bose-Einstein condensates. *Physical Review A* **74**, 023601 (2006).

[79] J. A. Dunningham, K. Burnett, R. Roth, and W. D. Phillips. Creation of macroscopic superposition states from arrays of Bose-Einstein condensates. *New Journal of Physics* **8**, 182 (2006).

[80] David Hallwood, Keith Burnett, and Jacob Dunningham. Macroscopic superpositions of superfluid flows. *New Journal of Physics* **8**, 180 (2006).

[81] David Hallwood, Keith Burnett, and Jacob Dunningham. The barriers to producing multiple-particle superposition states in rotating Bose-Einstein condensates. *Journal of Modern Optics* **54**, 2129 (2007).

[82] Ana Maria Rey, Keith Burnett, Indubala I. Satija, and Charles W. Clark. Entanglement and the Mott transition in a rotating bosonic ring lattice. *Physical Review A* **75**, 063616 (2007).

[83] G. Watanabe and C. J. Pethick. Reversal of the circulation of a vortex by quantum tunneling in trapped Bose systems. *Physical Review A* **76**, 021605(R) (2007).

[84] Luigi Amico, Andreas Osterloh, and Francesco Cataliotti. Quantum many particle systems in ring-shaped optical lattices. *Physical Review Letters* **95**, 063201 (2005).

[85] S. Franke-Arnold, J. Leach, M. J. Padgett, V. E. Lembessis, D. Ellinas, A. J. Wright, J. M. Girkin, P. Ohberg, and A. S. Arnold. Optical ferris wheel for ultracold atoms. *Optics Express* **15**, 8619 (2007).

[86] S. Chavez-Cerda, M. J. Padgett, I. Allison, G. H. C. New, J. C. Gutierrez-Vega, A. T. O'Neil, I. MacVicar, and J. Courtial. Holographic generation and orbital angular momentum of high-order Mathieu beams. *Journal of Optics B* **4**, S52 (2002).

[87] V. Boyer, R. M. Godun, G. Smirne, D. Cassettari, C. M. Chandrashekar, A. B. Deb,

Z. J. Laczik, and C. J. Foot. Dynamic manipulation of Bose-Einstein condensates with a spatial light modulator. *Physical Review A* **73**, 031402 (2006).

[88] Rajiv Bhat, M. J. Holland, and L. D. Carr. Bose-Einstein condensates in rotating lattices. *Physical Review Letters* **96**, 060405 (2006).

[89] R. Peierls. Zur Theorie des Diamagnetismus von Leitungselektronen. *Zeitschrift fur Physik* **80**, 763 (1933).

[90] M. Cozzini, B. Jackson, and S. Stringari. Vortex signatures in annular Bose-Einstein condensates. *Physical Review A* **73**, 013603 (2006).

[91] Brandon M Peden, Rajiv Bhat, Meret Krämer, and Murray J Holland. Quasi-angular momentum of Bose and Fermi gases in rotating optical lattices. *Journal of Physics B* **40**, 3725 (2007).

[92] Caspar H. van der Wal, A. C. J. ter Haar, F. K. Wilhelm, R. N. Schouten, C. J. P. M. Harmans, T. P. Orlando, Seth Lloyd, and J. E. Mooij. Quantum superposition of macroscopic persistent-current states. *Science* **290**, 773 (2000).

[93] I. Chiorescu, Y. Nakamura, C. J. P. M. Harmans, and J. E. Mooij. Coherent quantum dynamics of a superconducting flux qubit. *Science* **299**, 1869 (2003).

[94] Ulrich Eckern, Gerd Schön, and Vinay Ambegaokar. Quantum dynamics of a superconducting tunnel junction. *Physical Review B* **30**, 6419 (1984).

[95] Shin Takagi. *Macroscopic Quantum Tunneling*. Cambridge University Press, (2002).

[96] J. E. Mooij, T. P. Orlando, L. Levitov, Lin Tian, Caspar H. van der Wal, and Seth Lloyd. Josephson persistent-current qubit. *Science* **285**, 1036 (1999).

[97] A. J. Leggett. *Chance and Matter*, chapter Quantum mechanics at the macroscopic level, 395–506. North Holland (1987).

[98] M. Arndt, O. Nairz, J. Voss-Andreae, C. Keller, G. van der Zouw, and A. Zeilinger. Wave-particle duality of C_{60} molecules. *Nature* **401**, 680 (1999).

[99] Fabrice Gerbier, Artur Widera, Simon Fölling, Olaf Mandel, and Immanuel Bloch. Resonant control of spin dynamics in ultracold quantum gases by microwave dressing. *Physical Review A* **73**, 041602 (2006).

[100] Artur Widera, Fabrice Gerbier, Simon Fölling, Tatjana Gericke, Olaf Mandel, and Immanuel Bloch. Precision measurement of spin-dependent interaction strengths for spin-1 and spin-2 Rb atoms. *New Journal of Physics* **8**, 152 (2006).

[101] H. Pu and P. Meystre. Creating macroscopic atomic Einstein-Podolsky-Rosen states from Bose-Einstein condensates. *Physical Review Letters* **85**, 3987 (2000).

[102] L.-M. Duan, A. Sørensen, J. I. Cirac, and P. Zoller. Squeezing and entanglement of atomic beams. *Physical Review Letters* **85**, 3991 (2000).

[103] A. M. Rey, V. Gritsev, I. Bloch, E. Demler, and M. D. Lukin. Preparation and detection of magnetic quantum phases in optical superlattices. *Physical Review Letters* **99**, 140601 (2007).

[104] S. Peil, J. V. Porto, B. Laburthe Tolra, J. M. Obrecht, B. E. King, M. Subbotin, S. L. Rolston, and W. D. Phillips. Patterned loading of a Bose-Einstein condensate into an optical lattice. *Physical Review A* **67**, 051603 (2003).

[105] P. J. Lee, M. Anderlini, B. L. Brown, J. Sebby-Strabley, W. D. Phillips, and J. V. Porto. Sublattice addressing and spin-dependent motion of atoms in a double-well lattice. *Physical Review Letters* **99**, 020402 (2007).

[106] Tin-Lun Ho. Spinor Bose condensates in optical traps. *Physical Review Letters* **81**, 742 (1998).

[107] G. J. Milburn, J. Corney, E. M. Wright, and D. F. Walls. Quantum dynamics of an atomic Bose-Einstein condensate in a double-well potential. *Physical Review A* **55**, 4318 (1997).

[108] C. Menotti, J. R. Anglin, J. I. Cirac, and P. Zoller. Dynamic splitting of a Bose-Einstein condensate. *Physical Review A* **63**, 023601 (2001).

[109] D. Jaksch, S. A. Gardiner, K. Schulze, J. I. Cirac, and P. Zoller. Uniting Bose-Einstein condensates in optical resonators. *Physical Review Letters* **86**, 4733 (2001).

[110] Oriol Romero-Isart and Juan José García-Ripoll. Quantum ratchets for quantum communication with optical superlattices. *Physical Review A* **76**, 052304 (2007).

[111] Tassilo Keilmann and Juan José García-Ripoll. Dynamical creation of bosonic Cooper-like pairs. *Physical Review Letters* **100**, 110406 (2008).

[112] Peter Barmettler, Ana Maria Rey, Eugene Demler, Mikhail D. Lukin, Immanuel Bloch, and Vladimir Gritsev. Quantum many-body dynamics of coupled double-well superlattices. arXiv:0803.1643, (2008).

[113] Alastair Kay and Jiannis K. Pachos. Quantum computation in optical lattices via global laser addressing. *New Journal of Physics* **6**, 126 (2004).

[114] R. Raussendorf and H. Briegel. Computational model underlying the one-way quantum computer. *Quantum Information & Computation* **6**, 433 (2002).

[115] M. S. Tame, M. Paternostro, and M. S. Kim. One-way quantum computing in a decoherence-free subspace. *New Journal of Physics* **9**, 201 (2007).

[116] Ana Maria Rey. *Ultra-cold bosonic atoms in optical lattices*. PhD thesis, University of Maryland at College Park, (2004).

[117] Masahito Ueda and Masato Koashi. Theory of spin-2 Bose-Einstein condensates: Spin correlations, magnetic response, and excitation spectra. *Physical Review A* **65**, 063602 (2002).

[118] Wenxian Zhang, Su Yi, and L. You. Bose-Einstein condensation of trapped interacting spin-1 atoms. *Physical Review A* **70**, 043611 (2004).

[119] B. Vaucher, S. R. Clark, U. Dorner, and D. Jaksch. Fast initialization of a high-fidelity quantum register using optical superlattices. *New Journal of Physics* **9**, 221 (2007).

[120] N. Teichmann and C. Weiss. Coherently controlled entanglement generation in a binary Bose-Einstein condensate. *Europhysics Letters* **78**, 10009 (2007).

[121] David Hayes, Paul S. Julienne, and Ivan H. Deutsch. Quantum logic via the exchange blockade in ultracold collisions. *Physical Review Letters* **98**, 070501 (2007).

[122] L.-M. Duan, E. Demler, and M. D. Lukin. Controlling spin exchange interactions of ultracold atoms in optical lattices. *Physical Review Letters* **91**, 090402 (2003).

[123] Jiannis K. Pachos and Peter L. Knight. Quantum computation with a one-dimensional optical lattice. *Physical Review Letters* **91**, 107902 (2003).

[124] Jens Eisert and Hans J. Briegel. Schmidt measure as a tool for quantifying multi-particle entanglement. *Physical Review A* **64**, 022306 (2001).

[125] Chuanwei Zhang, S. L. Rolston, and S. Das Sarma. Manipulation of single neutral atoms in optical lattices. *Physical Review A* **74**, 042316 (2006).

[126] S. F. Huelga, C. Macchiavello, T. Pellizzari, A. K. Ekert, M. B. Plenio, and J. I. Cirac. Improvement of frequency standards with quantum entanglement. *Physical Review Letters* **79**, 3865 (1997).

[127] Dan Browne and Hans Briegel. *One-way quantum computation*. Wiley, (2006).

[128] O. Mandel, M. Greiner, A. Widera, T. Rom, T. W. Hänsch, and I. Bloch. Controlled collisions for multi-particle entanglement of optically trapped atoms. *Nature* **425**, 937 (2003).

[129] P. Walther, K. J. Resch, T. Rudolph, E. Schenck, H. Weinfurter, V. Vedral, M. Aspelmeyer, and A. Zeilinger. Experimental one-way quantum computing. *Nature* **434**, 169 (2005).

[130] R. Prevedel, P. Walther, F. Tiefenbacher, P. Böhi, R. Kaltenbaek, T. Jennewein, and A. Zeilinger. High-speed linear optics quantum computing using active feed-forward. *Nature* **445**, 65 (2007).

[131] D. Gross and J. Eisert. Novel schemes for measurement-based quantum computation. *Physical Review Letters* **98**, 220503 (2007).

[132] D. Gross, J. Eisert, N. Schuch, and D. Perez-Garcia. Measurement-based quantum computation beyond the one-way model. *Physical Review A* **76**, 052315 (2007).

[133] H. Pu, C. K. Law, S. Raghavan, J. H. Eberly, and N. P. Bigelow. Spin-mixing dynamics of a spinor Bose-Einstein condensate. *Physical Review A* **60**, 1463 (1999).

[134] K. v. Klitzing, G. Dorda, and M. Pepper. New method for high-accuracy determination of the fine-structure constant based on quantized Hall resistance. *Physical Review Letters* **45**, 494 (1980).

[135] D. C. Tsui, H. L. Störmer, and A. C. Gossard. Two-dimensional magnetotransport in the extreme quantum limit. *Physical Review Letters* **48**, 1559 (1982).

[136] Jainendra K. Jain. *Composite Fermions*. Cambridge University Press, (2007).

[137] R. B. Laughlin. Anomalous quantum Hall effect: An incompressible quantum fluid with fractionally charged excitations. *Physical Review Letters* **50**, 1395 (1983).

[138] S. A. Trugman and S. Kivelson. Exact results for the fractional quantum Hall effect with general interactions. *Physical Review B* **31**, 5280 (1985).

[139] N. K. Wilkin, J. M. F. Gunn, and R. A. Smith. Do attractive bosons condense? *Physical Review Letters* **80**, 2265 (1998).

[140] N. K. Wilkin and J. M. F. Gunn. Condensation of composite bosons in a rotating BEC. *Physical Review Letters* **84**, 6 (2000).

[141] N. R. Cooper, N. K. Wilkin, and J. M. F. Gunn. Quantum phases of vortices in rotating Bose-Einstein condensates. *Physical Review Letters* **87**, 120405 (2001).

[142] V. Schweikhard, I. Coddington, P. Engels, V. P. Mogendorff, and E. A. Cornell. Rapidly rotating Bose-Einstein condensates in and near the lowest Landau level. *Physical Review Letters* **92**, 040404 (2004).

[143] D Jaksch and P Zoller. Creation of effective magnetic fields in optical lattices: the Hofstadter butterfly for cold neutral atoms. *New Journal of Physics* **5**, 56 (2003).

[144] Anders S. Sørensen, Eugene Demler, and Mikhail D. Lukin. Fractional quantum Hall states of atoms in optical lattices. *Physical Review Letters* **94**, 086803 (2005).

[145] Rajiv Bhat, B. M. Peden, B. T. Seaman, M. Krämer, L. D. Carr, and M. J. Holland. Quantized vortex states of strongly interacting bosons in a rotating optical lattice. *Physical Review A* **74**, 063606 (2006).

[146] Rajiv Bhat, M. Krämer, J. Cooper, and M. J. Holland. Hall effects in Bose-Einstein condensates in a rotating optical lattice. *Physical Review A* **76**, 043601 (2007).

[147] M. Hafezi, A. S. Sørensen, E. Demler, and M. D. Lukin. Fractional quantum Hall effect in optical lattices. *Physical Review A* **76**, 023613 (2007).

[148] M. Hafezi, A. S. Sørensen, M. D. Lukin, and E. Demler. Characterization of topological states on a lattice with Chern number. *Europhysics Letters* **81**, 10005 (2008).

[149] Douglas R. Hofstadter. Energy levels and wave functions of Bloch electrons in rational and irrational magnetic fields. *Physical Review B* **14**, 2239 (1976).

[150] Dung-Hai Lee and Jon Magne Leinaas. Mott insulators without symmetry breaking. *Physical Review Letters* **92**, 096401 (2004).

[151] Alexander Seidel, Henry Fu, Dung-Hai Lee, Jon Magne Leinaas, and Joel Moore. Incompressible quantum liquids and new conservation laws. *Physical Review Letters* **95**, 266405 (2005).

[152] R. Tao and D. J. Thouless. Fractional quantization of Hall conductance. *Physical Review B* **28**, 1142 (1983).

[153] E. J. Bergholtz and A. Karlhede. Quantum Hall system in Tao-Thouless limit. *Physical Review B* **77**, 155308 (2008).

[154] E. H. Rezayi and F. D. M. Haldane. Laughlin state on stretched and squeezed cylinders and edge excitations in the quantum Hall effect. *Physical Review B* **50**, 17199 (1994).

[155] B. Andrei Bernevig and F. D. M. Haldane. Fractional quantum Hall states and Jack polynomials. arXiv:0707.3637, (2008).

[156] F. D. M. Haldane. Many-particle translational symmetries of two-dimensional electrons at rational Landau-level filling. *Physical Review Letters* **55**, 2095 (1985).

[157] X. G. Wen and Q. Niu. Ground-state degeneracy of the fractional quantum Hall states in the presence of a random potential and on high-genus Riemann surfaces. *Physical Review B* **41**, 9377 (1990).

[158] A. Yu. Kitaev. Fault-tolerant quantum computation by anyons. *Annals of Physics* **303**, 2 (2003).

[159] P. G. Harper. Single band motion of conduction electrons in a uniform magnetic field. *Proccedings of the Physical Society A* **68**, 874 (1955).

[160] Ana Maria Rey, Indubala I. Satija, and Charles W. Clark. Quantum coherence of hard-core bosons: Extended, glassy, and Mott phases. *Physical Review A* **73**, 063610 (2006).

[161] D. J. Thouless. Long-range order and the fractional quantum Hall effect. *Physical Review B* **31**, 8305 (1985).

[162] Assa Auerbach. *Interacting Electrons and Quantum Magnetism*. Springer, (1998).

[163] T. Kinoshita, T. Wenger, and D. S. Weiss. A quantum Newton's cradle. *Nature* **440**, 900903 (2006).

[164] Marcos Rigol, Vanja Dunjko, Vladimir Yurovsky, and Maxim Olshanii. Relaxation in a completely integrable many-body quantum system: An ab initio study of the dynamics of the highly excited states of 1D lattice hard-core bosons. *Physical Review Letters* **98**, 050405 (2007).

[165] S. Hofferberth, I. Lesanovsky, B. Fischer, T. Schumm, and J. Schmiedmayer. Non-

equilibrium coherence dynamics in one-dimensional Bose gases. *Nature* **449**, 324327 (2007).

[166] Marcos Rigol, Vanja Dunjko, and Maxim Olshanii. Thermalization and its mechanism for generic isolated quantum systems. *Nature* **452**, 854 (2008).

[167] M. Cramer, C. M. Dawson, J. Eisert, and T. J. Osborne. Exact relaxation in a class of nonequilibrium quantum lattice systems. *Physical Review Letters* **100**, 030602 (2008).

[168] T. Barthel and U. Schollwöck. Dephasing and the steady state in quantum many-particle systems. *Physical Review Letters* **100**, 100601 (2008).